UNIVERSIDADE DE LISBOA

INSTITUTO SUPERIOR TÉCNICO

Ultrasound Based Navigation and Control for Orthopaedic Robot Surgery

Pedro Miguel Baptista Torres

Supervisor: Doctor Jorge Manuel Mateus Martins
Co-Supervisor: Doctor Paulo Jorge Sequeira Gonçalves

Thesis approved in public session to obtain the PhD Degree in Mechanical Engineering

Jury final classification: Pass with Merit

Jury

Chairperson: Chairman of the IST Scientific Board

Members of the Committee:

Doctor Carlos Peréz Vidal
Doctor José Manuel Gutierrez Sá da Costa
Doctor João Rogério Caldas Pinto
Doctor Paulo Jorge Sequeira Gonçalves
Doctor João Miguel Raposo Sanches
Doctor Jorge Manuel Mateus Martins

2015

UNIVERSIDADE DE LISBOA

INSTITUTO SUPERIOR TÉCNICO

Ultrasound Based Navigation and Control for Orthopaedic Robot Surgery

Pedro Miguel Baptista Torres

Supervisor: Doctor Jorge Manuel Mateus Martins

Co-Supervisor: Doctor Paulo Jorge Sequeira Gonçalves

Thesis approved in public session to obtain the PhD Degree in Mechanical Engineering

Jury final classification: Pass with Merit

Jury

Chairperson: Chairman of the IST Scientific Board

Members of the Committee:

Doctor Carlos Peréz Vidal, Professor Titular da Universidad Miguel Hernández de Elche, Espanha;

Doctor José Manuel Gutierrez Sá da Costa, Professor Catedrático do Instituto Superior Técnico, da Universidade de Lisboa;

Doctor João Rogério Caldas Pinto, Professor Associado (com Agregação) do Instituto Superior Técnico, da Universidade de Lisboa;

Doctor Paulo Jorge Sequeira Gonçalves, Professor Coordenador da Escola Superior de Tecnologia do Instituto Politécnico de Castelo Branco;

Doctor João Miguel Raposo Sanches, Professor Auxiliar (com Agregação) do Instituto Superior Técnico, da Universidade de Lisboa;

Doctor Jorge Manuel Mateus Martins, Professor Auxiliar do Instituto Superior Técnico, da Universidade de Lisboa.

2015

Abstract

Surgical Robotics is an expanding area, contributing to the increased precision and accuracy of surgical procedures, besides producing more reliable and reproducible results, minimizing the invasiveness, reducing complications and improving patient safety, compared with conventional techniques. Navigation within the operating room is fundamental to the success of robotic systems. In this context a new navigation system, used in the control loop, to co-manipulate a robotic system developed to assist orthopaedic surgeons, is proposed. Although it may have other applications, the system is designed to perform a hole in the femur head, necessary to implant the initial guide wire used in Hip Resurfacing surgery. During the surgery, the bone position and orientation is obtained through a registration process between a set of US images acquired in real time and the CT femur model, preloaded pre-operatively. Contrary to current surgical systems, it does not use any type of implant in the bone, to localize the femur, but passive markers, of an optical measurement system, placed on the probe and the robot to measure their 3D poses. Experimental validation tests were performed on a human's femur phantom, validating the proposed system.

Keywords: Hip Arthroplasty , Surgical Robotics , Image-guided surgery , Ultrasound imaging , Medical image processing , Image Segmentation , 3D Surface Reconstruction , Surface-based Registration , Visual Servoing , Image-based tracking

Resumo

A Robótica cirúrgica é uma área em expansão, contribuindo para o aumento da precisão e exatidão dos procedimentos cirúrgicos, além de produzir resultados mais confiáveis e reprodutíveis, minimizando a invasividade, reduzindo as complicações e melhorando a segurança dos pacientes, comparativamente com as técnicas convencionais. A navegação dentro da sala de operações é primordial para o sucesso dos sistemas robóticos. Neste contexto é proposto um novo sistema de navegação, usado na malha de controlo, de um sistema robótico co-manipulado, dedesenvolvido para auxiliar os cirurgiões ortopédicos. Embora possa ter outras aplicações, o sistema foi desenvolvido para realizar um furo na cabeça do fémur, necessário ao implante do fio guia na cirurgia de substituição parcial da anca. Durante a cirurgia, a posição e orientação do osso é obtida através de um processo de registo entre as imagens de US adquiridas em tempo real e o modelo CT do fémur, previamente carregado no pré-operatório. Contrariamente aos sistemas cirúrgicos atuais, não usa nenhum tipo de implante no osso para localizar o fémur, mas sim marcadores passivos colocados na sonda e no robô, e um sistema de medição óptico para medir as suas posições 3D. Os testes experimentais de validação foram realizados num *phantom* de um fémur humano.

Palavras-chave: Artroplastia da anca, Robôs de cirurgia, Cirurgia guiada por imagem, Ultrasonografia, Processamento de imagens médicas, Segmentação de imagem, Reconstrução de Superficie 3D, Registo baseado em superficie, Controlo visual, Seguimento baseado em imagem

Acknowledgements

I would like to thank my advisor, Professor Jorge Manuel Mateus Martins and co-advisor Professor Paulo Jorge Sequeira Gonçalves, for the opportunity they gave me to do this work. Particularly special thanks to Professor Paulo Gonçalves, by having followed closely my work.

I would also like to thank Professor João Miguel Sanches, for its availability and suggestions for the development of this work on image processing component.

Thanks to the Portuguese Science and Technology Foundation (FCT) for the PROTEC funding program and also thanks to the advanced training program of the Polytechnic Institute of Castelo Branco.

Finally I would like to extend my thanks all those which in one way or another (providing ideas and / or constructive criticism) were helping anonymously in numerous discussions throughout this work.

This work was partly supported by the Strategic Project, $PEst-OE/EME/LA0022/$, through FCT (under IDMEC-IST, Research Group: IDMEC/LAETA/CSI), FCT project $PTDC/EME-CRO/099333/2008$ and $EU-FP7-ICT-231143$, project ECHORD.

Contents

Abstract i

Resumo iii

Acknowledgements v

1 Introduction 1

1.1 Background and Motivation . . . 1
1.2 State of the Art . . . 3
1.3 HipRob project . . . 7
1.4 Objectives . . . 8
1.5 Contributions . . . 9
1.6 Publications . . . 10
  1.6.1 Book Chapters . . . 10
  1.6.2 Papers in Refereed International Journals . . . 10
  1.6.3 Papers in Proceedings of International Conferences . . . 11
  1.6.4 Papers in Proceedings of National Conferences . . . 11
1.7 Outline of the Thesis . . . 12

2 Image Acquisition 15

2.1 Ultrasound Image Acquisition . . . 15
  2.1.1 Freehand Ultrasound Acquisition System . . . 15
  2.1.2 Non Freehand Ultrasound Acquisition System . . . 19

2.2 CT Image Acquisition 21

3 **Image Processing** **23**

3.1 Ultrasound Image Processing and Segmentation 23

3.1.1 Segmentation Method 24

3.1.2 Image Processing and Segmentation Results 26

3.1.3 Point Cloud Extraction 33

3.2 Processing and Segmentation of CT Images 34

3.2.1 Point Cloud Extraction 36

3.3 3D Reconstruction and Visualization 37

3.3.1 3D Reconstruction and Visualization Experimental Results 39

4 **Image Registration** **43**

4.1 Introduction 43

4.2 Iterative Closest Point (ICP) Method 44

4.3 Coherent Point Drift (CPD) Method 46

4.4 Experimental Results 46

5 **Visual Control of Robotic Manipulator using Fuzzy Models** **51**

5.1 Introduction 52

5.2 Fuzzy Modeling 54

5.2.1 Off-Line Fuzzy Modeling 54

5.2.2 Takagi–Sugeno fuzzy model 55

5.2.3 Fuzzy Model Parameters Identification by fuzzy clustering 56

5.2.4 On-Line Fuzzy Modeling 57

5.2.5 Uncalibrated Fuzzy Visual Servoing 59

5.3 Experimental Setup 59

5.3.1 Fuzzy Modeling Results 60

5.3.2 Control Results 65

6 Ultrasound Based Robot Navigation **69**

6.1 Bone Tracking based on 2D Ultrasound (US) Images 69

6.2 Navigation System Calibration 72

6.3 Robot Navigation 74

6.4 Experimental Setup 79

6.5 Experimental Results 80

7 Conclusions **89**

7.1 General Conclusions 89

7.2 Suggestions for Future Work 92

Bibliography **93**

List of Tables

3.1 Quantification of segmentation errors 33

4.1 Registration Errors Results, with a cow femur bone. 46

4.2 Registration Errors Results of the human femur. 48

5.1 Results of the off-line fuzzy model, obtained for each joint. 64

5.2 Results of the on-line fuzzy model, obtained for each joint. 64

6.1 Quantification of segmentation errors during the on-line femur tracking. 82

6.2 Calibration error results, after registration. 83

6.3 Results before and after the on-line Registration Process. 84

6.4 Errors between the drilling point variation and the corresponding variations of the robot, in the tracker reference frame. 86

6.5 Movements of the drilling point. 86

List of Figures

1.1 Prosthesis used in Hip Resurfacing and Total Hip Replacement. 2

1.2 $smith\&nephew$, BIRMINGHAM HIP Resurfacing System (Extracted from Smith$\&$Nephew (2008)). 3

1.3 Overview of the hardware setup and frames transformations of HipRob navigation system. 8

2.1 Optical Tracking System and coordinate frames used in image acquisition process. 17

2.2 Tools Specifications, extracted from the Polaris Spectra Tool Kit Guide. 18

2.3 Robotic 3D US system. 20

3.1 Segmentation Algorithm Flowchart. 27

3.2 Ultrasound image before and after denoising process. 28

3.3 Evolution of Processing time during Denoising. 29

3.4 Result of segmentation in US image and contour overlay on the original image. . . 29

3.5 Segmentation time evolution and number of iterations need in each image. 30

3.6 Surface detection in US images through a needle. 31

3.7 Points of a contour extracted from a manual segmentation (green) and through the proposed method (blue). 32

3.8 Point cloud extracted from ultrasound images, referenced to the polaris referential frame. 34

3.9 Segmentation steps of CT images, on the head of the femur. 35

3.10 Segmentation steps of CT images, on the head of the femur, with the proposed method. 36

3.11 Segmentation result of CT images in the central part of the bone. 37

3.12 Point clouds of CT images. 38

3.13 Femur Bone Reconstruction, with a high level of transparency (Maximum Intensity Projection (MIP)). 39

3.14 Femur Bone Reconstruction, with highlight bone definitions. 40

3.15 Cross section Femur Bone Reconstruction. 40

3.16 Volume Rendering performed in Matlab. 41

3.17 Surface Rendering performed in Matlab. 41

3.18 Results of Visualization a human femur. 42

4.1 Example of alignment for local minimum. 45

4.2 Registration Results of cow femur bone. 47

4.3 Registration Results of human femur. 48

5.1 The eye-to-hand experimental setup. 61

5.2 Configuration of the markers placed on the end-effector. 61

5.3 3D Spiral path used to collect the data for the fuzzy model identification, solid thin line. Task linear trajectory used to test the visual servo control law, dash-dotted thick line. 62

5.4 The input data for model identification, $\delta\mathbf{s}_{xy}(k+1)$, i.e., in the x and y directions. . 63

5.5 The input data for model identification, $\delta\mathbf{s}_{z}(k+1)$, i.e., in the z direction. 64

5.6 The output data, $\delta\mathbf{q}(k)$. For model identification, solid-line, and the estimated fuzzy model output, dash-dotted line. 65

5.7 The output data, $\delta q_4(k)$. For model identification, solid-line, and the estimated fuzzy model output, dash-dotted line. 65

5.8 Uncalibrated Visual Servo Control Loop. 66

5.9 Evolution of the error of the position on the X coordinate. 67

5.10 Evolution of the error of the position on the Y coordinate. 68

5.11 Evolution of the error of the position on the Z coordinate. 68

6.1 Flowchart of the bone tracking based in US images. 70

6.2 Region of interest in an US image of a femur phantom. 71

6.3 Detail the acquisition of points in the femur head (calibration method 1). 73

6.4 Scan of the femur with the ultrasound probe to extract features (calibration method 2). . . . 74
6.5 Steps for obtaining ${}^{CT}T_{NDI}$ transformation matrix, during calibration process. . . . 75
6.6 Flowchart that describes the calculation of the position and orientation of drilling point in the robot coordinates. . . . 77
6.7 Block diagram of the open-loop robot control. . . . 78
6.8 Experimental setup. . . . 78
6.9 The Real Scenario of the femur phantom, the Us probe, and the drilling point in the femur head. . . . 80
6.10 Experimental apparatus. . . . 81
6.11 Results of image processing during the tracking of the femur. . . . 82
6.12 The registration process - calibration method 1. 3D Computed Tomography (CT) point cloud (green). Point cloud of the femur head, before registration (red). Point cloud of the femur head, after registration (black). . . . 82
6.13 The registration process - calibration method 2. 3D CT point cloud (green). US point cloud, before registration (red). US point cloud, after registration (black). . . . 82
6.14 Local registration highlighting - calibration method 1. . . . 83
6.15 Local registration highlighting - calibration method 2. . . . 83
6.16 The registration process, snapshot from the developed application. Left, before registration, and right, after registration. . . . 84
6.17 On-line local registration, highlighting. US point cloud, before local registration (red). US point cloud, after local registration (black), performed with Iterative Closest Point (ICP) method. . . . 85
6.18 On-line local registration. CT point cloud (green). US point cloud, after local registration (red). US point cloud, after local refinement (black), performed with Coherent Point Drift (CPD) method. . . . 85
6.19 Bone movements (Red) and robot movements (Blue) during an experiment, represented in XYZ coordinates. . . . 87

Glossary

Computed Tomography

Although also based on the variable absorption of X-rays by different tissues, computed tomography (CT) imaging, also known as ”CAT scanning” (Computerized Axial Tomography), provides a different form of imaging known as cross-sectional imaging. CT scans of internal organs, bone, soft tissue and blood vessels provide greater clarity and reveal more details than regular X-ray exams. Radiographs are two dimensional representations of three dimensional objects and CT provides images that show all three dimensions.

Hip Resurfacing

Hip Resurfacing arthroplasty is a bone-preserving procedure that helps restore comfort and function to patients’ hips damaged by degenerative joint disease (osteoarthritis rheumatoid arthritis and traumatic arthritis) avascular necrosis or developmental hip dysplasia. It is viewed as an alternative to traditional hip replacements for helping patients return to their active lifestyles.

Total Hip Replacement

Hip replacement surgery involves replacing components of the hip joint with a synthetic implant, to repair the damaged bearing surfaces that are causing pain. In a total hip replacement both the thigh bone (femur) and the socket are replaced with synthetic implant materials.

Ultrasound

Medical sonography (ultrasonography) is an ultrasound-based diagnostic medical imaging technique that use of high-frequency sound waves to create images of organs and systems within the body. Unlike with an X-ray or CT scan, there is no ionizing radiation exposure with this test. In diagnostic sonography, the ultrasound is usually between 2 and 18 MHz. Higher frequencies provide better quality images, but are more readily absorbed by the skin and other tissue, so they cannot penetrate as deeply as lower frequencies. Lower frequencies can penetrate deeper, but the image quality is inferior.

Acronyms

ANFIS	Adaptive Neural Fuzzy Inference Systems

CAOS	Computer-Assisted Orthopaedic Surgical
CAS	Computer-Assisted Surgery
CPD	Coherent Point Drift
CT	Computed Tomography
DICOM	Digital Imaging and Communications in Medicine
FMS	Fast Marching Segmentation
FOV	Field of View
GACS	Geodesic Active Contour Segmentation
HD	Hausdorff Distance
HR	Hip Resurfacing
ICP	Iterative Closest Point
IGSTK	Image-Guided Surgery Toolkit
ITK	Insight Segmentation and Registration Toolkit
MAP	Maximum a Posteriori
MHD	Modified Hausdorff Distance
MIP	Maximum Intensity Projection
MIS	Minimally Invasive Surgery
MISO	Multiple-input and Single-output
PCL	Point Cloud Library
RMSE	Root Mean Squared Error
ROI	Region of Interest
SDS	Shape Detection Segmentation
SPF	Signed Pressure Force
THR	Total Hip Replacement

TLSS	Threshold Lever Set Segmentation
TV	Total Variation
UDP	User Datagram Protocol
US	Ultrasound
USB	Universal Serial Bus
VTK	Visualization Toolkit

List of symbols

α	Alpha indicates a balloon force.
β_i	is the degree of activation of the i^{th} rule.
δ	Delta indicates an variation.
$\triangle$	$\triangle$ is the difference operator.
ε	ε indicates the motion errors.
f	*f* is a collection of fuzzy if-then rules.
$\mathbf{J}$	indicates the Jacobian.
λ	Lambda is a trade-off parameter.
Max	*Max* indicates the maximum value.
min	*min* indicates the minimum value.
$\mu_{A_{ij}}(x_j)$	is the membership function of the fuzzy set A_{ij}.
∇	Nabla indicates the Gradient Operator.
$norm$	indicates the norm of a vector.
Ω	Omega indicates the region boundary.
$P_k(z_k)$	is the potential of the data point z_k.
ϕ	Phi indicates the (x,y) contour coordinates.
$\dot{\mathbf{q}}(k)$	indicates the robot joint velocities.
$\mathbf{q}(k)$	indicates the robot joint positions.
R_i	is the i^{th} rule.
σ	Sigma indicates the standard deviation.
$\mathbf{x}$	indicates the data input vector.
y_i	indicates the data output vector.
$\hat{y}$	indicates the estimated output, from the model.

Chapter 1

Introduction

Health is the most important asset that the human being can have. The significant improvements of the humans life quality, over the years is only achieved because researchers constantly seek new solutions and new methods. The use of new technologies to assist medicine allows, to improve classical techniques and develop new solutions. These technologies also allows clinicians to improve clinical diagnosis, and assist them in clinical practice, e.g., during surgery. The main objective of the work presented in this thesis is the development of new techniques to assist surgeons, in orthopaedics, while improving accuracy and diminish surgical procedures time. For that, is proposed a new navigation system for a robot-assisted orthopaedic surgery, developed to be used in Hip Resurfacing (HR).

The surgical navigation is based on the patient's own CT imaging data to prepare surgical procedures before operation, i.e., to obtain the desired drilling point. During surgery, to achieve an accurate system to drill the femur head, the robot's surgical drill and femur movements must be tracked. The surgical drill is tracked through an opto-tracker system, while the femur movements are tracked also using US images. This real-time feedback allows to compensate the femur movements, during the robotic drilling, without incisions in the femur.

1.1 Background and Motivation

The research developed during this thesis addresses a current problem identified by the orthopaedic surgeons who perform HR surgeries. This problem consists in the amount of time spent, during surgery, to obtain the correct alignment to perform an implant in the femur head, with the current techniques. To find a solution to this problem is the main focus all the research undertaken in this thesis. This issue was also the motivation to improve the state of the art, and contribute for the developments in this scientific area, improving humans life quality.

An high number of patients with damaged hip have degenerative joint disease (osteoarthritis rheumatoid arthritis and traumatic arthritis) avascular necrosis or developmental hip dysplasia, Berry & Lieberman (2013). In most cases, the patient's quality of life improves significantly with an hip surgery.

Total Hip Replacement (THR) is one of the most successful orthopaedic interventions used. The femoral head is removed and replaced by a prosthesis. According to the surgeon Derrek McMinn, McMinn (2009), the THR procedure is reasonably successful in elderly, relatively inactive patients. However, replacement hip joints wear out quickly in younger, more active patients, leading to the revision surgery and associated complications.

HR is a bone preserving alternative method to THR, Muirhead-Allwood *et al.* (2008), which maintains the anatomical loading situation of the hip almost unaffected. It is viewed as an alternative to traditional THR for helping patients return to their active lifestyles. Observing Figure 1.1, significant differences are noted between the prostheses used in HR and THR. HR is a bone-conserving hip procedure contrary to THR. However, the HR surgical technique is considerably more demanding than THR. Retaining the neck and head of the femur, for instance, makes it much harder for the surgeon to expose the socket. Shaping the femoral head appropriately also takes practice and if the surgeon does that poorly, the patient is far more likely to suffer a femoral neck fracture.

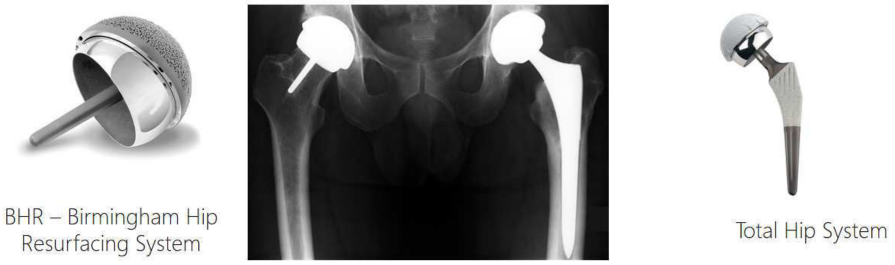

Figure 1.1: Prosthesis used in Hip Resurfacing and Total Hip Replacement.

In the Birmingham Hip Resurfacing surgery (designed in Birmingham by Derrek McMinn), the implant alignment is the most important pre-operative consideration for correct implant positioning. According to the surgical procedures, described in, Smith&Nephew (2008), and illustrated in figure 1.2, the correct positioning is obtained pre-operatively (step 1), and intra-operatively, the alignment is made from a very time consuming mechanically procedure (step 5), through a alignment guide (named McMinn Alignment Guide). A guide wire is inserted when the desired position of the alignment guide has been achieved (step 6). The guide wire ensures that the spherical metal cap is positioned correctly on the femoral head. The success of the surgery depends on the correct positioning of the guide wire.

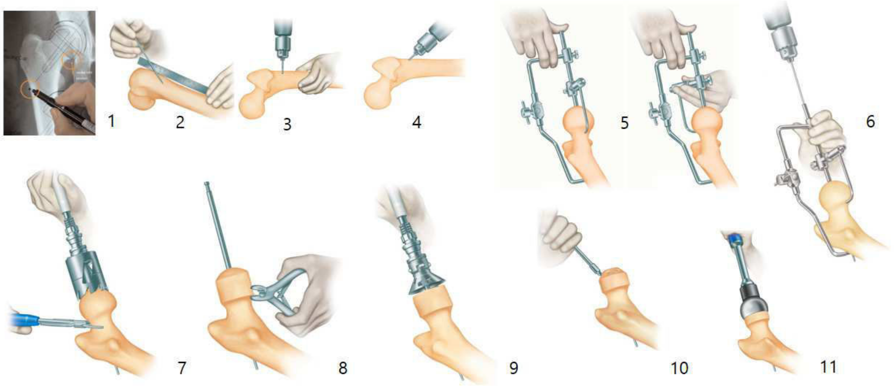

Figure 1.2: $smith\&nephew$, BIRMINGHAM HIP Resurfacing System (Extracted from Smith&Nephew (2008)).

Several studies have identified the malpositioning as a risk factor for femoral neck fracture after HR, Shimmin & Back (2005), Shimmin *et al.* (2005), Tapaninen *et al.* (2012), Matharu *et al.* (2013). Computer navigation systems, are an increasingly alternative to allow accurate placement of the femoral implant. Several studies comparing HR procedures performed using mechanical jigs and computer navigation systems, demonstrate that the computer navigation systems allows more accuracy, Davis *et al.* (2007), Hodgson *et al.* (2007), Ganapathi *et al.* (2009), Bailey *et al.* (2009). Improve the navigation systems and assist surgeons in the HR procedures is the greatest motivation of this thesis, i.e., to find a robotic solution that increase the accuracy and reduce post-operative complications associated with the technique.

1.2 State of the Art

Increasing advances in robotics have allowed the emergence of new systems dedicated to surgery, which began to be a valid option in surgical procedures. The computer-assisted surgery (CAS), Adams *et al.* (1990), and particularly the robot-assisted orthopaedic surgery, Kather *et al.* (2010), Mantwill *et al.* (2005), improves accuracy and precision of surgical procedures, besides producing more reliable and reproducible outcomes, minimizing the invasiveness of surgical procedures and to improve patient outcomes, by reducing complications and improving patient safety, compared with conventional orthopaedic techniques.

The use of robots to automate medical tasks increases its reliability, accuracy and are an excellent contribution to Minimally Invasive Surgery (MIS). MIS is becoming more and more common nowadays in hospitals. Surgical procedures are performed through tiny incisions instead of one large opening. Because the incisions are small, patients trend to have quicker recovery times and less discomfort than with conventional surgery. Last thirty years have been marked by the development of robotic systems for MIS. In 1985 a robot, the PUMA 560, Satava (2002), was used to place a needle for a brain biopsy using CT guidance. Three years later the same machine was used to perform a transurethral resection. In 1987 robotics was used in the first Laparoscopy surgery, a cholescystecotomy. In 1988, the PROBOT, Harris *et al.* (1997) developed at Imperial College London, was used to perform prostate surgery.

More recently appeared the ZEUS, DaVinci and DLR MIRO surgical systems. The ZEUS robotic surgical system, initially developed in 1995 for endoscopic microsurgery (including general surgery, thoracic surgery, gynaecology, urology), was the robotic system used in the first transatlantic surgical intervention performed on a human, in 2001 between New York and Strasbourg, France, at 15000 km of distance, Marescaux *et al.* (2001). The DaVinci Surgical System enables surgeons to operate through a few tiny incisions with dramatically enhanced vision, precision and control. State-of-the-art DaVinci Surgery helps surgeons to minimize the pain and risk associated with traditional surgery, while increasing the chances for a fast recovery and excellent clinical outcomes. DLR MIRO, Konietschke *et al.* (2009), Hagn *et al.* (2008), Matharu *et al.* (2013), is a compact, slim and lightweight (LWR) robotic system versatile for various existing and future medical robotic procedures. Can be used in orthopaedics to setting holes for bone screws, robot-assisted endoscope guidance and on to the multi-robot concept for (endoscopic) minimal invasive surgery.

In orthopaedics several solutions have emerged, such as ROBODOC, Kazanzides *et al.* (1995), for the planning and performance of total hip and knee replacement, CASPAR, Beasley (2012), developed for the same purpose of ROBODOC, Acrobot Sculptor, Cobb *et al.* (2006), Davies *et al.* (2007), used in knee surgery, or the RIO robotic arm (MAKOplasty), Pearle *et al.* (2009), the latest developed system for orthopaedics. The Robodoc surgical system consisted of the Orthodoc, Paul *et al.* (1992), pre-surgical planner and the Robodoc as the surgical tool. The Robodoc system comprises a five-axis Sankyo-Seiki industrial robot with a six degree-of-freedom force-sensor. The Orthodoc describes the three-dimensional geometry of the femur from CT data and the geometry of the implant.

The MAKO system consists of the well known general purpose WAM - Whole Arm Manipulator from Barrett Technology, Rooks (2006), for bone deburring, and an optical navigation system consisting of stereo infra-red cameras, and marker arrays attached to the tibia and femur. On the other hand, the Acrobot system uses their special purpose robot manipulator, where the tibia and femur are immobilized with bone clamps which are fixed through small skin incisions.

The increasing evolution of surgical robotic systems has also been accompanied for significant evolution in the surgical navigation systems, Stiehl *et al.* (2007). Of the several systems that have appeared in the market are highlighted the OrthoPilot, Miehlke *et al.* (2004), (`http://www.orthopilot.com`) and the BrainLAB systems, Gumprecht *et al.* (1999), (`https://www.brainlab.com`). Both systems employ markers placed on the femur for tracking the bone movements, Schulz *et al.* (2007).

Surgical navigation systems allow the surgeon to perform surgical actions in real time using information conveyed through a virtual world, which consist of computer-generated models of surgical instruments and the virtual representations of the anatomy being operated. Virtual representations can be generated from data obtained through Computer Tomography scans, ultrasound images, amongst others. Image-guided surgical navigation is on the rise in many different areas of medicine, with strong growth in orthopaedic surgery. The use of visual information obtained from medical images is widely used in Computer-Assisted Orthopaedic Surgical (CAOS) (`www.caos-international.org`). CAOS systems are increasingly available, with several commercial and research systems now well-established. These systems assist surgeons in pre-operative planning and simulation, from the obtained bone model, and in intra-operative navigation, using tracking systems with fiducial markers attached to the patient bone, and in the robotic execution of the surgical procedure. From the fiducial markers the position and orientation of the bone, in the intra-operative scenario, relative to the robot frame is obtained in the state-of-the-art systems, e.g., the BrainLab System or Orthopilot.

The incisions performed to place these markers, can leave serious injury to the patient. There are many cases of complaints of pain at the implant site after Surgery. Studies on the patients reported persistent severe pain at the site of pin implantation, after surgery, caused by the injuries to the nerves, result of the fiducial markers's implants, Nogler *et al.* (2001).

Recently, much scientific research work has been developed, with the purpose of eliminating fiducial markers in orthopaedic surgery, Amiot & Poulin (2004), Nabeyama *et al.* (2004), and the main guidelines of research focuses on the use of intra-operative US and pre-operative CT to provide real time surgical guidance. In Beitzel *et al.* (2012), it is presented a semi-automatic bone detection approach for US via registration with CT datasets pre-operatively acquired. The CT data is used to create a patient-specific bone model, and rigid transformation from US to CT are estimate by ICP algorithm, from a initializing of three points in the datasets. The three correspondence points, define the principal axis and orientation of the bone in both modalities. Moghari & Abolmaesumi (2007), propose a point-based registration algorithm based on unscented Kalman filter (UKF) to estimate the rigid transformation parameters between the bone surfaces obtained from US and CT data, less sensitive to outliers compared with ICP. Both methods are based on features of the datasets (feature-based), but there are also methods that use the image intensity information (intensity-based) directly in order to avoid extraction of bone surfaces. Penney *et al.* (2006), used normalized cross-correlation as a similarity metric for registering CT and US images. Prior to registration, both datasets were converted to bone probability images using gradient, bone intensity and US shadowing artefact information. More recently, in Hacihaliloglu *et al.* (2013), is proposed a rigid registration method where the translation parameters are estimated from the projections of local phase volumes in frequency domain. Bone surfaces were automatically extracted directly from 3D US and CT volumes based on 3D local image features calculated using 3D Log-Gabor filter.

Common drawbacks of these systems reside in the invasiveness of the bone tracking method. The innovative contribution of this thesis emerge to overcome this drawback: a tracking system for the femur which uses an optically tracked ultrasound probe, eliminating the extra skin and bone incisions for marker placement as well as the inaccuracies associated with their placement.

After its incipient experiments, ultrasound based visual servoing has recently gained new interest due to the establishment of visual servoing. Initial works consisted in the use of robot arms which manipulated an ultrasound probe for medical diagnoses, Abolmaesumi *et al.* (2002), Krupa & Chaumette (2006). The use of ultrasound also found its way into orthopaedics as a non-invasive radiation-free navigation system for surgeon operated, interventions, Chen & Ellis (2005). This is particularly valuable when the bones to be operated are so small, that it is not possible to attach heavy tracking targets onto them. For interventions cooperated by robot arms, effective applications using ultrasound guidance are not yet available, but an intense race involving research centers and industry is currently taking place.

Guiding a robot in positioning tasks through visual information using uncalibrated visual servoing systems is a very active research topic due to the complexity of real applications and workspace scenarios such as an operating room. The operating room can unpredictably change during a HR surgery, causing calibration errors. In Gonçalves *et al.* (2008), uncalibrated visual servoing was proposed, where the inverse system Jacobean was estimated on-line, thus immune to camera miss-calibration. It presents a very promising solution for the operating room, where it is also desired to minimize calibration time. Furthermore, this approach will give added robustness to a medical setting where the environment is calibrated, but redundancy is necessary for safety reasons. This work has been further extended to a more general case in, Gonçalves & Pinto (2008), where the uncalibrated model can evolve during the tasks to be performed. In Gonçalves & Fernandes (2008), tools for ultrasound based 3D Bone model reconstruction, registration and visualization are presented, which are currently being developed by the research team, in order to introduce ultrasound feedback in the visual control loop. In Gonçalves *et al.* (2009), was proposed and approach to obtain the position and orientation of a bone based in it's 3D model obtained from Computed Tomography images (in the preoperative scenario) and the registration of ecographic images to it (in the intra-operative scenario).

1.3 HipRob project

The current thesis was developed in the scope of the HipRob Project, (`http://www.echord.info/wikis/website/hiprob`), it emerges from the desire to develop a system that helps surgeons to perform HR prosthesis surgery. It is designed to aid surgeon to perform the initial drilling, necessary for guide wire implant. A co-manipulation robotic solution for HR surgery based on variable impedance control for physical surgeon-robot interaction will be developed. US images are used for non-invasive real-time bone tracking. The innovative co-manipulation setting to the medical gesture brings together the higher geometric accuracy and precision of the robot manipulator with the higher sensibility and decision making capability of the surgeon when applying force, thus resulting in clear benefits for patients, medical doctors and hospitals. For navigation, the system, during surgery, acquires a 3D US bone surface from a sequence of US images. This bone surface will then be registered to the pre-operative bone model, for a precise knowledge of the bone position and orientation. This registration is performed in two steps. The first, a global registration before the surgical procedure, to exactly register the bone. The second is to locally register the femur, which is faster and more suitable for tracking the bone movements. The measured bone movement is used by the robot manipulator to update its drilling position and orientation. Figure 1.3 shows an overview of the HipRob navigation system.

The avoidance of fiducial markers implies that the US probe is referenced to the optical measurement system (NDI - Polaris), (`http://www.ndigital.com/medical/`). This referencing is made by placing a marker in the US probe. From this moment, also the images and features are referenced to the tracker. The pose of the robot end-effector also has to be referenced by the Navigation system to inform the robot controller of its location. The ideal drilling point, is obtained pre-operatively in the CT reference frame. Inside the operating room, a initial calibration ($^{CT}T_{NDI}$) between the tracker (NDI) and CT is needed to localize the femur. After calibration, the main goal consists in to determine at each instant, the drilling point in the robot reference frame ($^{ROB}P_{drill}$) and track the bone movements with the robot.

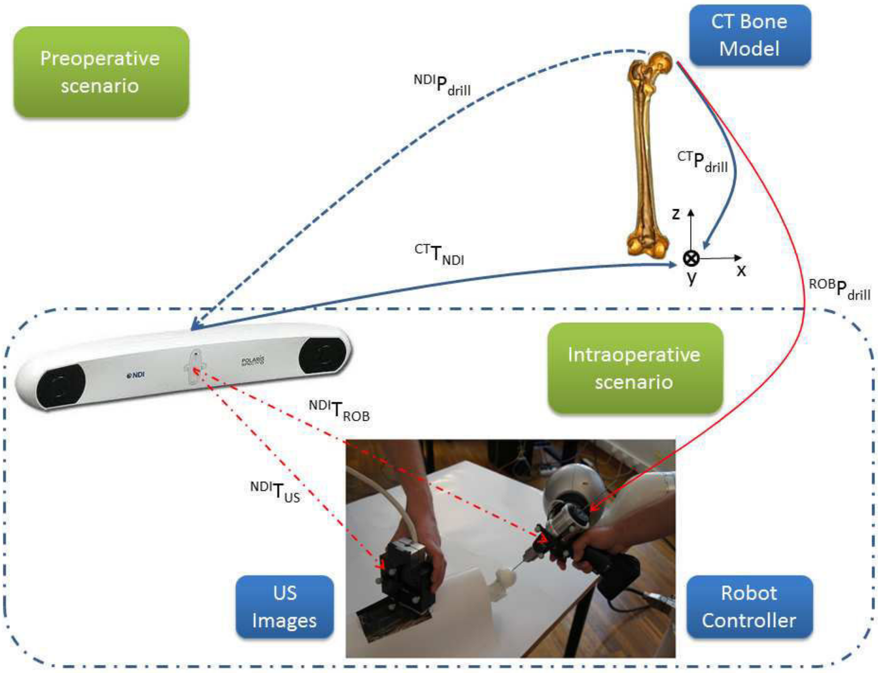
Preoperative scenario
CT Bone Model
$^{NDI}P_{drill}$
$^{CT}P_{drill}$
z
x
y
$^{CT}T_{NDI}$
$^{ROB}P_{drill}$
Intraoperative scenario
$^{NDI}T_{ROB}$
$^{NDI}T_{US}$
US Images
Robot Controller

Figure 1.3: Overview of the hardware setup and frames transformations of HipRob navigation system.

1.4 Objectives

In the doctoral plan three types of objectives were proposed, technical, sociological and multidisciplinary. First, are presented the technical objectives related to specific points of the scientific work which are outlined below:

- Position Based Visual Control of a robotic manipulator, using a high speed 3D optical tracking device - Polaris;
- Kinematic modelling between the imaging sensing devices, bone and robotic manipulator;
- Integration of the 3D Bone model based on CT in the navigation system;
- Ultrasound Based Visual Control of a robotic manipulator;
- Development of a laboratory prototype for experimental testing;

Secondly, are the sociological objectives related to the human factors of the project such as the improvement in people's health, particularly in the rehabilitation of patients with joint or bone related pathologies, and the benefits of less invasive surgeries and higher precision procedures. An example is the hip resurfacing surgical procedure stated in the State of the Art.

Finally there are the multidisciplinary objectives: the bringing together of two disciplines, Mechanical Engineering and orthopaedics, in order to improve bone related surgery. The traditional language used in both fields is different, and in this work will have to be brought together producing a common language that both fields may understand.

1.5 Contributions

During the development of this thesis some important contributions have been made:

- Two solutions are proposed to acquire, intra-operatively, US images spatially located. The first is a freehand system, where it is used the NDI Polaris opto-tracker to measure the position and orientation of the US probe. The Image-Guided Surgery Toolkit (IGSTK) toolkit is used to acquire and synchronize the images with the Polaris. The second solution is a non-freehand system, where the US probe is placed on the end-effector of an anthropomorphic robot arm. The robot is responsible to move the US probe along the leg and give a spatial location for each US slice of the bone.

- A new region-based approach for US images segmentation based on an existing algorithm, was proposed. Concretely was added a regulation term to block the contour's evolution to far from the initialization region, identifying only the desired object. Was also added a new condition to stop the segmentation method, and was used the output of previous segmentation as a mask to the next image, in the segmentation process. Both contributions improve significantly the processing times.

- Were developed and implemented some software tools for image segmentation, registration and visualization, useful both for surgical planning as for the intra-operative procedures.

- A new approach for US based robot navigation was developed. This approach uses registration algorithms to identify bone movements intra-operatively and updates at each instant the desired target's position and orientation. This approach is used to close the control loop for robotic motion compensation, using the 3D point clouds extracted from the contours of US images.

1.6 Publications

1.6.1 Book Chapters

1. **Pedro M. B. Torres**, Paulo J. S. Gonçalves, “Ultrasound Imaging for Robotic Orthopedic Surgery: A Survey”, Computer- Assisted Surgery: New Developments, Applications and Potential Hazards, Xiaojun Chen, (Ed.), Surgery - Procedures, Complications, and Results Series, Nova Publishers, 2015, ISBN: 978-1-63463-811-1;

2. P.J.S. Gonçalves, **P.M.B. Torres**, ”Visual Control of Robotic Manipulators: Fundamentals”, Robotics: State of the Art and Future Trends, L. Legnani, I. Fassi, (Eds.), Computer Science, Technology and Applications Series, Nova Publishers, 2012, ISBN: 978-1-62100-403-5;

1.6.2 Papers in Refereed International Journals

1. P.J.S. Gonçalves, **P.M.B. Torres**, F. Santos, R. Antonio, N. Catarino, J.M.M. Martins (2015) A Vision System for Robotic Ultrasound Guided Orthopaedic Surgery. Journal of Intelligent and Robotic Systems 77 (2) pp. 327-339. Springer Netherlands;

2. **P. M. B. Torres**, P. J. S. Gonçalves , J. M. M. Martins, ”3D Reconstruction and Visualization of Femur Bone Structures”, Romanian Review Precision Mechanics, Optics & Mechatronics, nr. 41, pp. 51-56, 2012;

3. **P. M. B. Torres**, P. J. S. Gonçalves , J. M. M. Martins, ”Robot Calibration for Precise Ultrasound Image Acquisition”, Romanian Review Precision Mechanics, Optics & Mechatronics, nr. 40, pp. 129-134, 2011;

4. P. J. S. Gonçalves, **P. M. B. Torres**, ”Extracting Bone Contours in Ultrasound Images: Energetic versus Probabilistic Methods”, Romanian Review Precision Mechanics, Optics & Mechatronics, nr. 37, pp. 105-110, 2010;

5. P. J. S. Gonçalves, M. V. Carvalho, D. F. A. Mateus, **P.M.B. Torres**, ”Registo de Imagens Ecográficas com Modelo 3D de Ossos aplicação ao fémur”, RISTI Revista Ibérica de Sistemas e Tecnologias de Informação, N.4, 12/2009, ISSN: 1646-9895, pp. 43-56;

1.6.3 Papers in Proceedings of International Conferences

1. **P.M.B. Torres**, P.J.S. Gonçalves, J.M.M. Martins, ”New Approach to the Open Loop Control for Surgical Robots Navigation”, Controlo 2014, 11th Portuguese Conference on Automatic Control, Porto, Portugal, 21-23 July 2014;

2. P. J. S. Gonçalves, **P. M. B. Torres**, J. M. M. Martins, ”Towards a Software Tool for Ultrasound Guided Robotic Hip Resurfacing Surgery”, ECHORD workshop in (IROS 2012), IEEE/RSJ International Conference on Intelligent Robots and Systems, Vilamoura, Portugal, 7-12 October 2012;

3. **P. M. B. Torres**, J. M. Sanches, P. J. S. Gonçalves, J. M. M. Martins, ”3D femur reconstruction using a robotized ultrasound probe,” Biomedical Robotics and Biomechatronics (BioRob), 2012 4th IEEE RAS & EMBS International Conference on , vol., no., pp.884-888, Rome, Italy, 24-27 June 2012, doi: 10.1109/BioRob.2012.6290782;

4. **P. M. B. Torres**, P. J. S. Gonçalves, J. M. M. Martins, ”Bone Registration using a Robotic Ultrasound Probe”, International Conference VipIMAGE 2011 - III ECCOMAS Thematic Conference on Computational Vision and Medical Image Processing, Olhão, Portugal, 12-14 October 2011;

5. **P. M. B. Torres**, P. J. S. Gonçalves, J. M. M. Martins, ”3-D Surface Registration of Ultrasound to CT-Bone Images”, Euromedia 2011, Workshop on Medical Imaging Systems, London, UK, 18-20 April 2011;

6. P. J. S. Gonçalves, **Pedro M.B. Torres**, ”Registration of Bone Ultrasound Images to CT Based 3D Bone Models ”,6th International Conference on Technology and Medical Sciences, Porto, Portugal, 21-23 October 2010;

7. **P. M. B. Torres**, P. J. S. Gonçalves, J. R. Caldas Pinto, ”Uncalibrated Stereo Visual Servo Control Using Fuzzy Models ”, Controlo’ 2010, 9th Portuguese Conference on Automatic Control, Coimbra, Portugal, 8-10 September 2010;

1.6.4 Papers in Proceedings of National Conferences

1. P.J.S. Gonçalves, **P.M.B. Torres**, J.M.M. Martins, ”Towards a Software Tool for Ultrasound Guided Robotic Hip Resurfacing Surgery”, ACM Symposium on Applied Computing 2013, Intelligent Robots track, Coimbra, Portugal, March 2013;

2. **Pedro M. B. Torres**, J. Miguel Sanches, Paulo J. S. Gonçalves, Jorge M. M. Martins, "Robotic 3D Ultrasound", Proceedings of RECPAD 2012, 18th Portuguese Conference on Pattern Recognition, Coimbra, Portugal, 26th October 2012;
3. Ruben António, P.J.S. Gonçalves, **P.M.B. Torres**, "Simulation of Ultrasound Guided Robotic Surgery with MORSE", Proceedings of RECPAD 2012, 18th Portuguese Conference on Pattern Recognition, Coimbra, Portugal, 26th October 2012;
4. Fábio Santos, P.J.S. Gonçalves, **P.M.B. Torres**, "3D Point Cloud Registration of the Femoral Bone, using the Point Cloud Library", Proceedings of RECPAD 2012, 18th Portuguese Conference on Pattern Recognition, Coimbra, Portugal, 26th October 2012;
5. Nuno M.M. Catarino, P.J.S. Gonçalves, **P.M.B. Torres**, "Bone Contour Segmentation from US Images - A Comparative Study", Proceedings of RECPAD 2012, 18th Portuguese Conference on Pattern Recognition, Coimbra, Portugal, 26th October 2012;
6. P. J. S. Gonçalves, **P. M. B. Torres**, "Femur Contour Extraction using Energetic and Probabilistic Models", Proceedings of RECPAD 2010, 16th Portuguese Conference on Pattern Recognition, Vila Real, Portugal, 29th October 2010;
7. P. J. S. Gonçalves, **P. M. B. Torres**, "The ICP Method Applied to Register US Images to 3D Bone Models", Proceedings of RECPAD 2010, 16th Portuguese Conference on Pattern Recognition, Vila Real, Portugal, 29th October 2010;

1.7 Outline of the Thesis

The remainder of this thesis is organized as follows: In the following chapter, the CT and US image acquisition procedures, are presented. The chapter describe the architecture of the freehand US acquisition system based on the optical tracker NDI Polaris Spectra and on the IGSTK toolkit. Is also described the non-freehand system for US image acquisition with a robot.

Chapter 3 presents the image processing tasks performed to extract the 3D point clouds from calibrated US and CT datasets. It is also described a new approach for medical imaging segmentation, that improves the computational speed. The last part of the chapter describes the 3D reconstruction and visualisation procedures form CT data, used in the pre-operative scenario.

In chapter 4 are presented the, multimodal point set registration procedures to register US with CT data. The classical ICP is described as well as a more recent approach called CPD method. These methods were compared regarding speed and accuracy, to justify the application in the final experimental system.

Chapter 5 describes the experiments performed with visual servoing to control a robot manipulator. The Visual Control is addressed when the sensing information, need to close the loop, is obtained from image features.

Chapter 6 describes the integration of all tasks previously presented in order to design a new approach for surgical navigation. The navigation is entirely based on the information extracted from image information. In real-time, the US point sets are registered with the model, constructed from CT, to obtain the femur displacements during surgery. In the chapter is also presented the experiments performed in a human femur phantom, which validate the proposed approaches in this thesis.

The last chapter (Chapter 7) presents the general conclusions achieved during the thesis development and proposals for future work.

Chapter 2

Image Acquisition

This chapter describes the important aspects of image acquisition, both ultrasound and CT. It is a background chapter, which describes the details of the acquisitions that will be subsequently considered in chapter 3, where is reported the image processing.

2.1 Ultrasound Image Acquisition

Ultrasound imaging provides a non-invasive and convenient technology that has recently benefited from the development of three-dimensional (3D) reconstruction techniques. Volume reconstruction of ultrasound images can be performed directly with 3D probes, more expensive, or by spatial measurement systems coupled to the conventional 2D ultrasound probe. Freehand and non freehand US acquisition systems, were developed in this work to perform 3D reconstruction across US images acquired in B-mode trough 2D US probes.

2.1.1 Freehand Ultrasound Acquisition System

In this subsection is presented a Freehand Acquisition System developed for acquisition of US images, properly referenced. This module is based on IGSTK (`http://www.igstk.org/`), a free open source C++ toolkit, that provides a framework for rapid prototyping of customized image-guided surgical applications. The toolkit provides a set of components common to general purpose navigation systems, such as interface with tracking systems, image registration and visualization though the Insight Segmentation and Registration Toolkit (ITK) (`http://www.itk.org/`) and Visualization Toolkit (VTK) (`http://www.vtk.org/`). For the acquisition system proposed in this thesis the integration of the Open Computer Vision library, OpenCV (`http://opencv.org/`), was also done to allow ultrasound image acquisition and processing from the US probe, through an Universal Serial Bus (USB) video capture. NDI Polaris Spectra is the sensor used to measure the pose of passive targets. Three different markers are used, one attached to the robot end-effector in order to measure the passive targets pose, presented in left side of figure 2.2 (ref. 8700339), other, on the US probe to measure the pixels 3D position, presented in right side of figure 2.2 (ref. 8700449), and the other free-hand (ref. 8700340), figure 2.2 c), to be used in marking some points of interest, e.g., perform palpation of the femur head. Each point in US images can be referenced to the NDI frame (${}^{NDI}P$), through the equation 1.

$$^{NDI}P =^{NDI} T_{Mk} \times^{Mk} T_{pr} \times^{pr} T_i \times^i P(u,v) \tag{1}$$

According to figure 2.1, ${}^{NDI}T_{Mk}$, represents the relationship between passive markers and Polaris system, ${}^{Mk}T_{pr}$, represents the relationship between the US probe extremity and Marker, ${}^{pr}T_i$ corresponds to the relationship between the image plane and US probe, and finally, ${}^{i}P(u,v)$ represents a point in the US image. The transformations ${}^{Mk}T_{pr}$ and ${}^{pr}T_i$, depicted in figure 2.1, are previously calibrated off-line.

To obtain the marker's position and orientation, the *igstk::Transform* class was used. This class represents relative positions and orientations in 3D space. It is intended to be used for positioning objects in the scene, since it is a means of communication between trackers and spatial objects. The Translational component is obtained from the function " *GetTranslation()* " (*igstk::Transform::GetTranslation()*), and Rotational component is obtained from the function " *GetRotation()* " (*igstk::Transform::GetRotation()*). 3D position of each point is obtained in [mm], and orientation is provided in quaternion, format [Qx, Qy, Qz, Qw], or in the form of rotation matrix. With the position and orientation components is defined the homogeneous transformation matrix that relates the pose of the marker in 3D space, referenced in the Polaris frame, according to the equation 2.

$$^{NDI}T_{Mk} = \begin{pmatrix} ^{NDI}R_{3\times3} & ^{NDI}t_{3\times1} \\ 0_{3\times3} & 1 \end{pmatrix} \tag{2}$$

To obtain the matrix that relates the center of the US probe, to the passive marker reference frame, it is important to know the translation offsets in X ($px1$), Y ($py1$) and Z ($pz1$). These offsets

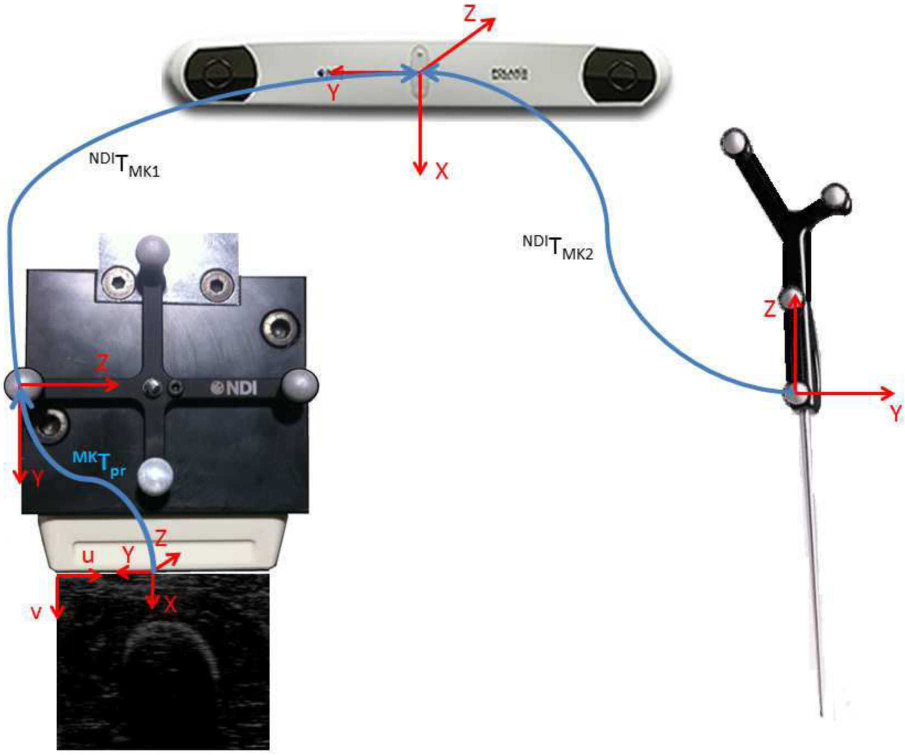

Figure 2.1: Optical Tracking System and coordinate frames used in image acquisition process.

are obtained thought metric measurements, and confirmed using the free-hand marker. The matrix in equation 3, represents the calibration matrix, obtained, where $px1$, $py1$ and $pz1$ are expressed in [mm]. The rotation component is defined by the identity matrix, because the US probe is aligned with the marker and there is no rotation component.

$$^{Mk}T_{pr} = \begin{pmatrix} 1 & 0 & 0 & px1 \\ 0 & 1 & 0 & py1 \\ 0 & 0 & 1 & pz1 \\ 0 & 0 & 0 & 1 \end{pmatrix} = \begin{pmatrix} 1 & 0 & 0 & -35,0000 \\ 0 & 1 & 0 & 65,9800 \\ 0 & 0 & 1 & 41,4878 \\ 0 & 0 & 0 & 1 \end{pmatrix} \tag{3}$$

Equation 4 ($^{pr}T_i$), relates the US image plane to the US probe reference frame.

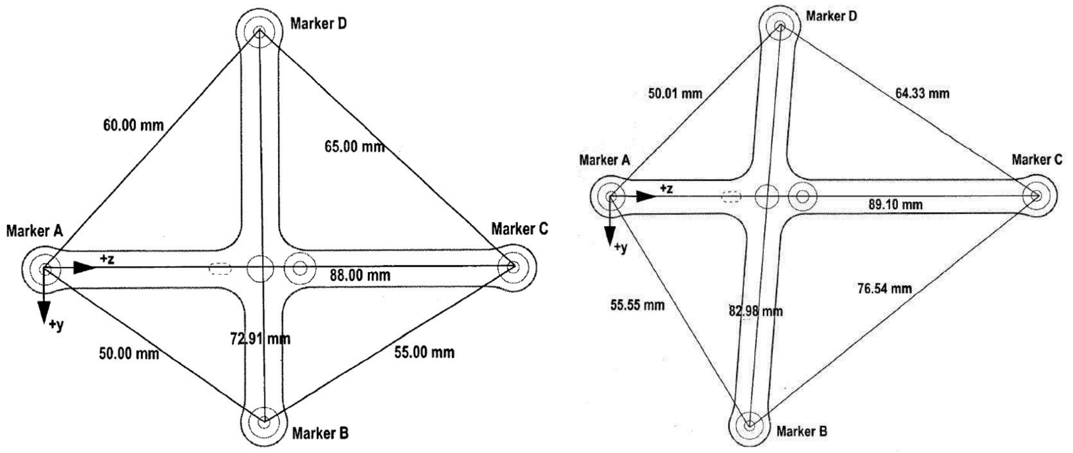
Marker D
60.00 mm
65.00 mm
Marker A
Marker C
+z
88.00 mm
+y
72.91 mm
50.00 mm
55.00 mm
Marker B
Marker D
50.01 mm
64.33 mm
Marker A
Marker C
+z
89.10 mm
+y
55.55 mm
82.98 mm
76.54 mm
Marker B

(a) Marker 8700339 layout.

(b) Marker 8700449 layout.

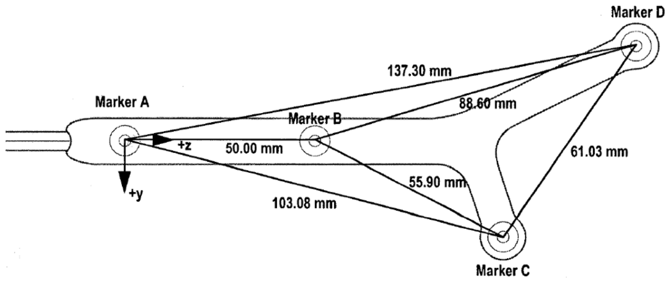
Marker D
137.30 mm
Marker A
88.60 mm
Marker B
+z
50.00 mm
61.03 mm
+y
55.90 mm
103.08 mm
Marker C

(c) Marker 8700340 layout.

Figure 2.2: Tools Specifications, extracted from the Polaris Spectra Tool Kit Guide.

$$
{}^{pr}T_i = \begin{pmatrix} 0 & 0 & 1 & 0 \\ 0 & 1 & 0 & 0 \\ -1 & 0 & 0 & 0 \\ 0 & 0 & 0 & 1 \end{pmatrix} \tag{4}
$$

$P(u, v)$ represents any point in US image, u_i and v_i are the pixel coordinates and u_0, the coordinate of the center, obtained from calibration. S_x and S_y are the scale factors, two of the US imaging device intrinsic parameters, obtained from calibration. CIRS Ultrasound Calibration Phantom, model 555 (`http://www.cirsinc.com`) was used to obtain these scale factors. This Phantom is a cube with a small egg and a large egg. There are two scanning surfaces and the targets are centred within the background material. Knowing the dimensions of each egg, it is possible to obtain the relationship $pixels/mm$ for each level of depth of the US equipment and calculate the scale factors.

$$P(u,v) \quad = \quad \begin{pmatrix} S_x(u_i - u_0) \\ S_y(v_i) \\ 0 \\ 1 \end{pmatrix} \tag{5}$$

2.1.2 Non Freehand Ultrasound Acquisition System

A significant amount of scientific work has been produced in order to acquire US images with the aid of automatic mechanisms, such as robots, Abolmaesumi *et al.* (2000), Mebarki *et al.* (2010). The concept of Ultrasound Visual Servoing, Mebarki *et al.* (2008), Bachta & Krupa (2006), is a theme that has shown good results in the control of probe positioning, with practical application in different areas, helping technicians and automating the diagnosis based on ultrasound images.

This subsection presents a non freehand US acquisition system, where the probe displacement and position are accurately controlled by an anthropomorphic robot. The aim of this system is to acquire a sequence of 2D parallel cross-sections evenly spaced along the displacement direction in order to perform an accurate 3D reconstruction of the femur. The robotic system used, consists of an Eurobtec IR52C robot manipulator. The probe is placed in the end effector of the robot, responsible for positioning the probe in contact with the femur. The images were acquired and the femur scanned with the best possible coupling at a constant speed. In the preparation of each experiment is necessary to define the pose of the robot that guarantees the best coupling between the probe and the femur, without hurting the patient. Initial and final points of acquisition must be defined, to perform trajectory planning along the femur. Whenever possible, trying to make linear trajectories. The estimation of the hand-eye and the robot-world transformations, to know the positioning of the probe at every moment, is an important point of this work. These estimations allow to perform a precise three-dimensional reconstruction of the bone. Each point in US images can be referenced to the world frame (${}^{w}P$), through the equation 6.

$${}^{w}P = {}^{w}T_b \times {}^{b}T_e \times {}^{e}T_{pr} \times {}^{pr}T_i \times {}^{i}P(u,v) \tag{6}$$

According to figure 2.3(a), ${}^{w}T_b$ represents the relationship between the base of the robot and the position coordinates in the world frame (equation 7) , ${}^{b}T_e$ is the relation between the robot end-effector and its base, computed from the robot kinematics, ${}^{e}T_{pr}$ represents the relationship between the US probe extremity and the robot end-effector (equation 8), ${}^{pr}T_i$ corresponds to the relationship between the image plane and US probe (equation 4), and finally, ${}^{i}P(u, v)$ represents a point in the US images, the same matrix used in the freehand system, equation 5.

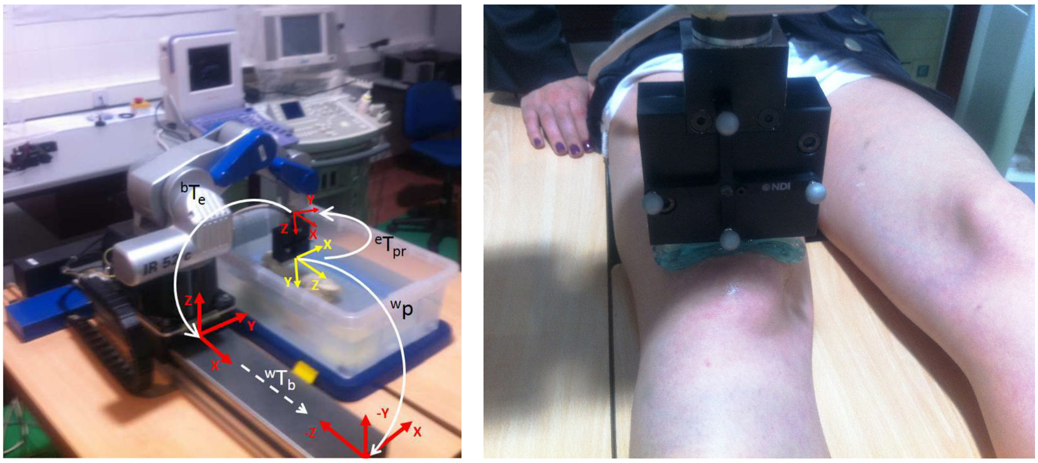

(a) Robot with frames used in calibration. (b) Acquisition Details in a human femur.

Figure 2.3: Robotic 3D US system.

$$
{}^{w}T_{b} = \begin{pmatrix} 0 & 0 & 1 & 0 \\ 0 & 1 & 0 & 0 \\ 0 & -1 & 0 & pz \\ 0 & 0 & 0 & 1 \end{pmatrix} \tag{7}
$$

where pz corresponds to robot movement, in mm, along to its linear axis.

$$
{}^{e}T_{pr} = \begin{pmatrix} 0 & 1 & 0 & 0 \\ 0 & 0 & 1 & 0 \\ 1 & 0 & 0 & 135 \\ 0 & 0 & 0 & 1 \end{pmatrix} \tag{8}
$$

With this system, various tests were performed in the laboratory, first with a cow femur bone within a tank of water and after in human femurs. Figure 2.3(a) shows the experimental apparatus during the scan of a cow femur and in Figure 2.3(b), where it can be seen in detail an acquisition to a human femur.

2.2 CT Image Acquisition

Two acquisitions of CT images were performed during the thesis, first with a cow femur bone to preliminary tests and second with a human femur. Both acquisitions were performed with a Siemens SOMATOM Sensation 16 CT scanner in a medical imaging center, with a slice thickness of $0.75\ [mm]$ and a spacial resolution of 512×512 pixels. The acquisition of human femur was performed with a Field of View (FOV) of $185\ [mm]$, pitch of 0.5 and reconstruction interval of $0.1\ [mm]$. In this acquisition, 4913 images were stored in Digital Imaging and Communications in Medicine (DICOM) standard format, which is equivalent to $491.3\ [mm]$ (4913×0.1) of femur. This specifications are important to determine the reconstruction parameters. FOV represents the maximum size of the object under study, in this case the femur. Since the image matrix size is 512×512, the pixel size (ps), is obtained from the relation between FOV and matrix size (M), according equation 9.

$$ps = \frac{FOV}{M} = \frac{185}{512} = 0.3613[mm] \tag{9}$$

Chapter 3

Image Processing

Ultrasound and CT images of femur can be used to eliminate the bone incisions to attach the fiducial markers in orthopaedic surgery, and to extract the position and orientation of the bone for robotic navigation during the surgical procedure. For that, image processing is an important task in this work. This chapter presents the US and CT image processing steps for identify the bone contours from images and extract the point clouds for the registration process presented in chapter 4.

3.1 Ultrasound Image Processing and Segmentation

Since the bone is a rigid anatomical structure, ultrasound signals are reflected, and the image only captures the top layer of the bone. Processing this type of images is a challenging task, since images are very noisy and blurred. The image quality decreases severely when approaching the knee, because there is less muscle mass. When the bone gets closer to the probe, the US reflections are more intense. Other issue is the difficulty of coupling the probe to the knee, reducing the image quality.

Image *Denoising* was used to remove the noise that degrades the images, e.g., Speckle, the most common noise in US images. The objective is to smooth homogeneous areas while preserving the contours without distorting the images. The algorithm used is based on the Maximum a Posteriori (MAP) criterion with a Total Variation (TV) edge-preserving Gibbs prior. The method is formulated as an optimization task that is solved by the Sylvester equation, developed by Sanches *et al.* (2008).

To extract bone contours in all images, several tests were performed with energetic and probabilistic methods, Gonçalves & Torres (2010), and Catarino *et al.* (2012). However it was extremely difficult to extract the bone with significant precision. In 2010, Zhang *et al.* (2010), presented an Active Contour method, that conjugates the benefits of edge-based methods (Geometric Active Contour models, Sandhu *et al.* (2008)) and region-based methods (*Chan-Vese* algorithm, Chan & Vese (2001)). Methods based on the contour (edge-based), have some limitations and fail when the initialization is far from the object. The tests performed with this type of algorithms demonstrates that less careful initialization, results in a poor bone segmentation. With region-based methods, as the *Chan-Vese* and related, the statistical information inside and outside the contour is used to control its evolution, making it less sensitive to the noise. This method presents good results even for images with weak or blurred contours, besides being less sensitive to initialization. The method was applied to an image, after *Denoising*, but several objects were identified in the image beyond the region of interest, i.e., the bone. In fact, several regions in the images with pixel intensity similar to the bone, leading to similar values for known statistical metrics, even if the initialization is a square around the bone contour of interest.

To obtain accurate results for the problem at hand, it is necessary to understand where is the bone region and apply a regulation term to the forces function, that control the contour evolution, and lock evolutions far from the original mask. The next subsection describes the algorithm implemented and new contributions to segment ultrasound images of the femur.

3.1.1 Segmentation Method

The method proposed by Zhang *et al.* (2010), uses the statistical information inside and outside the contour to construct a region-based Signed Pressure Force (SPF) function in order to define the contour, described in equation 10. The signed pressure force modulates the signs of the pressure forces inside and outside the region of interest so that the contour shrinks when outside the object, or expands when inside the object.

$$spf(I(u,v)) = \frac{I(u,v) - \frac{c_1+c_2}{2}}{\max(|I(u,v) - \frac{c_1+c_2}{2}|)} \tag{10}$$

where $I(u,v)$ is the image with (u,v) coordinate pixels. c_1 and c_2 are two constants which are the average intensities inside and outside the contour, respectively, obtained from minimization of *Chan-Vese* energy function defined by equation 11.

$$E^{CV} = \lambda_1 \int_{inside(C)} |I(u,v) - c_1|^2 dudv + \lambda_2 \int_{outside(C)} |I(u,v) - c_2|^2 dudv \tag{11}$$

λ are fixed parameters, determined by the user.

$$c_1(\phi) = \frac{\int_\Omega I(u,v) \cdot H(\phi) dudv}{\int_\Omega H(\phi) dudv} \tag{12}$$

$$c_2(\phi) = \frac{\int_\Omega I(u,v) \cdot (1 - H(\phi)) dudv}{\int_\Omega (1 - H(\phi)) dudv} \tag{13}$$

$H(\phi)$ is the Heaviside function of the contour coordinates ϕ and Ω the region boundary. The author also proposes a new level set formulation to extract the contour, formulated by equation 14 and explained in Zhang *et al.* (2010).

$$\frac{\partial \phi}{\partial t} = spf(I(u,v)) \cdot \alpha \mid \nabla \phi \mid \tag{14}$$

where α is the balloon force, which controls the contour shrinking or expanding, and ∇ is the gradient operator. The method present a high potential to segment the bone in US images, but the low contrast between regions sometimes leads to errors and the segmentation of other objects in image.

It is important to define a regulation term to the forces function, that control the contour, and lock evolutions far from the original mask. Furthermore a new method to stop the contour evolution was implemented. The intensities inside and outside the contour are controlled to maximize the relations between them and the contour evolution stops only when the parameters converge, eliminating the number of iterations to define when the algorithm stops, used by Zhang *et al.* (2010). With this approach the processing time and the segmentation precision was improved, since the images are different, e.g. one image may need 50 iterations to converge while another requires only 5 iterations. The method converge when:

$$c_2(i) - c_1(i) = c_2(i-1) - c_1(i-1) \tag{15}$$

This means that, as from a given instant the values of c_1 and c_2 tend to stabilize and the contour presents no evolution, the algorithm can be stopped because it will not change the contour, i.e. the method converged. So it was improved the processing times and accuracy of segmentation.

Algorithm

1. Initialization ($\phi(u, v), t = 0$): Define a square in the region of interest, where the values inside are $\phi(u, v) = 1$ and outside $\phi(u, v) = -1$;
2. Compute $c_1(\phi)$ and $c_2(\phi)$, according equations 12 and 13;
3. Evolve the level set function according equation 14
4. Let $\phi(u, v) = 1$ if $\phi(u, v) > 0$; otherwise $\phi(u, v) = -1$
5. Regularize the level set function with a Gaussian filter: $\phi(u, v) = \phi(u, v) * G_\sigma$
6. If method converge (condition term, 15) $\phi(u, v)$ represents the image segmentation; Else, return to the step 2;

End Algorithm

$\phi(u, v) = \phi(u, v) * G_\sigma$ is the convolution of local segmentation with a Gaussian filter, where the standard deviation (σ) influences the sensitivity of the algorithm for the noise. Flowchart of figure 3.1, helps to understand the method used to segment all US images.

3.1.2 Image Processing and Segmentation Results

Many experiments were performed with freehand and non freehand systems described in chapter 2, first with a cow femur bone in a water tank and after in human femurs. This subsection presents the experimental image processing and segmentation results, obtained from the processing of 245 US images of a human femur, acquired with the non freehand system, but with the spatial location of the probe performed by the Polaris optical tracking system. In this experiment a girl's leg was scanned, on the central part of the leg from the hip to the knee with an ALOKA prosound 2 echograph with a $5\ MHz$ probe. All images were acquired with a resolution of 720×576 pixels with an image plane of $6\ [cm]$ (R06 - mean that one scale division, on image is equal to $0.5\ [cm]$), and a probe frequency of $7.5\ MHz$. Figure 3.2 a), represents an US image of the central part of femur.

The first step is to identify the Region of Interest (ROI) and clean the images with the *Denoising* method developed by Sanches *et al.* (2008). Figure 3.2(b) shows the region of interest defined

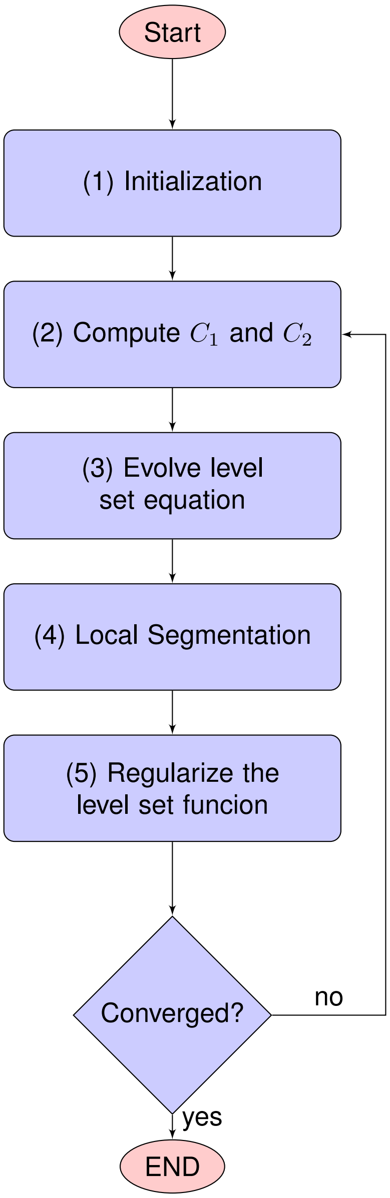
Start
(1) Initialization
(2) Compute C_1 and C_2
(3) Evolve level set equation
(4) Local Segmentation
(5) Regularize the level set funcion
Converged?
no
yes
END

Figure 3.1: Segmentation Algorithm Flowchart.

and the result after applying the *Denoising* algorithm for image 3.2(a). The processing time in the images cleaning is relatively high, an average of 3.8181 seconds per ROI of image, however facilitates the segmentation process and increases its accuracy. Previous laboratory tests without applying this cleaning method show that it is extremely difficult to achieve bone segmentation in an automated way.

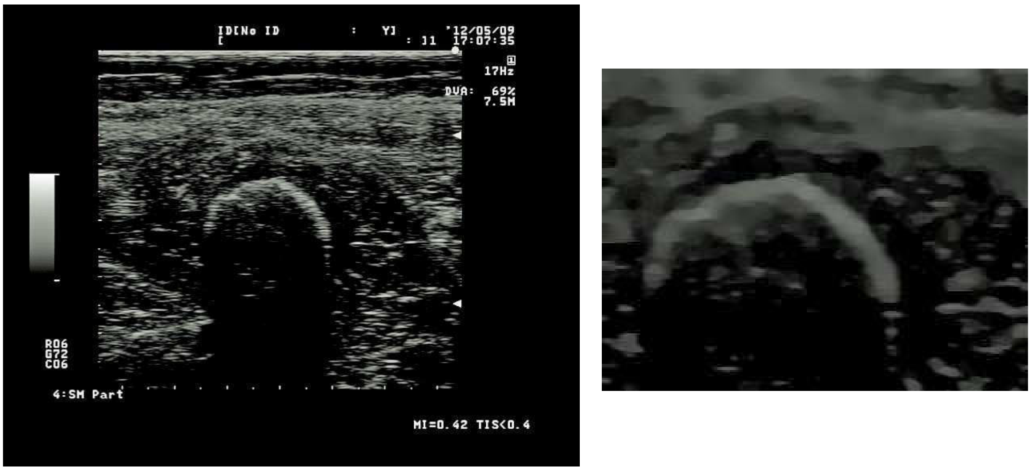

(a) US Bone Image. (b) Denoising Result, in the region of interest.

Figure 3.2: Ultrasound image before and after denoising process.

The graph in Figure 3.3 represents the evolution processing time, for cleaning all 245 images. As can be seen, the first image requires more time to converge. For the next images the processing time is significantly lower, because the algorithm use information from previous result, as input to the following images.

After cleaning, all the images are segmented using the method described in subsection 3.1.1. To reduce segmentation processing time of a set of images, the output result of a previous image is the input mask to the next image. Figure 3.4(a) shows the segmentation result of the image with index 100 (figure 3.2(a)). The initialization is performed in the image with index 1. To evaluate the results, the contour extracted is overlayed on the original image as seen in Figure 3.4(b). The bone was identified, despite the segmentation being performed in blurred images. Similar results are obtained to all images in the dataset. On average, 0.1779 seconds and 15.1265 iterations are needed to segment each image in the dataset, with this method.

The graph in Figure 3.5 represents the segmentation time and the number of iterations performed by the method to segment all 245 images. All experiments were performed in *MATLAB*, with an Intel Core 2 Duo, 2.27 GHz computer, with 4 GB RAM.

To understand bone in segmented images and identify its bone boundary, some experiments

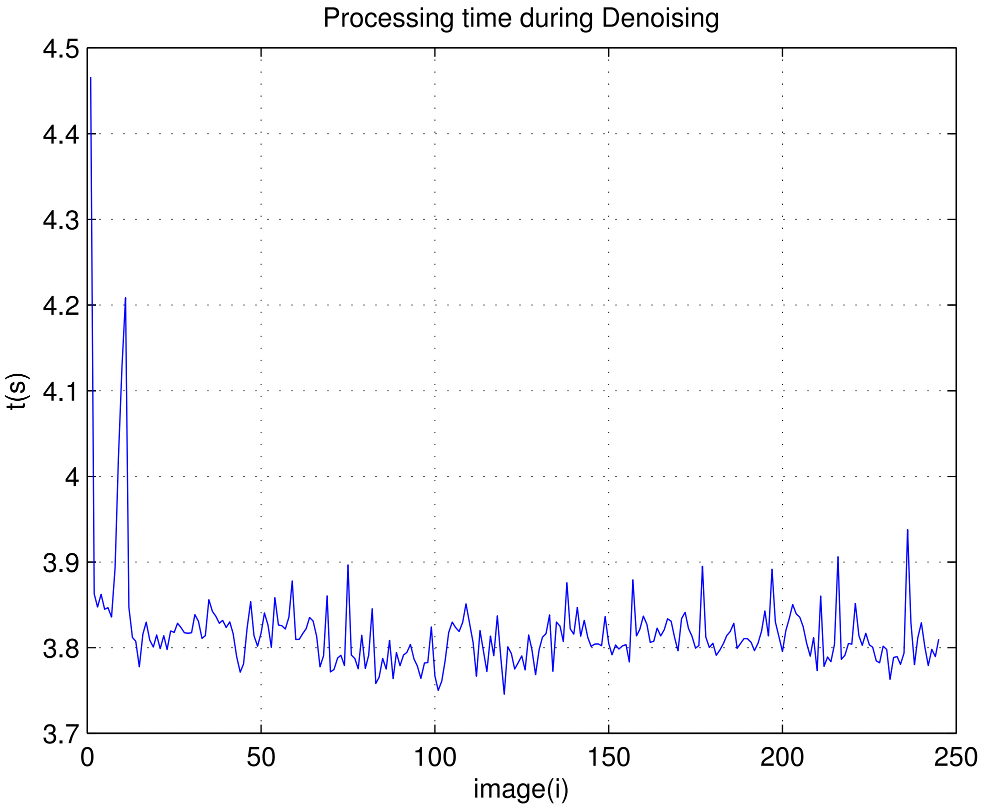

Figure 3.3: Evolution of Processing time during Denoising.

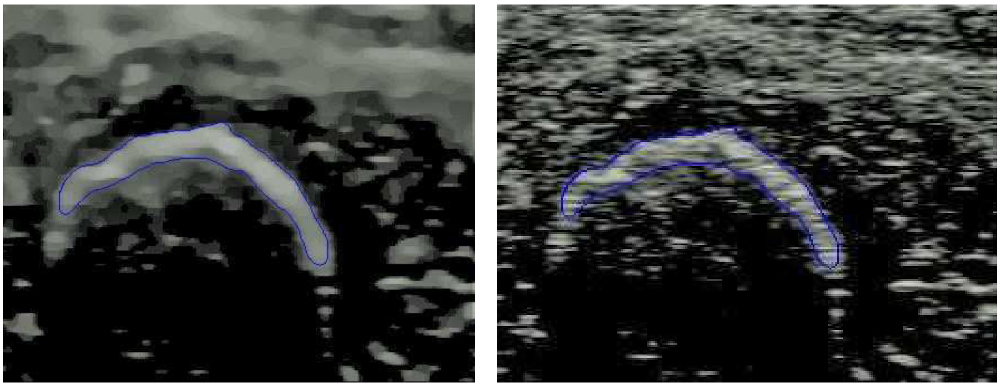

(a) Bone segmentation.

(b) Bone identification in the original image.

Figure 3.4: Result of segmentation in US image and contour overlay on the original image.

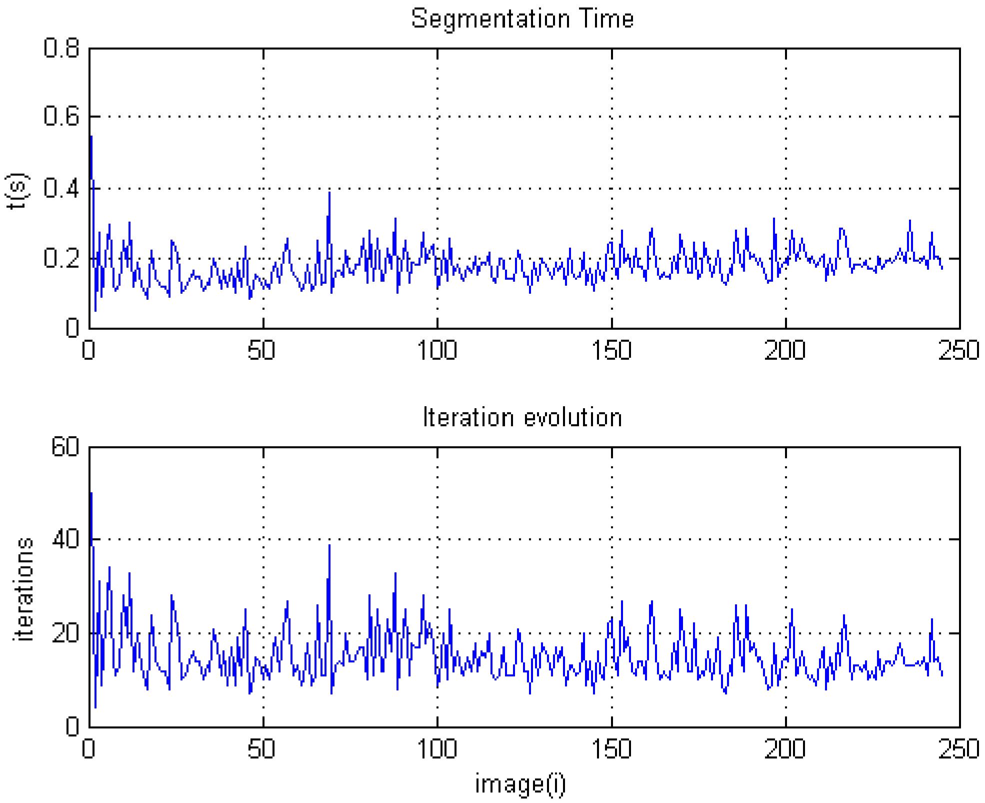

Figure 3.5: Segmentation time evolution and number of iterations need in each image.

were performed with a cow femur, a steak and a needle. As can seen in figure 3.6, when a needle penetrates the steak on the bone, does not penetrates the stain, finding the bone in the upper surface of image. Therefore, only the upper surface of the femur (open contour) is extracted from images, after segmentation.

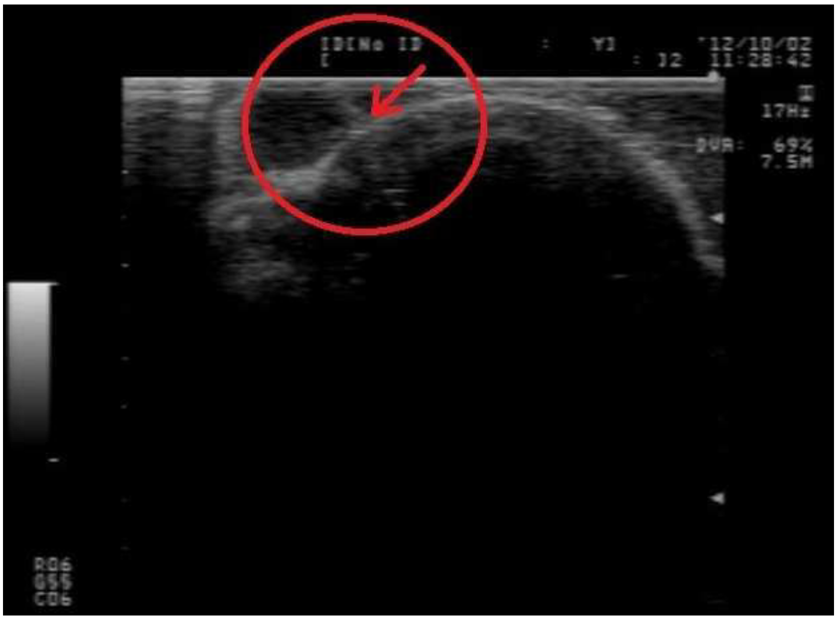

Figure 3.6: Surface detection in US images through a needle.

Root Mean Squared Error (RMSE) (equation 16) and Mahalanobis distance (M_D) (equation 17) were used to analyse the performance of the segmentation method, when applied to the upper contours of all images.

$$RMSE(i) = \sqrt{\frac{\sum(vg - ve)^2}{n}} \tag{16}$$

$$M_D(i) = \sqrt{(vg - \mu g)^T S^{-1} (ve - \mu e)} \tag{17}$$

vg are the ground-truth values (obtained manually), ve are the estimated values (obtained thought segmentation) and n is the number of points in each image contour. Since vg and ve can have different sizes, a cubic spline was used to interpolate both contours, allowing them to have the same size.

The quantification of segmentation errors, obtained with the proposed segmentation method are presented in table 3.1. The errors were calculated between the 245 segmented contours and the correspondent contours manually extracted. Is taken into account that manual extraction of contours in medical images requires expert knowledge and the extraction is influenced by the variability of the human observer, which limits its reliability, then extracting also contains errors. However, this is the way to compare the efficiency of the method. Figure 3.7 shows the point cloud extracted from the upper contour through segmentation method (ve) and manually (vg) of the ultrasound image of figure 3.2(a).

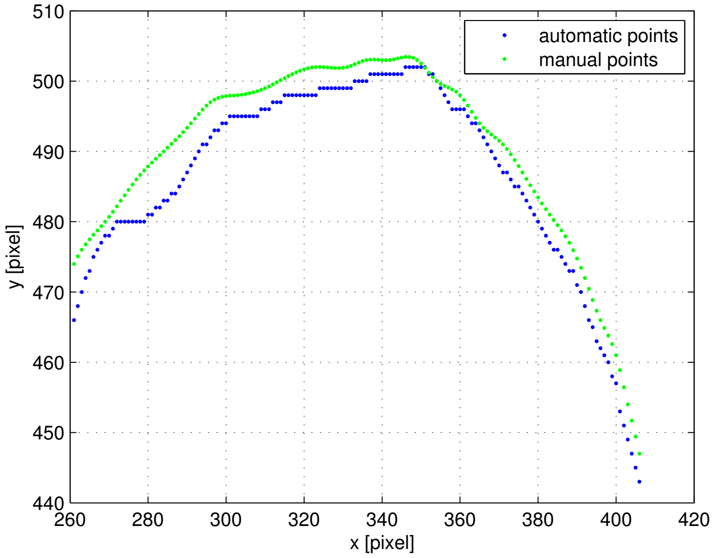

Figure 3.7: Points of a contour extracted from a manual segmentation (green) and through the proposed method (blue).

By comparison of tests performed with other algorithms published in, Catarino *et al.* (2012), and presented in table 3.1, is concluded that the proposed method has better results, in terms of accuracy. In all experiments presented in Catarino *et al.* (2012), the image cleaning process is based on average filters, no considering the *Denoising* algorithm presented above.

$\overline{RMSE}$ is the average of root mean square error, calculated across equation 16, in all images. σ_{RMSE} is the RMSE standard deviation. $\overline{M_D}$ is the average of Mahalanobis distance, calculated across equation 17. σ_{M_D} is the Mahalanobis standard deviation. Methods tested were:

- Fast Marching Segmentation (FMS) (Sethian (1996)) - This Level Set approach propagates a contour from a user-provided initial level set. The contour advances with a speed computed from the intensity of the input image gradient magnitude.
- Shape Detection Segmentation (SDS) (Malladi *et al.* (1995)) - This Level Set approach propagates a contour from a user-provided initial level set. The contour evolution controlled

by a partial differential equation using the gradient of the input image and also the contour curvature.

- Geodesic Active Contour Segmentation (GACS) (V. Caselles & Sapiro (1997)) - The geodesic approach for object segmentation allows to connect classical ”snakes” based on energy minimization and geometric active contours based on the theory of curve evolution.
- Threshold Lever Set Segmentation (TLSS) (Ibáñez Luis & Josh (2005)) - The goal is to define a range of intensity values that classify the bone of interest and then base the propagation term on the level set equation for that intensity range. Using the level set approach, the smoothness of the evolving surface can be constrained to prevent some of the ”leaking” that is common in connected-component schemes.
- Minimization of Region-Scalable Fitting Energy for Image Segmentation (MRIS) (Li *et al.* (2008)) - Is a region-based active contour model that draws upon intensity information in local regions at a controllable scale. The proposed model is able to segment images with intensity inhomogeneity, and has desirable performance for images with weak object boundaries.

Table 3.1: Quantification of segmentation errors

Method	$\overline{RMSE}[pixel]$	σ_{RMSE}	$\overline{M_D}[pixel]$	σ_{M_D}
Proposed	2.8099	0.7140	1.4766	0.0448
FMS	6.9054	2.0732	1.5318	0.1614
SDS	7.9454	2.5378	1.6237	0.2202
GACS	10.6508	3.2568	1.8186	0.3132
TLSS	2.8494	0.8001	1.4784	0.0453
MRIS	2.9428	0.9123	1.4990	0.0465

3.1.3 Point Cloud Extraction

The point clouds are an important way of three-dimensional data representation. A representation by point clouds simplifies the physical object and highlights the object’s shape, showing only the most relevant information. To represent point clouds referring the reconstruction of 3D US images is necessary to spatially locate each image pixel, for a given reference frame. This work presents two ways for locating the ultrasound images, properly explained in chapter 2. Freehand system, provides better accuracy, therefore has been widely used. To extract the points of interest in US images, the contour obtained in each slice and described in subsection 3.1.2, are related with calibration equations, presented in section 2.1.1, to give the position in the NDI frame.

The only unknowns parameters, are the scale factors S_x and S_y, which are calculated according to the specifications of the acquisitions. These parameters are obtained from a calibration phantom, off-line, or by calculating the pixels/mm relation, knowing the size of image plane and the number of pixels associated. For example, the acquisition used in section 3.1.2, was performed with an image plane of $6\ [cm]$ and this size corresponds to 420 pixels both in x and in y, so S_x and S_y are equal to $0.1429\ [mm]$. Figure 3.8 shows the ultrasound point cloud, extracted from the contours of all 245 images, with coordinates x, y and z oriented according to the referential of NDI tracker.

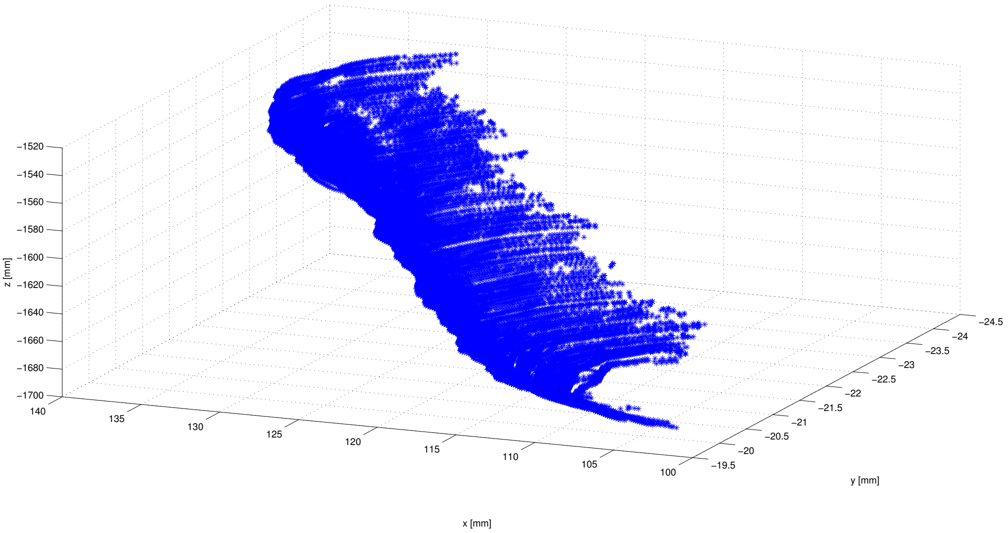

Figure 3.8: Point cloud extracted from ultrasound images, referenced to the polaris referential frame.

3.2 Processing and Segmentation of CT Images

The femur CT images have better quality than ultrasound images, however have a low contrast and the femoral head overlapping the pelvic bone. It is important to adjust the image intensities and automatically get the 2D femur contour of each slice and get a clear edge of the femur head, eliminating the pelvic zone. Several methods was used to extract the femur head, such as presented in wei Song *et al.* (2007), Baniasadipour *et al.* (2007) and Morar *et al.* (2012).

A popular method to extract such objects from a CT is global thresholding, in which the threshold value is determined from the image histogram. However, accurate threshold selection is not straightforward, especially in the area of the head of the femur, where we have similar intensity levels in various image objects.

In regions where two objects are identified clearly, as in Figure 3.9(a), the threshold method works. In this example the figure represents the femur (left object) and pelvic area (right object). After segmentation, it is necessary to identify the object that corresponds to the femur, this example is relatively simple, but in images more complex as the head of the femur (figure 3.10(a)) is extremely difficult.

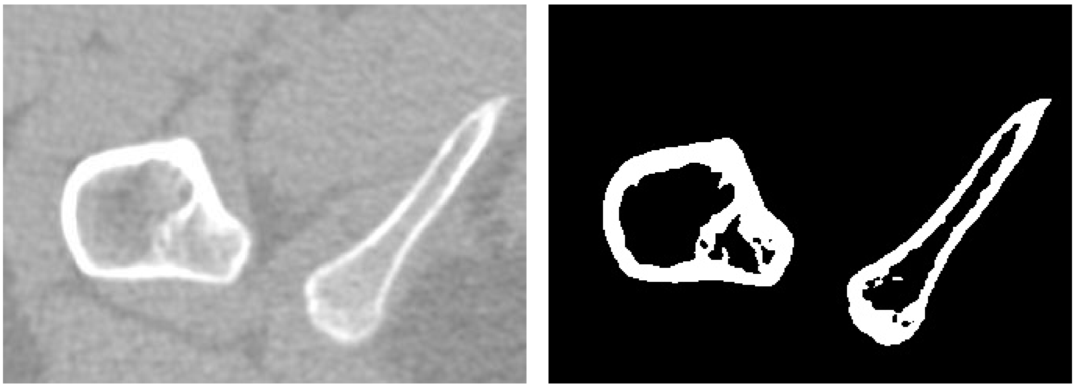

(a) CT image of the femur in the pelvic zone, after adjusting intensity.

(b) Result of thresholding image segmentation.

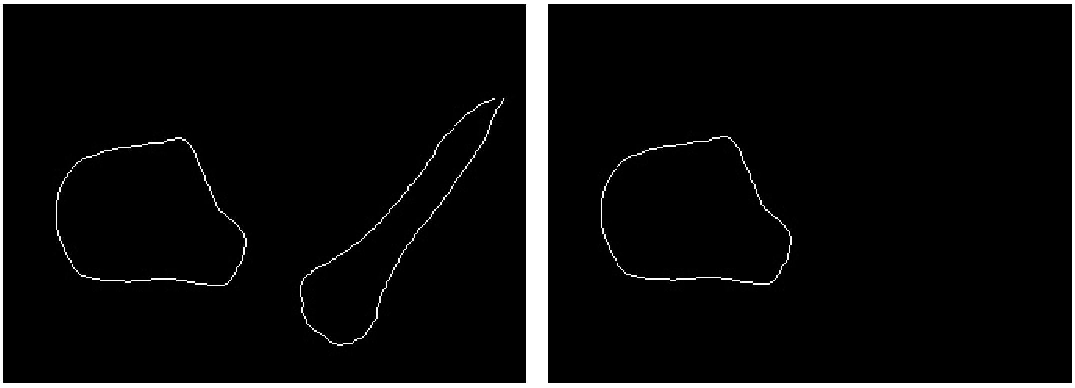

(c) External contour of segmentation.

(d) Final result.

Figure 3.9: Segmentation steps of CT images, on the head of the femur.

Applied the method proposed in section 3.1.1, with appropriate adjustments for such images, the head of the femur is identified with precision, despite various objects present in the image with similar levels of intensity. It is necessary to initialize the algorithm with a mask in the region of the head of femur and adjust the regulation term, to control the evolution of contour. Figure 3.10(b) represents the identification of target obtained by the proposed method, figure 3.10(c) the segmentation result and figure 3.10(d), the external contour used to extract the point clouds. The remainder images of the femur don't have the problem of having multiple objects with the same intensity, so the segmentation is performed by thresholding, with threshold values identified by histogram, since it accelerates the processing time.

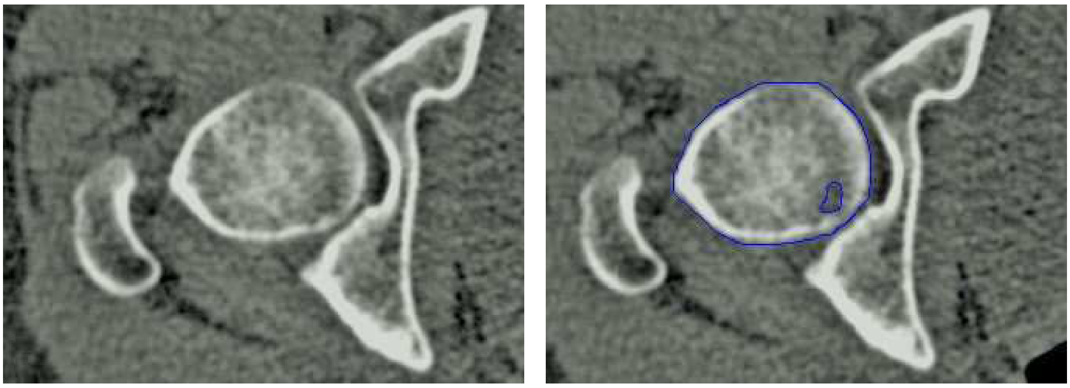

(a) CT image of the head of the femur. (b) Segmentation result.

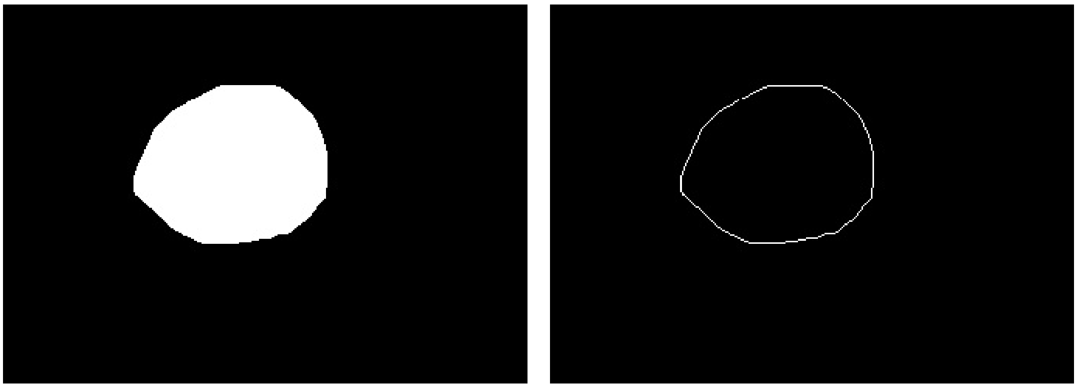

(c) Head of femur. (d) Final result.

Figure 3.10: Segmentation steps of CT images, on the head of the femur, with the proposed method.

3.2.1 Point Cloud Extraction

To extract the point cloud of CT images, it is necessary to take into account the metric units of each CT slice and the spacing between slices. According to section 2.2 the pixel size of CT images refereed to the human femur is equal to $0.3613\ [mm]$, this means that each pixel has $0.3613\ [mm]$ of dimensions in x and y. The depth is given by the spacing between slices, which we know to be $0.1\ [mm]$, however one must keep in mind that images are recorded by CT datasets, so the images do not appear followed and it is important extract the location of the DICOM file (*SliceLocation parameter*).

From the DICOM dataset, the point cloud extracted from segmented images, has a dimension quite high, with 1567171 points (figure 3.12(a)), which leads to a subsequent process of downsampling, Marion *et al.* (2012), in order to process point cloud for registration and visualization.

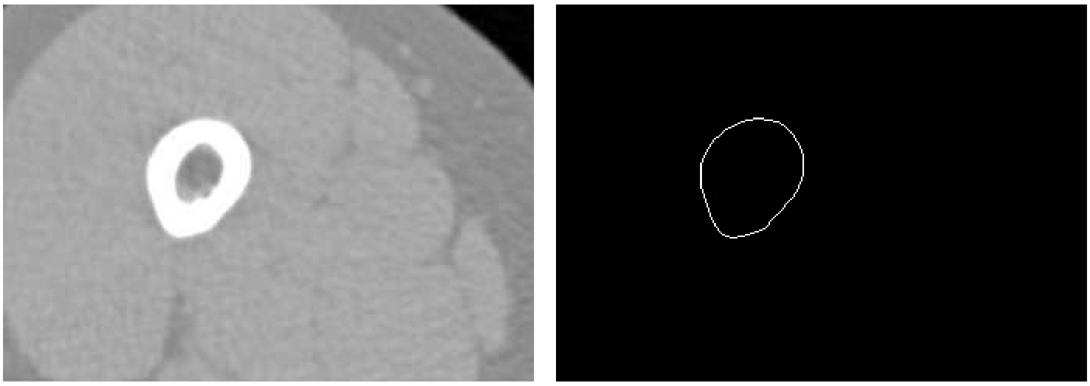

(a) CT image of the central part of the femur. (b) Segmentation Result.

Figure 3.11: Segmentation result of CT images in the central part of the bone.

With the downsampling process, the number of points are reduced to 42451 (figure 3.12(b)). The reducing of the number of points decreases the accuracy of the point clouds, but facilitates the registration process, insofar as improves the processing time. Figure 3.12 shows the point clouds obtained, before and after downsampling.

3.3 3D Reconstruction and Visualization

Visualization of 3D volume data, obtained from reconstruction of 2D medical images is a very important concept in different areas, e.g., surgical robotics. Perception of anatomical structures of the human body, without the use of evasive techniques, is an important aspect that can increase the rate of precise diagnosis. The usage of CAOS techniques by surgeons is rapidly growing. CAOS enhance the Hip Resurfacing or Hip Replacement process, since automatic systems increase surgical tasks precision and accuracy.

The surgeon, to achieve a better implant alignment, should use a precise 3D bone visualization tool. The work, presented in this section describes the techniques of volume rendering of US and CT images of femur bones, essential for navigating a robot for orthopaedic surgery. This section describes the techniques of Surface Rendering and Volume Rendering, used in this thesis.

Surface Rendering interprets the datasets by generating a set of polygons that represent the anatomical surface, and displaying a three-dimensional model representation. Polygons representing the outer surface of an object can be identified by running an isosurface detection algorithm (e.g. a Marching Cubes algorithm, Lorensen & Cline (1987)). This method show 3D relationships most effectively, but suffer from artefacts and fail to effectively display lesions hidden behind overlying bone or located beneath the bone cortex. It also does not display the

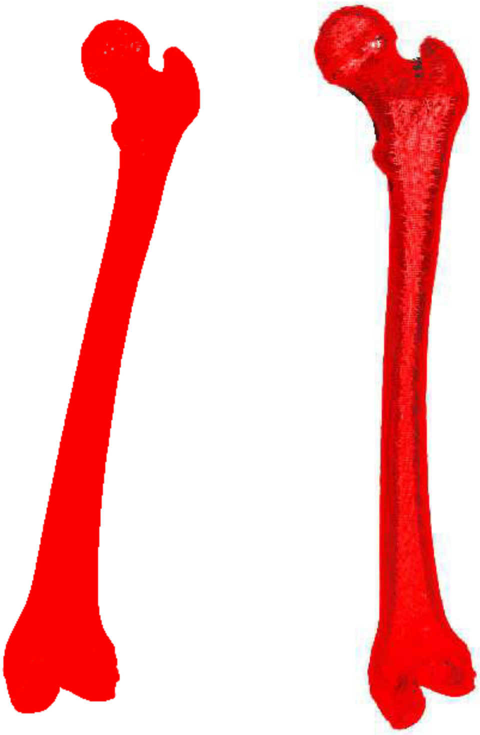

(a) Point cloud extracted from CT images.

(b) Point cloud extracted from CT images, after downsampling.

Figure 3.12: Point clouds of CT images.

most important information in the image dataset, because simplifies the data into a binary form, classifying each pixel as either bone or not bone.

Volume Rendering represents 3D objects as a collection of cube-like building blocks called voxels, or volume elements. Each voxel is a sample of the original volume, a 3D pixel on a regular 3D grid. Each voxel has associated one or more values quantifying some measured or calculated properties of the original object, such as transparency, luminosity, density, flow velocity or metabolic activity. The main advantage of this type of rendering is its ability to preserve the integrity of the original data throughout the visualization process. Using this method is possible to show sub-cortical lesions, minimally displaced fractures, and hidden areas of interest with few artefacts. Depending on the degree of surface shading and opacity, multiple overlying and internal features can be shown, and the displayed intensity is related to the amount of bone encountered along a line extending through the volume.

There are several techniques to perform volume rendering, as volume ray casting, Lee *et al.* (2010), splating, Piccand *et al.* (2008), among others. The present work is focused in the Maximum Intensity Projection (MIP) Algorithm. This method, first introduced by Wallis *et al.* (1989), is a Volume Rendering method for 3D data, which projects in the visualization plane the voxels with maximum intensity. The technique consists of projecting the highest intensity captured by the rays perpendicular to the projection of the image, i.e. the method only displays the highest intensity value seen through each pixel. This type of projection is used to highlight the important parts of the image.

3.3.1 3D Reconstruction and Visualization Experimental Results

This subsection presents the bone reconstruction results, performed with VTK and *MATLAB*, for CT and US images. The Visualization Toolkit (VTK) is an open-source, object-oriented software system for 3D computer graphics, image processing and visualization. It is provided as a *C++* library with interfaces to the interpreted languages such as *Tcl*, *Python* and *Java*. In this thesis, *Microsoft Visual Studio 2010*, with VTK, is adopted to reconstruct the 3D images using the 2D CT image sequence in DICOM format. Conventional 3D visualization tools usually have important limitations such as low efficient code execution, poor computing capacity. VTK overcomes these limitations, because has constantly evolved, has fast algorithms and computationally efficient.

3D reconstruction was performed with US and CT images of a cow femur bone and an human femur, already described in previous sections. With the reconstruction is possible to visualize the bone in $360°$, for complete visualization, in its total length and identify possible lesions, if existing. To reconstruct the volume of the bone it is necessary to load images (*vtkDICOMImageReader class*), rendering the images (*vtkRenderer class*) and finally create a volume (*vtkVolume class*). Figures 3.13 and 3.14, represents the volume reconstruction of bone, performed with the MIP algorithm for the CT images.

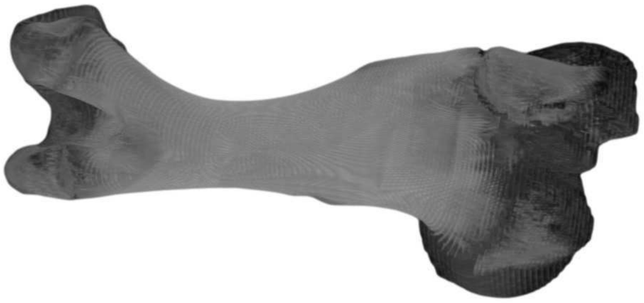

Figure 3.13: Femur Bone Reconstruction, with a high level of transparency (MIP).

The application developed allows to combine colors and opacity of the representation and thus highlight the parts that are most interesting finding in the representation. Figure 3.14 presents an example where it intends to highlight more the bone definitions, giving less importance to the interior, unlike the results of Figure 3.13, which is very transparent.

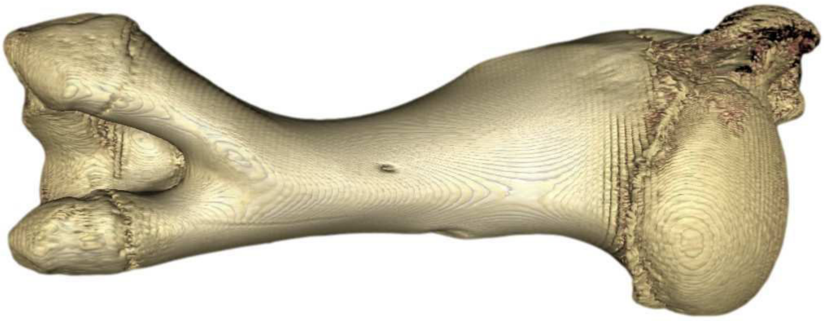

Figure 3.14: Femur Bone Reconstruction, with highlight bone definitions.

Figure 3.15 shows a section of the bone highlighting the cross section and view inside the bone. These representations have a good image quality showing a perfect bone constitution, inside and outside. It is visible the nodules of the femur in a perfect and realistic reconstruction.

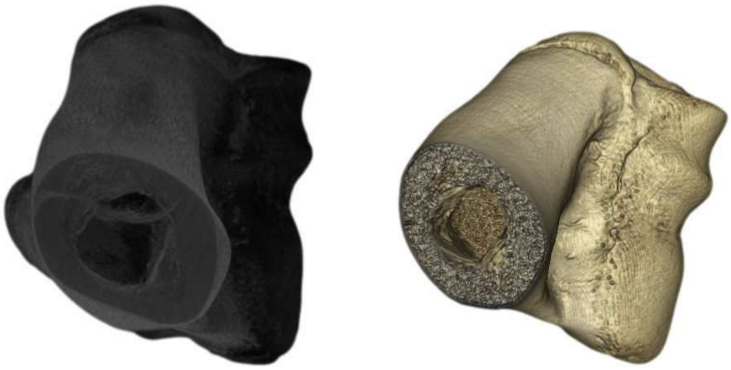

(a) Cross section Femur Bone Reconstruction.
(b) Cross section Femur Bone Reconstruction.

Figure 3.15: Cross section Femur Bone Reconstruction.

The results obtained from the *MATLAB* implementation, for the volume reconstruction with the CT images, have less quality than the results achieved with VTK and the computational cost is much higher. Figure 3.16 shows the Volume Rendering of CT images (3.16(a)) and US images (3.16(b)). As ultrasound does not penetrate the bone, in this type of image is only possible to view the upper surface of the femur.

Surface Rendering technique was only implemented in order to compare the results with Volume Rendering technique. Figure 3.17 shows the results of surface rendering obtained with CT

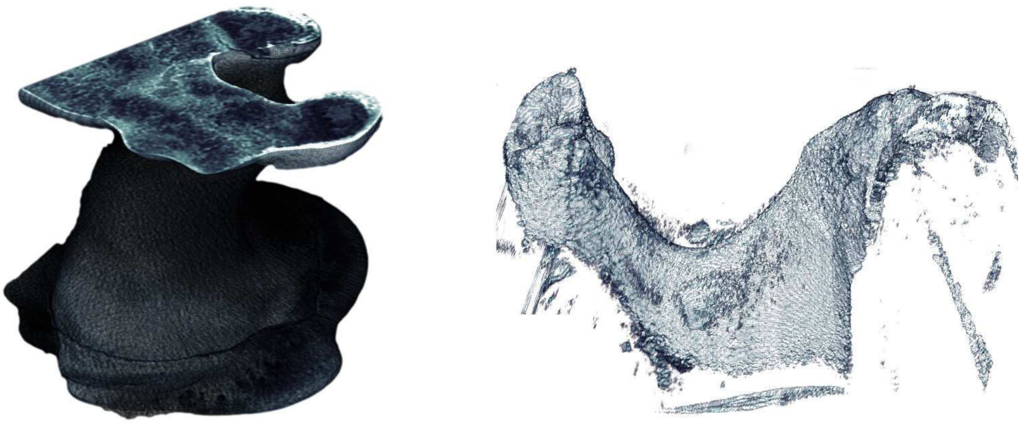

(a) volume of CT images.

(b) volume of US images

Figure 3.16: Volume Rendering performed in Matlab.

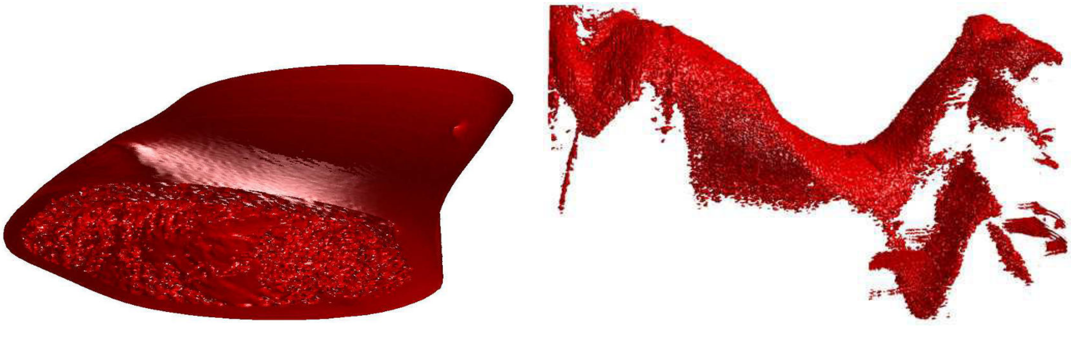

(a) Reconstruction of CT images.

(b) Reconstruction of US images

Figure 3.17: Surface Rendering performed in Matlab.

images and US images. CT image reconstruction of the full dimension of the femur, was not possible because computational cost was very high and Matlab was not enough memory to process so much data. Figure 3.18 shows two types of visualization of the volume reconstruction, with CT images of the human femur.

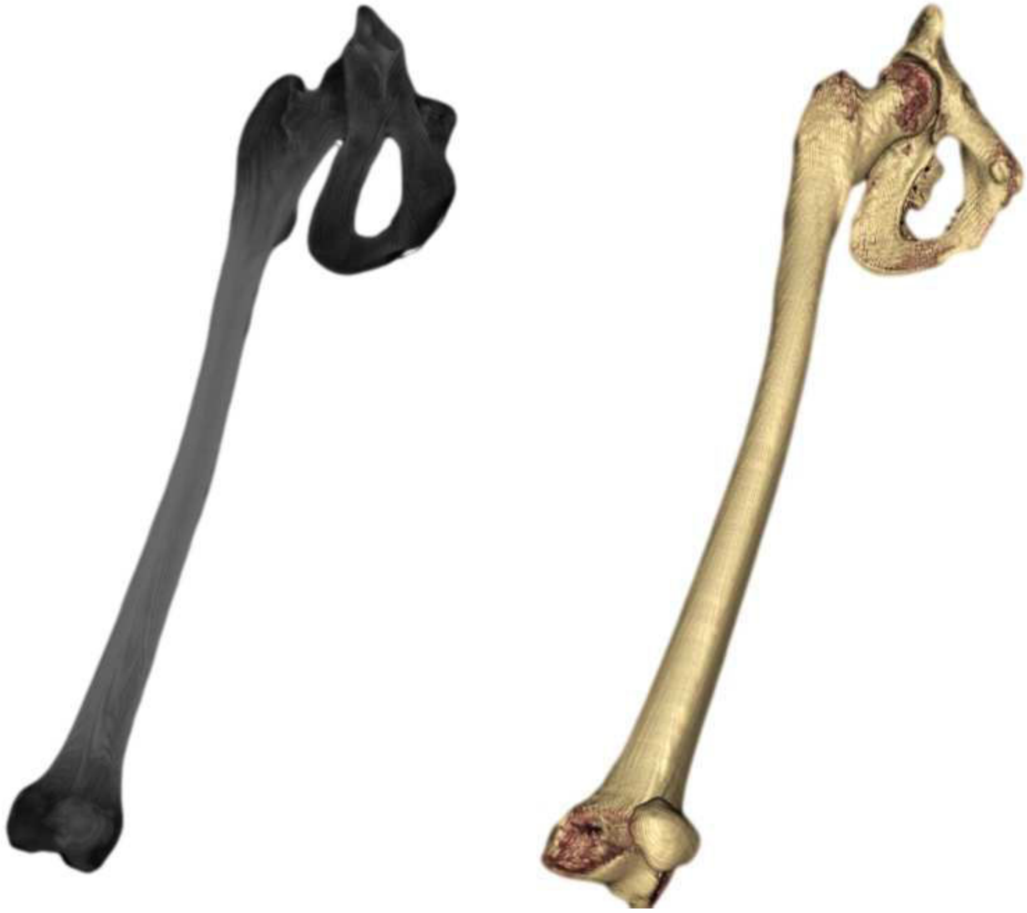

(a) Visualization of the femur with high level of transparency.

(b) Visualization of the femur with opacity.

Figure 3.18: Results of Visualization a human femur.

Chapter 4

Image Registration

This chapter describes the image registration tasks performed in order to find a relationship between the set of US images acquired in the intra-operative scenario, with the images of CT already pre-processed in the preoperative scenario. This relationship allows locating the femur into the operating room in order to contribute to the surgical navigation during hip resurfacing surgery.

4.1 Introduction

As already described, in previous chapters, this thesis aims to demonstrate that it is possible to navigate the surgical robotic system with information extracted from CT and ultrasound images. Medical images used are obtained from different sources, CT scans and ultrasound. In practice, images acquired have different coordinate systems. The process of transforming these images into a single coordinate system is called image registration. As derived from different sources, called Multimodal image registration, Maintz & Viergever (1998).

Registration of medical images allow to relate a group of images obtained in a pre-operative scenario, with images obtained in the intra-operative scenario, assisting the surgeon in surgical navigation, Dang *et al.* (2010).

Minimally invasive surgical interventions performed using Computer-Assisted Surgery (CAS), Sugano (2003) systems require reliable registration methods for pre-operatively acquired patient anatomy representations that are compatible with the minimally invasive paradigm.

In general, the image registration method can be classed into the methods based on the features (feature-based) and the intensity information (intensity-based). The registration transformation considered will depend on the application addressed and the nature of the images involved. The transformations can be categorized into affine transformations, rigid and nonrigid or elastic. Affine transformations, NOPPADOL & KE (2009), preserves the operations of vector addition and scalar multiplication, being a combination of translation, rotation, scaling, and shear components. In rigid transformations, there is no distortion of the object, the transformations are global, involves a linear rigid-body transformation, consisting of rotation and translation. Nonrigid or elastic transformations, allows local deformations of image features.

3D multi-modal point set Registration of anatomical structures, such as bone, is complex because the datasets arrive from different scans. Adequate feature extraction algorithms are essential to accurately align the two datasets. Several methods have been developed in recent years to perform the registration of bone ultrasound images, obtained in the intra-operative scenario, to the 3D bone model, obtained from CT images, Winter *et al.* (2006). The approaches presented by the research community are nowadays a active field of research, due to the need of a high precision system. In fact, the following approaches can perform US images to 3D bone model registration on several parts of the human body but still need to improve its overall accuracy. The approaches tackle the Spine, Brendel *et al.* (2002), the shoulder, Tyryshkin *et al.* (2007) and the nose, Descoteaux *et al.* (2006). The most commonly method used is the ICP, Granger *et al.* (2010), Salvi *et al.* (2006). Recently, (Myronenko & Song, 2010) have proposed a new method, that relies on a probabilistic framework to perform the registration.

In this thesis two feature-based registration methods, are used to perform the 3D point set registration, between US and CT datasets in order to compare results and draw appropriate conclusions. The first method used is the ICP method, based on an iterative approach between two rows of points in order to achieve the closest relationship between them. The second method, CPD, recently proposed, is based on the probabilistic concept to relate two datasets.

4.2 Iterative Closest Point (ICP) Method

The Iterative Closest Point (ICP) method, presented by (Besl & McKay, 1992) is the standard method used to perform registration between two set of 3D points. It transforms two sets of points to a common coordinate frame. If the exact correspondences of the two data set could be known, then the exact translation t and rotation R can be found. The main issue of the method is then to find the corresponding points between the two data sets, $Y = (y_1, ..., y_M)^T$ and $X = (x_1, ..., x_M)^T$.

The assumption in the ICP method is that the closest points between the data sets correspond to each other, and are used to compute the best transformation, rotation and translation, between them. The original method have been extended to line segment sets, implicit curves, parametric curves, triangle sets, implicit surface and parametric surfaces.

To obtain the closest point of Y to a point in X, the Euclidean distance is applied:

$$d(Y, X) = \sqrt{(X_x - Y_x)^2 + (X_y - Y_y)^2 + (X_z - Y_z)^2} \tag{18}$$

When all points of the data set Y are associated to the point in X the transformation is estimated by minimizing a mean square cost function:

$$E_{ICP} = \sum_i \|R \cdot x_i + t - y_i\|^2 \tag{19}$$

From the obtained parameters, the points in the X data set are transformed and the error between them and the ones in Y calculated. If the error is above a pre-defined threshold then the points must be re-associated and the previous steps again performed until the error is below the threshold. Figure 4.1 helps us understand the alignment procedure.

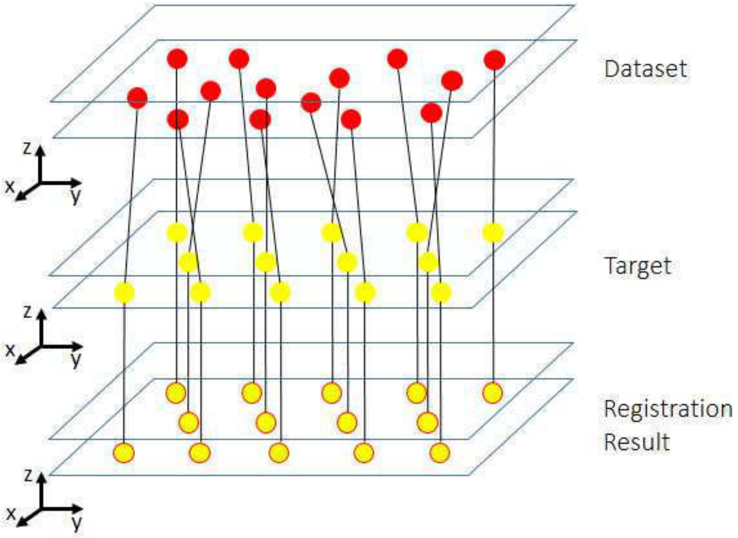

Figure 4.1: Example of alignment for local minimum.

4.3 Coherent Point Drift (CPD) Method

Coherent Point Drift is a probabilistic method for point set registration, described in Myronenko & Song (2010). Given two n-dimensional point sets, where a given point set is expressed as $Y = (y_1, ..., y_M)^T$ and should be aligned with the reference point set $X = (x_1, ..., x_N)^T$. Points in Y are considered the centroids of the Gaussian Mixture Model, and fit it to the data points X by maximizing a likelihood function. Bayes theorem is used to find the parameters Y by maximizing the posteriori probability, or minimizing the energy function:

$$E_{CPD}(Y) = -\sum_{n=1}^{N} log \sum_{m=1}^{M} e^{-\frac{1}{2}\|\frac{x_n - y_m}{\sigma}\|^2} + \frac{\lambda}{2}\phi(Y) \tag{20}$$

where E is the negative log-likelihood function, $\phi(Y)$ is a regularization term, and λ is a trade-off parameter.

4.4 Experimental Results

In this section are presented the Surface registration results obtained using the 3D point clouds, extracted, from a US and CT images, described in section 3.3. To match the two surfaces, several testes were performed, with datasets of a cow femur bone, and a human femur through affine and rigid registration of ICP and CPD algorithms.

Table 4.1: Registration Errors Results, with a cow femur bone.

	Registration Errors [mm]			
	Before	After	iter.	time
CPD Affine	51.8662	44.1493	40	17m:22s
CPD Rigid		47.4229	26	11m:40s
ICP Rigid		47.7152	27	10m:86s

In Torres *et al.* (2011b), are presented the registration results between the US and CT surfaces, of a cow femur bone, shown in figures 4.2(a), 4.2(b) and 4.2(c). Table 4.1 shows the results of RMSE, according to equation 21, and the time consumed for each simulation.

Algorithms were tested in $MATLAB$, with an Intel Core 2 Duo, 2.27 GHz computer, with 4 GB RAM. Better results, were presented by affine registration performed by the CPD method,

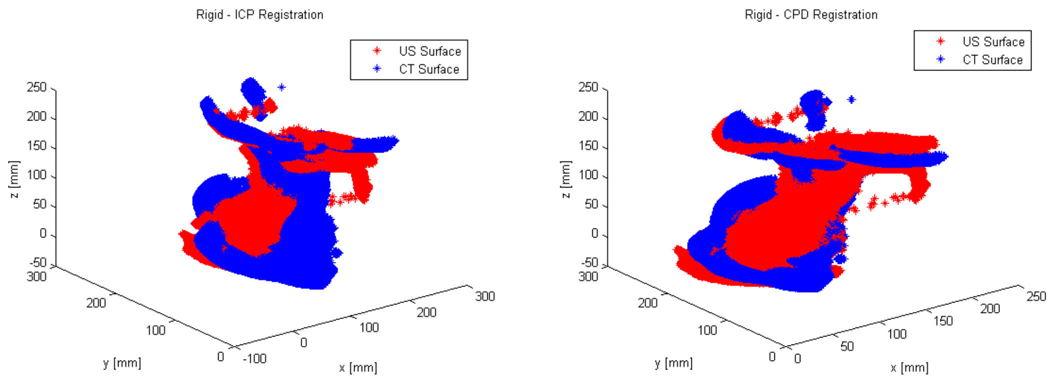

(a) ICP Rigid Registration of cow femur bone.

(b) CPD Rigid Registration of cow femur bone.

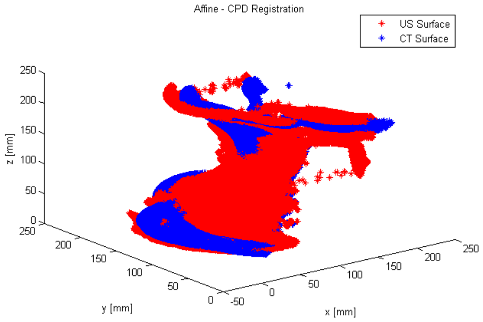

(c) CPD Affine Registration of cow femur bone.

Figure 4.2: Registration Results of cow femur bone.

although it takes longer to converge. ICP Affine method, was also implemented and tested, but failed to obtain an adequate registration, and the simulations lasted one full day, it was decided to exclude this method, because its contribution was not valid for this study.

Despite the relation between the two point clouds, the errors obtained are quite high, essentially because the two surfaces have different sizes and root mean squared error not reflect accurately the registration error.

$$RMSE = \sqrt{\frac{1}{n}\sum(\widehat{y}_i - y_i)^2} \tag{21}$$

To overcome this limitation, the registration errors was measure by the Modified Hausdorff Distance (MHD), presented in Mémoli & Sapiro (2004). Hausdorff distance is the maximum distance of a set to the nearest point in the other set. Given two finite datasets $A = \{a_1, ..., a_n\}$ and $B = \{b_1, ..., b_n\}$, the Hausdorff Distance (HD) is defined as:

$$HD(A, B) = max\, min \parallel a - b \parallel \tag{22}$$

Modified Hausdorff distance (MHD) measure, defined in equation 23, give the best performance.

$$MHD(A, B) = \frac{1}{N_a} \sum min \parallel a - b \parallel \tag{23}$$

where N_a is the number of points in A.

The registration results achieved with the point clouds extracted from the human femur are shown in figures 4.3(a) and 4.3(b), with the quantitative results presented in the table 4.2.

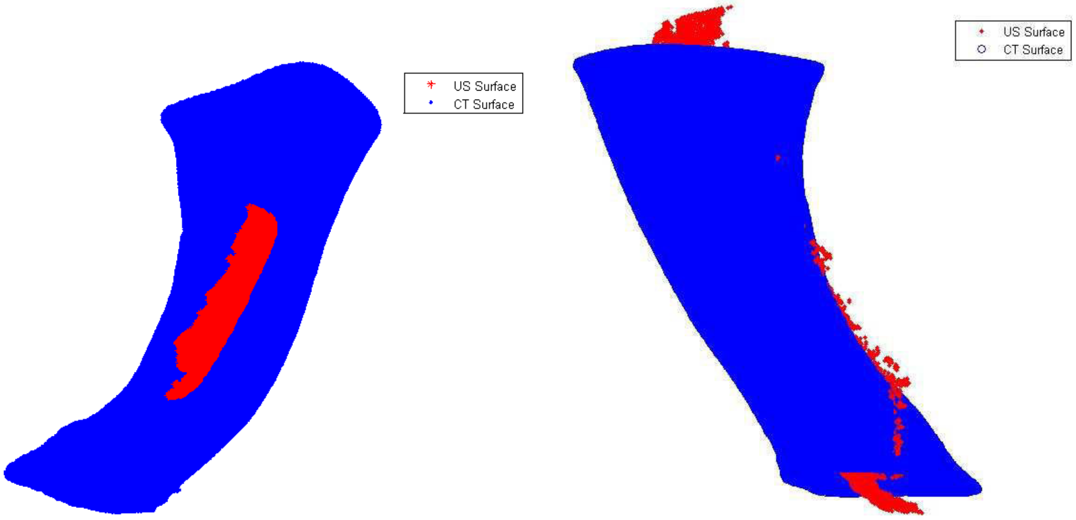

(a) ICP Rigid Registration of human bone. (b) CPD Rigid Registration of human femur.

Figure 4.3: Registration Results of human femur.

Table 4.2: Registration Errors Results of the human femur.

Method	MHD [mm] Before Registration	MHD [mm] After Registration
ICP Rigid	1433,3	74,8061
CPD Rigid		15,9435

This chapter presented the work developed to register 3D surfaces, with data from US and CT images. The well known ICP and the recent CPD methods were tested to register the points of US and CT images of a cow femur bone and a human femur. The results obtained validate the approach for the femur application. CPD algorithm presents better results although with high computational cost.

Chapter 5

Visual Control of Robotic Manipulator using Fuzzy Models

Robotic Manipulators are highly complex dynamic systems that can use a large amount of sensors to recognize its work environment. Laser, infrared or ultrasound sensors are used to measure distances. Force sensors are used to recognize contact between the robot and other objects. Cameras can be used to visualize the robot's global work environment.

Nowadays, robotic manipulators are used in factories to perform tasks in a specially designed work environment. Force and distance sensors are mainly used in these setups. Introducing cameras in this setup could, in a hopefully near future, make robot manipulators completely autonomous when performing tasks in unknown, or unable, to be precisely, modelled environments.

In the past decades, the use of computer vision and image processing methods has been constrained due to its high demanding computational costs. In the late 70's dozens of seconds were needed to extract simple object characteristics, e.g., edges. At that time, vision was used to detect the object position in the 3D space. This position was then used by the robot controller to drive the robot to it. Since the early 90's, due to the increasing capacity of computers, the vision sensor data can be used as sensor feedback to close the control loop. Nowadays the camera manufacturers can supply fast cameras that can achieve sample times up to one millisecond, i.e. comparable to distance or force sensors. This achievement, followed by the recent developments in Visual Control, opens a wide area for robotic applications.

Visual Control, also called Visual Servoing, has as its main objective the increase of flexibility and precision of the robot manipulator, when performing tasks. The vision sensor can give the robot a general overview of its working environment, which can be used as control input. Visual

Control aims to cancel the robot's manipulator position error, using as feedback, in the control loop, the data provided by the vision sensor.

The vision data can be directly or indirectly used in the control loop. The large majority of Visual Servoing approaches use an inner robot controller, with joint variables feedback, to stabilize the robot around the control action arriving from the outer visual control loop. The vision data, i.e., visual features, that characterize the object to be manipulated can be used directly in the control loop, e.g., the 2D pixels of the object or the object image moments. Visual features can also be used indirectly, e.g., the 3D data points of the object that describes its pose. 2D and 3D visual features can be combined to achieve the called hybrid features. The application of the above presented visual features derives different control laws, which are called image-based Visual Servoing, position-based Visual Servoing and hybrid Visual Servoing. In these approaches, the model of the visual motor interaction is already known. More recently the visual motor interaction has been estimated analytically or by learning, opening a new area for Visual Control of uncalibrated robotics systems. Visual Servoing is also evolving to new types of images, e.g., medical images. In this applications, surgical robotics, Ayadi *et al.* (2008); Ginhoux *et al.* (2005); Krupa *et al.* (2003, 2004); Li *et al.* (2012); Mebarki *et al.* (2010), the visual loop is used to position ultrasound probes, to track organs, and to assist surgeons performing surgical tasks.

5.1 Introduction

Visual Servo Control, *visual servoing*, Hill & Park (1979); Hutchinson *et al.* (1996), defines closed loop robot control using cameras to extract visual information from the robot's work environment. From the desired robot position and the visual information obtained from the camera, the visual servo control law gives the desired velocities that move the robot. The use of vision systems in robotics aims to increase flexibility and precision of robots. One of the first works that used vision to control a robot was presented by Shirai and Inoue Shirai & Inoue (1973), almost 40 years ago. The role of computer vision is to provide the robot with information about its work environment, to be used in the control loop.

Information from the robot's work environment can be used in control by two ways. The first approach called *Open-Loop-Robot-Control*, separates the vision part from the control part. The start and final positions of the robot are obtained using computer vision (pose estimation algorithms) and the robot's movement is controlled only on the joint or cartesian space. This approach needs camera calibration and the model of the object to manipulate. The second approach called *visual servoing*, uses directly or indirectly visual information to close the robot control loop. In this approach it is often used an inner controller, with joint feedback, to stabilize the robot around the control action that arrives from the outer vision control loop. The large majority of visual servoing applications are based on this approach.

Direct visual information uses pixel information, e.g., 2D points describing features of interest on the object to manipulate. Indirect visual information implies extraction of relevant object characteristics from 2D coordinates in the image space, e.g., the 3D pose of the object related to the camera frame.

Typical visual servoing applications can be classified as i) *positioning* the robot end-effector to an object; ii) *tracking* an object, e.g., keeping a constant distance from the object to the robot.

The object to manipulate is an important part of the visual control loop and its characterization is of special importance to formulate the control problem. This visual information can be obtained from one or more cameras looking at the robot and the object *eye-to-hand*, or being placed in the end-effector *eye-in-hand*. Object characteristics can be obtained: i) using 2D data expressed directly in pixel coordinates from the image space, ii) using 3D data to obtain the object pose, iii) fusing 2D and 3D data. To use these object characteristics, visual features, in the control loop, it is mandatory to obtain a relation between the feature space and the world, or camera frames. This relation (interaction model) has been over the years, an exciting field of research, and it is the base of visual servoing approaches. The first and second approaches are called *image-based visual servoing* and *position-based visual servoing*, respectively, Hutchinson *et al.* (1996). The third approach is called *hybrid visual servoing*, Hashimoto (2003), being the first reported work presented in, Malis *et al.* (1999).

Interaction models between the visual features of the object and camera coordinates frames can be grouped in two. The models known a priori, using analytical relations are in the first group. The models estimated numerically are in the second group. These models are used to generate movement commands to the robot and are called, amongst other terms, Hashimoto (2003), by image Jacobian. The other important relation is between the visual features and the robot joint coordinates. To build this model, the robot Jacobian and the relation between the camera and end-effector frames must be known.

In this chapter, the robot-camera model estimation by learning is addressed, using fuzzy techniques, to obtain a controller capable of controlling the robotic system. An inverse fuzzy model is used to derive the inverse robot-camera model, in order to compute the joints and end-effector velocities in a straightforward manner. The inverse fuzzy model is applied directly as a real-time controller.

From the modeling techniques based on soft computing, fuzzy modeling is one of the most appealing. In visual servoing, fuzzy logic has been used to learn the robot-camera model, Suh & Kim (1994, 2000). As the robotic manipulator together with the visual system is a nonlinear system, which is only partly known, it is advantageous to use fuzzy modeling as a way to derive a model (or an inverse model, as in this case) based only on measurements. Various techniques can be applied to derive such models, fuzzy clustering, neural learning methods or orthogonal least squares (see e.g. Guillaume (2001) for an overview). Fuzzy clustering is most often used to derive fuzzy models based on the data obtained from measurements of dynamic systems. This approach is used in this chapter and it is presented in detail in, Gonçalves *et al.* (2008). The next subsections present the fuzzy modeling approach and how the uncalibrated fuzzy model was obtained.

5.2 Fuzzy Modeling

5.2.1 Off-Line Fuzzy Modeling

Fuzzy modeling often follows the approach of encoding expert knowledge expressed in a verbal form in a collection of if–then rules, creating the model structure. Parameters in this structure can be adapted using input-output data. When no prior knowledge about the system is available, a fuzzy model can be constructed entirely on the basis of systems' measurements. In the following, we consider data-driven modeling based on fuzzy clustering, which is described in, Sousa & Kaymak (2002). This approach proved to be better than other well-known methods, such as Adaptive Neural Fuzzy Inference Systems (ANFIS), which was presented in, Jang (1993).

Assume that data from an unknown Multiple-input and Single-output (MISO) system $y = F(\mathbf{x})$ is observed. The aim is to use this data to construct a deterministic function $y = f(\mathbf{x})$ that can approximate $F(\mathbf{x})$. The function f is represented as a collection of fuzzy if–then rules. Depending on the form of the propositions and on the structure of the rule base, different types of rule-based fuzzy models can be distinguished.

For the robot under control, the direct robot-camera model states that the image features will move between consecutive time steps k and $k+1$, in the image space. This variation of the image features is defined as $\delta\mathbf{s}(k+1) = \mathbf{s}(k+1) - \mathbf{s}(k)$. Given a predefined robot velocity $\dot{\mathbf{q}}(k)$, and knowing its actual position $\mathbf{P}(k)$ in the world coordinate frame at the current time step k, the image features will move from $\mathbf{s}(k)$ to $\mathbf{s}(k+1)$.

In this chapter, rule-based MISO models of first order Takagi-Sugeno, Takagi & Sugeno (1985) type are considered. This type of models is described next, followed by a brief description of the identification procedure using fuzzy clustering.

5.2.2 Takagi–Sugeno fuzzy model

First order, MISO, Takagi-Sugeno rule-based models, are considered in this chapter. The models have n inputs and one single output. For systems with more outputs, several MISO models are needed to model the overall system, e.g., two MISO models are needed to model systems of two outputs.

The fuzzy model is divided in rules. Each rule is applied to a sub-domain of the input variables. This sub-domain is called a cluster and is obtained using clustering approaches, Gustafson & Kessel (1979). In each cluster there is a rule that describes the input-output relation. In conclusion, the rules of a Takagi-Sugeno fuzzy model describe local input-output relations, typically in a linear form, where the output y_i of each rule is a linear combination of the inputs $\mathbf{x}$:

$$\begin{aligned} &R_i : \textbf{If } x_1 \text{ is } A_{i1}\textbf{and } \ldots \textbf{and } x_n \text{ is } A_{in} \\ &\textbf{then } y_i = \mathbf{a}_i\mathbf{x} + b_i\,, \quad i = 1, 2, \ldots, K. \end{aligned} \tag{24}$$

Here R_i is the i^{th} rule, $\mathbf{x} = [x_1, \ldots, x_n]^T$ is the input (antecedents) variables. $A_{i1}, \ldots, A_{in}$ are fuzzy sets defined in the antecedent space, that must be estimated. y_i is the rule output variable. $\mathbf{a}_i$ and b_i are the consequent parameters of the linear combination for each rule, that must be estimated. K denotes the number of rules in the rule base. For each cluster i, the correspondent rule R_i gives an output y_i, that must be combined to obtain the only output of the MISO system. The aggregated output of the model, $\hat{y}$, is calculated by taking the weighted average of the rule consequents of each rule:

$$\hat{y} = \frac{\sum_{i=1}^{K} \beta_i y_i}{\sum_{i=1}^{K} \beta_i}\,, \tag{25}$$

where β_i is the degree of activation of the i^{th} rule, stating for a given input what rules are the most active.

$$\beta_i = \Pi_{j=1}^{n} \mu_{A_{ij}}(x_j), \quad i = 1, 2, \ldots, K, \tag{26}$$

and $\mu_{A_{ij}}(x_j)$: $\mathbb{R} \rightarrow [0, 1]$ is the membership function of the fuzzy set A_{ij} in the antecedent of R_i.

5.2.3 Fuzzy Model Parameters Identification by fuzzy clustering

To identify the first order Takagi-Sugeno model defined in (24), i.e., the antecedent and consequent parameters, the regression matrix $\mathbf{X}$ and an output vector $\mathbf{y}$ are constructed from the available input-output data:

$$\mathbf{X}^T = [\mathbf{x}_1, \ldots, \mathbf{x}_N], \quad \mathbf{y}^T = [y_1, \ldots, y_N]. \tag{27}$$

Here $N \gg n$, is the number of samples used for identification, taken at each time step. In this chapter, N is the number of time samples needed by the robot to perform a predefined trajectory. The objective of identification is to construct the unknown nonlinear function $\mathbf{y} = f(\mathbf{X})$ from the data, where f is the first order Takagi-Sugeno model in (24).

The number of rules K and the antecedent fuzzy sets A_{ij} are determined by means of fuzzy clustering in the product space of the inputs and the output, $[x_1 \times \ldots \times x_n \times y]$. Hence, the data set Φ to be clustered is composed from $\mathbf{X}$ and $\mathbf{y}$:

$$\Phi^T = [\mathbf{X}, \, \mathbf{y}] \, . \tag{28}$$

Given Φ, where the N input-output data samples are stored, and an estimated number of clusters K, the Gustafson-Kessel clustering algorithm, Gustafson & Kessel (1979), is applied to compute the fuzzy partition matrix $\mathbf{U} = [\mu_{ik}]_{K\times N}$, stating the degree of membership of each sample data, $k = 1...N$, to each cluster, $i = 1...K$.

Clustering provides a description of the system in terms of its local characteristic behavior in regions of the input-output data, Φ, where each cluster defines a rule. Unlike the popular fuzzy c-means algorithm, Bezdek (1981), the Gustafson-Kessel algorithm applies an adaptive distance measure suited for highly non-linear systems like robotic manipulators. As such, it can find hyper-ellipsoid regions in the input-output data, Φ, that can be efficiently approximated by hyperplanes described by the first order Takagi-Sugeno fuzzy rules, i.e. with dimension $n+1$ (n inputs and one output).

The fuzzy sets in the antecedent of the rules are obtained from the partition matrix $\mathbf{U}$, whose ik^{th} element $\mu_{ik} \in [0,1]$ is the membership degree of the data object $\mathbf{z}_k = [{\mathbf{x}_k}^T y_k]^T$ to the cluster i. To be used in the first order Takagi-Sugeno model defined in (24), one-dimensional fuzzy sets A_{ij} must be obtained from the multidimensional fuzzy sets defined point-wise in the i^{th} row of the partition matrix by projections onto the space of each input variable $x_j, j = 1\ldots n$:

$$\mu_{A_{ij}}(x_{jk}) = \text{proj}_j(\mu_{ik}), \tag{29}$$

where proj is the point-wise projection operator, Kruse *et al.* (1994). The point-wise defined fuzzy sets A_{ij} are approximated by suitable parametric functions, like gaussian membership functions, Sousa & Kaymak (2002), in order to compute $\mu_{A_{ij}}(x_j)$ for any value of x_j. At this point the antecedent parameters for each rule, A_{ij}, of the first order Takagi-Sugeno model have been estimated.

The consequent parameters for each rule are obtained as a weighted ordinary least-square estimate. In the following, are presented the steps to formulate the problem, following, Sousa & Kaymak (2002).

The consequents for each rule are placed in the following vectorial form, $\theta_i^T = \left[\mathbf{a}_i^T; b_i\right]$. The input-output data is extended and defined by $\mathbf{X}_e = [\mathbf{X}; \mathbf{1}]$. A diagonal matrix of weights in $\mathbb{R}^{N \times N}$, must be defined $\mathbf{W}_i$, having the degree of activation $\beta_i(\mathbf{x}_k)$, as its k^{th} diagonal element.

Assuming that the columns of $\mathbf{X}_e$ are linearly independent and $\beta_i(\mathbf{x}_k) > 0$ for $1 \leq k \leq N$, the weighted least-squares solution of $\mathbf{y} = \mathbf{X}_e\theta + \epsilon$, where ϵ is a residue, becomes:

$$\theta_i = \left[\mathbf{X}_e^T \mathbf{W}_i \mathbf{X}_e\right]^{-1} \mathbf{X}_e^T \mathbf{W}_i \mathbf{y}\,. \tag{30}$$

At this point the consequent parameters for each rule, $\mathbf{a}_i$ and b_i, of the first order Takagi-Sugeno model have been estimated.

5.2.4 On-Line Fuzzy Modeling

The model obtained from the techniques presented in the previous section is assumed to be fixed, since it is learned in off-line mode. Recently attention is focused in on-line learning, Angelov & Filev (2004), where in a first phase, input-output data is partitioned using unsupervised clustering methods and in a second phase, parameter identification is performed using a supervised learning method.

In On-Line Fuzzy Modeling and according to, Angelov & Filev (2004), also rule-based models of the TS type, are considered. Typically in the affine form described in (24), where the input-output data is acquired continuously. The new data, arriving at some time instant, can bring new information from the system, which could indicate a change in its dynamics. This information may change an existing rule, by changing the spread of the membership functions, or even introduce a new one. To achieve this, the algorithm must be able to judge the informative potential and the importance of the new data.

In the following are briefly presented the several steps of the algorithm used for on-line fuzzy modeling, proposed in, Angelov & Filev (2004), evolving fuzzy systems. The first step is based on the subtractive clustering algorithm, Chiu (1994), where the input-output data is partitioned. The procedure used must be initialized, i.e. the focal point of the first cluster is equal to the first data point and its potential is equal to one. Starting from the first data point, the potential of the next data point is calculated recursively using a Cauchy type function of first order:

$$P_k(z_k) = \frac{1}{1 + \frac{1}{k-1}\sum_{i=1}^{k-1}\sum_{j=1}^{n+1}(d_{ik}^j)^2}, \quad k = 2, 3, ... \tag{31}$$

where $P_k(z_k)$ denotes the potential of the data point z_k calculated at time k; $d_{ik}^j = z_i^j - z_k^j$, denotes projection of the distance between two data points (z_i^j and z_k^j) on the axis z^j.

When a new data point arrives it also influences the potential of the already defined center of the K clusters $(z_i^*, i = 1, 2, ..., K)$. A recursive formula for the update of the cluster centers potential is defined in, Angelov & Filev (2004):

$$P_k(z_i^*) = \frac{(k-1)P_{(k-1)}(z_i^*)}{k - 2 + P_{(k-1)}(z_i^*) + P_{(k-1)}(z_i^*) + \sum_{j=1}^{n+1}(d_{ik}^j)^2},$$

where $P_k(z_i^*)$ is the potential at time k of the cluster center, related to the rule i.

The next step of the algorithm is to compare the potential of the actual data point to the potentials of the existing cluster centers.

If the potential of a new data point is higher than the potential of the existing cluster centers, then the new data point is accepted as a new cluster center and a new rule is formed. If in addition to the previous condition the new data point is close to an old cluster center, the old cluster center is replaced. The decision to create or remove rules was based on the following principles:

1)The sample has a high potential is legible to be a focal point of a fuzzy rule:

$$P_k(z_k) > \max(P_k(z_i^*)) \tag{32}$$

2)A sample that is over an area of spatial data are is not covered by other rules, is also eligible to form a rule:

$$P_k(z_k) < \min(P_k(z_i^*)) \tag{33}$$

3)To avoid overlap and redundancy of information in creating new rules, the following condition is also checked:

$$\exists i, i = [1, R]; \mu_{ij}(x(k)) > e^{-1}; \forall j; j = [1, n] \tag{34}$$

R denotes the number of fuzzy rules up to the moment k. The membership function are gaussian, with the form:

$$\mu_{ij} = e^{-r\|x_j - x_{ij}^*\|^2}, \tag{35}$$

The consequents of the fuzzy rules are obtained using the global parameter estimation procedure based on the weighted recursive least squares, presented in, Angelov & Filev (2004).

5.2.5 Uncalibrated Fuzzy Visual Servoing

To obtain an accurate Jacobian, $\mathbf{J}$, a perfect modelling of the camera, the chosen image features, the position of the camera related to the world, and the depth of the target related to the camera frame must be accurately determined. Even when a perfect model of the Jacobian is available, it can contain singularities, which hampers the application of a control law. Remind that the Jacobian must be inverted to send the joint velocities to the robot. When the Jacobian is singular, the control cannot be correctly performed.

To overcome the difficulties regarding the Jacobian, a new type of differential relationship between the features and camera velocities was proposed in, Suh & Kim (1994). This approach states that the current joint variation, $\delta\mathbf{q}(k)$, depends on the image features variation that the robot must perform at the next time step, $\delta\mathbf{s}(k+1)$, and the current position of the robot manipulator, $\mathbf{q}(k)$:

$$\delta\mathbf{q}(k) = \mathbf{F}_k^{-1}(\delta\mathbf{s}(k+1), \mathbf{q}(k)). \tag{36}$$

In visual servoing, the goal is to obtain a joint velocity, i.e., the joint variation $\delta\mathbf{q}(k)$, capable of driving the robot according to a desired feature position, $\mathbf{s}(k+1)$, with an also desired feature variation, $\delta\mathbf{s}(k+1)$, from any position in the joint spaces. This goal can be accomplished by modelling the inverse function $\mathbf{F}_k^{-1}$, using inverse fuzzy modelling as proposed in this chapter and presented in Section 5.2.1. This new approach to visual servoing allows to overcome the problems stated previously regarding the Jacobian and the calibration of the robot-camera model.

5.3 Experimental Setup

In this section of the chapter are shown the results of the presented fuzzy modeling approach, *uncalibrated visual servoing* applied to position-based visual servo control.

To validate the proposed approach, a five-degree of freedom EurobTec IR52C Robotic Manipulator was used. The visual features were obtained from the images using a stereo vision system, with two *U-Eye* cameras, in eye-to-hand configuration, i.e., looking the robotic manipulator end-effector.

The experimental setup is presented in figure 5.1. At the IR52C robot end-effector it is attached an object with colored LEDs, depicted in figure 5.2, that is seen by the stereo vision system. For each of the three LEDs, its 3D coordinates, ${}^{c}\mathbf{t}_o$, are obtained. Note that, during the servoing, the LEDs are all in the same plane and therefore its rotation relative to the stereo vision frame (located in the left camera), ${}^{c}\mathbf{R}_o$, is the same. The visual processing is performed in the PC2, that acquires and process, Morgado *et al.* (2009), the images from both cameras and sends the 3D visual features to the network, using User Datagram Protocol (UDP) protocol, at each time step.

In PC1 is implemented the visual servoing control law, that receives the UDP packets coming from the PC2. Computer PC2, as in, Morgado *et al.* (2009), acquires images from cameras, performs color segmentation, and extracts the LEDs 3D coordinates,${}^{c}\mathbf{t}_o$, in real-time, corresponding to the 3D position of the LED. Since three LEDs are used in this setup, nine features are obtained and therefore ${}^{c}\mathbf{t}_o$ is a (9×1) vector. Note that, as stated before, the rotation, ${}^{c}\mathbf{R}_o$, is the same for all three LEDs. In the experiments presented in the following sections, the rotation, ${}^{c}\mathbf{R}_o$, was kept constant and therefore was the same for all the robot trajectories performed. For these reasons the (9×1), ${}^{c}\mathbf{t}_o$, is the feature vector, $\mathbf{s}$, sent to the network.

5.3.1 Fuzzy Modeling Results

To obtain the first order Takagi-Sugeno model defined in (24), the regression matrix (27) must be obtained from the input-output data of the robot. In section 5.2.5 was defined that the outputs of the model are the robot joint variations $\delta\mathbf{q}(k)$. These joint variations should be capable of driving the robot according to a desired feature position, $\mathbf{s}(k+1)$. Since the robot has five joints, five MISO models must be estimated, according to section 5.2.3.

To obtain the data for model identification, the robot was moved in its 3D workspace, within the field of view of the cameras, making a 3D spiral with a center point, depicted in figure 5.3. The variables needed for identification, $\delta\mathbf{q}(k)$ and $\delta\mathbf{s}(k+1)$, were stored during the 3D spiral path, i.e., the off-line training task. This procedure allows to cover a wide range of values for $\delta\mathbf{q}(k)$ and $\delta\mathbf{s}(k+1)$:

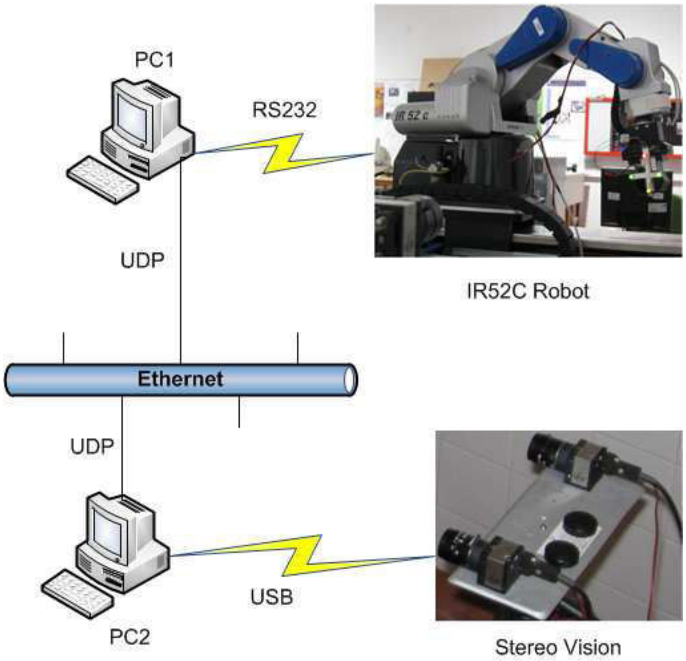
PC1
RS232
UDP
IR52C Robot
Ethernet
UDP
USB
PC2
Stereo Vision

Figure 5.1: The eye-to-hand experimental setup.

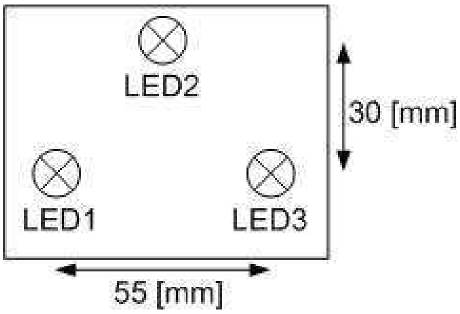
LED2
30 [mm]
LED1
LED3
55 [mm]

Figure 5.2: Configuration of the markers placed on the end-effector.

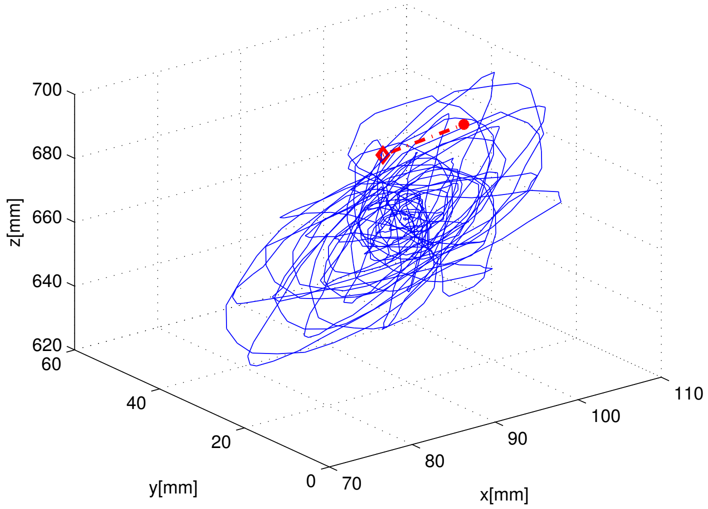

Figure 5.3: 3D Spiral path used to collect the data for the fuzzy model identification, solid thin line. Task linear trajectory used to test the visual servo control law, dash-dotted thick line.

$$\delta\mathbf{s}(k+1) = \mathbf{s}^{*} - \mathbf{s}(k+1) \tag{37}$$

$$\delta\mathbf{q}(k) = \frac{\mathbf{q}^{*} - \mathbf{q}(k)}{\Delta t} \tag{38}$$

where Δt is the visual sample time (0.1 seconds) and in the training phase:

$\mathbf{s}^{*} = [92.0\,,\, 25.0\,,\, 667.5\,,\, 66.5\,,\, 55.0\,,\, 669.0\,,\, 115.0\,,\, 57.5\,,\, 689.0](mm)$ are the 3D coordinates of the LEDs, at the center of the 3D spiral;

$\mathbf{q}^{*} = [-18.3545\,,\, -72.2546\,,\, -51.2007\,,\, -53.5447\,,\, -169.4038](^{\circ})$ are the robot manipulator joint values, at the center of the 3D spiral.

In figures 5.4, 5.5 and 5.6 are depicted, over time, the model inputs, $\delta\mathbf{s}(k+1)$, and the model outputs $\delta\mathbf{q}(k)$, respectively.

To estimate the model accuracy two descriptors are used: VAF (Variance Accounted For), defined in (39), and MSE (Mean Squared Error), defined in (40). A perfect match occurs, when VAF is 100% and MSE is 0.

$$VAF = 1 - \frac{var(\delta\mathbf{q} - \widehat{\delta\mathbf{q}})}{var(\delta\mathbf{q})} \times 100\% \tag{39}$$

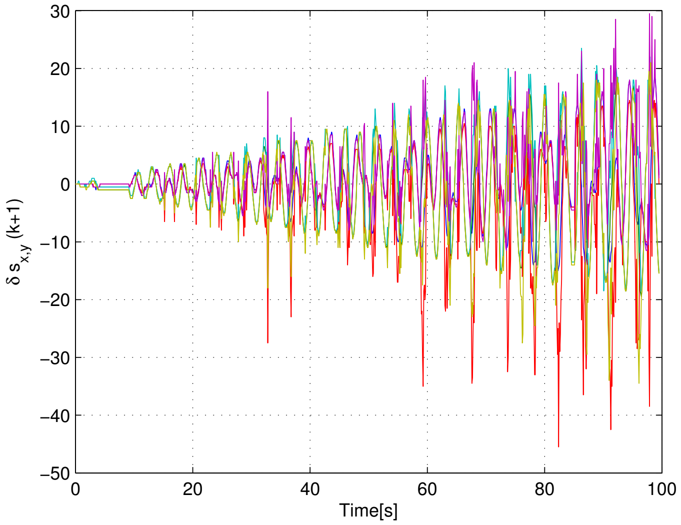

Figure 5.4: The input data for model identification, $\delta\mathbf{s}_{xy}(k+1)$, i.e., in the x and y directions.

where $\widehat{\delta\mathbf{q}}$ is the output of the estimated fuzzy model, and $var(...)$ is the variance of a vector.

$$MSE = \frac{1}{n}\sum(\widehat{\delta\mathbf{q}} - \delta\mathbf{q})^2 \tag{40}$$

where n is the size of the vectors. The values for VAF and MSE must be obtained for each robot joint using all the n samples of data collected for each joint, since five MISO fuzzy models are estimated as stated previously.

In Table 5.1 are presented the values of VAF and MSE for the off-line fuzzy modeling for each one of the five robot joints, i.e., one MISO model for each joint, using real data from the robot and vision systems. With only three rules, excellent values of VAF and MSE were obtained, meaning that is possible to obtain a good model for estimating the joint velocities, suitable to be used as a model based inverse controller. Figure 5.6, shows how close the output of the model is to the training data. In more detail, figure 5.7 depicts the result for joint 4, the worst VAF presented in table 5.1.

In Off-Line Fuzzy Modeling the number of clusters (rules) must be defined a priori in order to obtain a model. In On-Line Fuzzy Modeling, evolutionary algorithms are used that after initialized, will estimate the number of rules required in accordance with the potential associated with each data. The results from On-Line Fuzzy Modeling are presented in table 5.2. The variable Ω is the initialization parameter of the algorithm, that varies with the type of data. The results presented in table 5.2, show very good results with the exception of the last joint, but as the expense of a high number of rules, which will hopefully be minimized in future works to allow adequate control

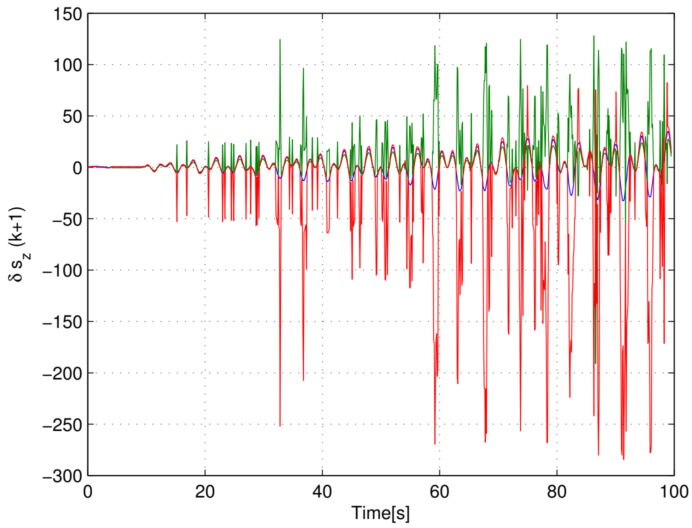

Figure 5.5: The input data for model identification, $\delta \mathbf{s}_z(k+1)$, i.e., in the z direction.

Table 5.1: Results of the off-line fuzzy model, obtained for each joint.

	Rules	VAF	MSE $[(^\circ/s)^2]$
Joint 1	3	98,2%	0,23
Joint 2	3	97,3%	0,93
Joint 3	3	94,4%	2,81
Joint 4	3	93,2%	1,21
Joint 5	3	98,2%	0,23

Table 5.2: Results of the on-line fuzzy model, obtained for each joint.

	Ω	VAF	MSE	Rules
Joint 1	400	97,9%	0,04	82
Joint 2	215	94,1%	0,37	74
Joint 3	250	95,6%	0,36	75
Joint 4	250	93,1%	0,20	66
Joint 5	342	64,3%	1,18	82

of the robot.

5.3.2 Control Results

This section presents the obtained control results, using the Off-Line fuzzy model based control, defined in figure 5.8. These results, that validate the proposed approach, were obtained from the real robot, when performing the Uncalibrated Visual Servoing using the fuzzy model previously presented.

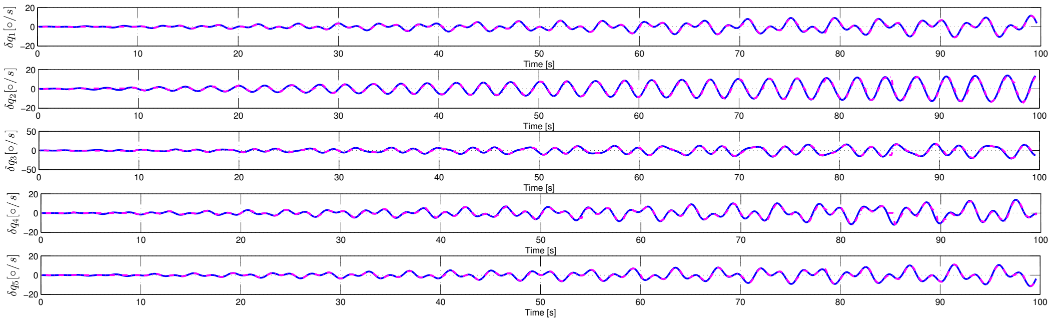

Figure 5.6: The output data, $\delta \mathbf{q}(k)$. For model identification, solid-line, and the estimated fuzzy model output, dash-dotted line.

To validate the estimated fuzzy models for controlling the robot manipulator, several positions were set within the robot workspace seen by the stereo vision system. Positioning tasks were given to the robot manipulator to fulfil. The operator gives, to the robot, the desired 3D coordinates of the object, either by a-priori knowledge or by moving the robot using a classical Cartesian control law. In this work the second approach was used.

The experiment was conducted following the general procedure:

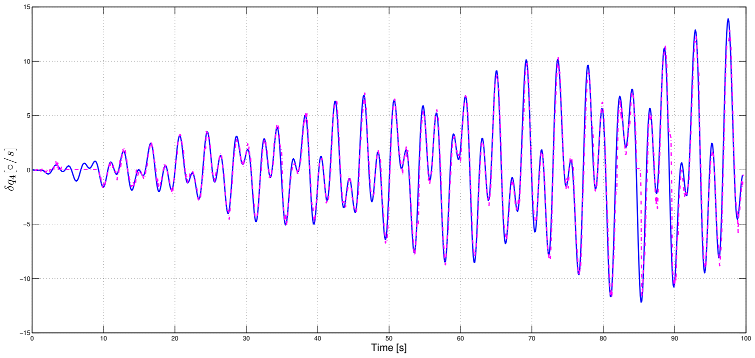

Figure 5.7: The output data, $\delta q_4(k)$. For model identification, solid-line, and the estimated fuzzy model output, dash-dotted line.

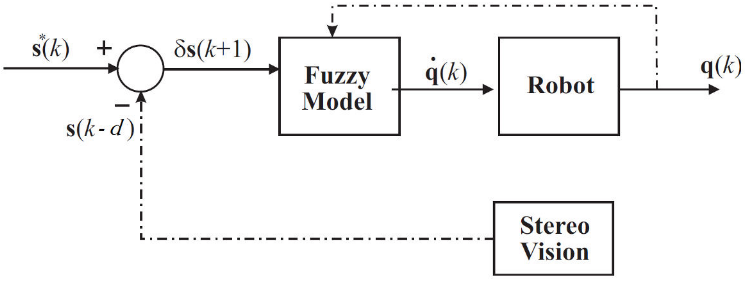

Figure 5.8: Uncalibrated Visual Servo Control Loop.

1. Move the robot to the desired position, using a classical Cartesian control law, where the stereo vision system can see the object, i.e., the three LED system.
2. Extract the desired feature vector s^* of the object, i.e., the 3D coordinates of the three LEDs.
3. Move the robot to the initial position, using a classical Cartesian control law, where the stereo vision can extract the initial feature vector of the object, s_i.
4. Start the Fuzzy Uncalibrated Visual Servoing to reach s^*.

Although in general the target position, s^*, to be tracked may varies over the time, in this experiment it was kept fixed.

Amongst all the positioning tasks given to the robot, in figure 5.3 is depicted one of the tested, the dash-dotted line. This trajectory has the following taught desired position,

$\mathrm{s}^* = [101.0\,,\,26.0\,,\,659.0\,,\,76.5\,,\,54.0\,,\,667.0\,,\,123.5\,,\,60.0\,,\,677.5](mm)$, and the following initial position, $\mathrm{s}_i = [107.5\,,\,38.0\,,\,670.0\,,\,81.0\,,\,65.5\,,\,675.0\,,\,129.5\,,\,72.5\,,\,690.0](mm)$.

Results are quite satisfactory, despite some initial oscillations of the 3D position error. The robot stabilizes and stops at the desired position with a small error, i.e., within 3 [mm]. This error was due to the precision of the robot (1 [mm] maximum) and the stereo vision system (4 [mm] maximum, in the depth direction). Figure 5.9, figure 5.10 and figure 5.11, show the error for each LED, with respect to the 3D coordinates X, Y, Z, respectively, obtained in one of several trajectories performed with the robot. The error is measured between the current robot position (obtained from the stereo vision system) and the taught desired position, for each one of the 3D directions. The visual servo control approach can stabilize the robot, as depicted in figures 5.9 to 5.11, which shows the evolution of the visual features error, during the trajectory.

This approach to visual servo control, based on fuzzy modeling to obtain an uncalibrated visual servo control system, is suitable to control the robot manipulator. The controller obtained presented excellent results, with errors within 3[mm] of the desired position, using the presented experimental setup.

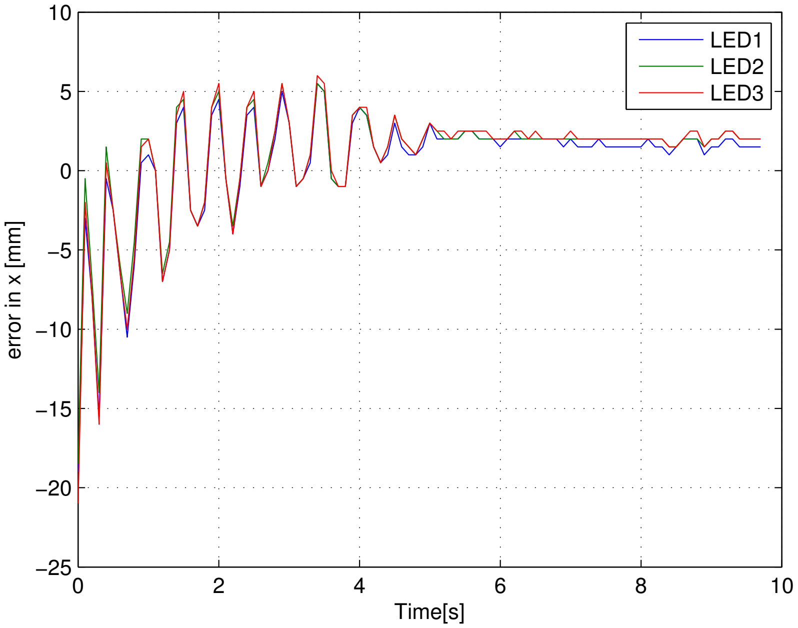

Figure 5.9: Evolution of the error of the position on the X coordinate.

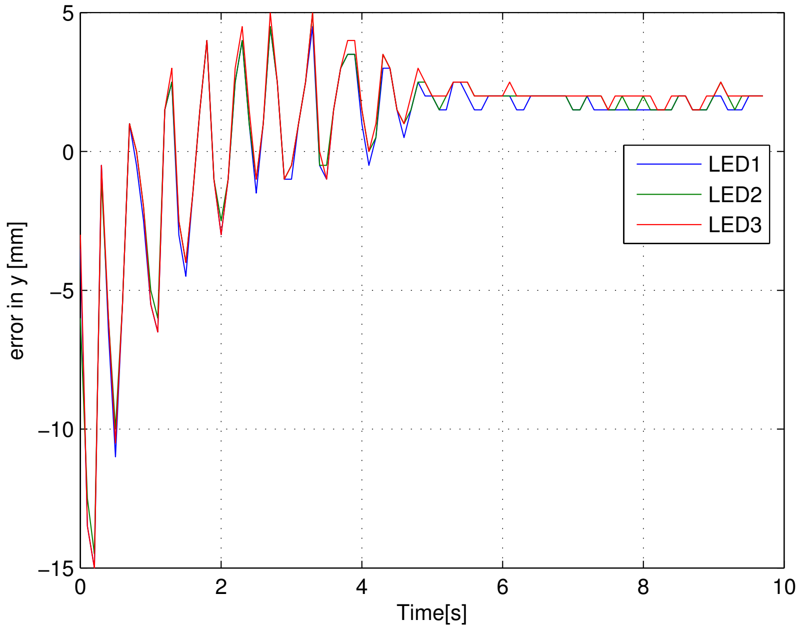

Figure 5.10: Evolution of the error of the position on the Y coordinate.

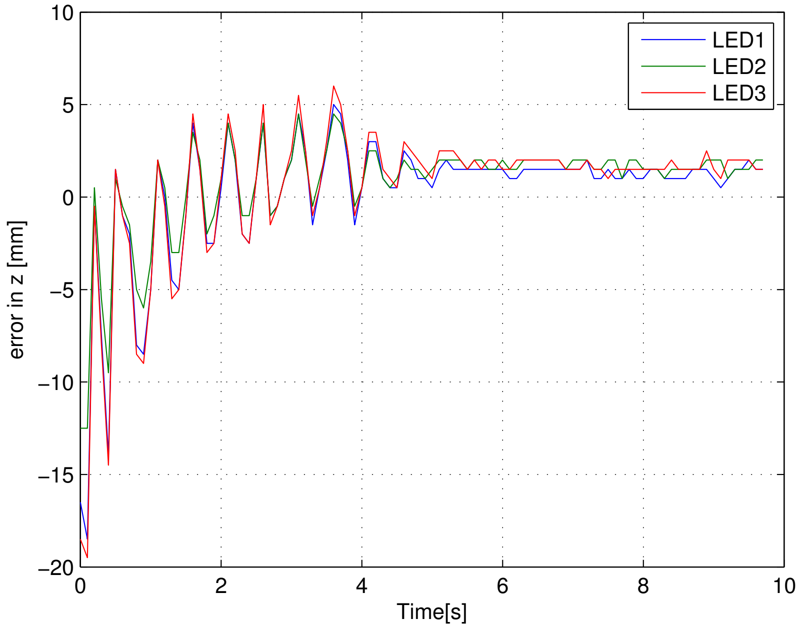

Figure 5.11: Evolution of the error of the position on the Z coordinate.

Chapter 6

Ultrasound Based Robot Navigation

This chapter presents the complete surgical navigation system, combining all the concepts already presented in previous chapters. Here are described the process of Bone Tracking based on 2D US images, the calibration methods and the robot navigation system for the operating room. Experimental tests performed in a human femur phantom, are described to validate the system.

6.1 Bone Tracking based on 2D US Images

This section describes the method developed for tracking the bone contour features in the US images, necessary to construct the 3D point cloud based on US images. From now on, named, 3D US bone model.

As there are no fiducial markers on the bone, all movements during the surgery are performed based on the information extracted from the US images. In other words, the Bone Tracking performed intra-operatively is based on bone contour features extracted slice by slice. The avoidance of fiducial markers implies that the US probe is referenced to the optical measurement system, depicted in figure 1.3. This referencing is made by placing a target with four markers in the US probe. From this moment, also the images and bone contour features are referenced to the tracker (NDI - Polaris).

The proposed method to track the femur in a sequence of 2D US images, allows 3D real-time measurement, which enables computer-assisted surgery for Hip Resurfacing Surgery. The flowchart of figure 6.1 helps to understand the method.

In **Initialization**, are performed all necessary initialization settings for the Optical Tracking System

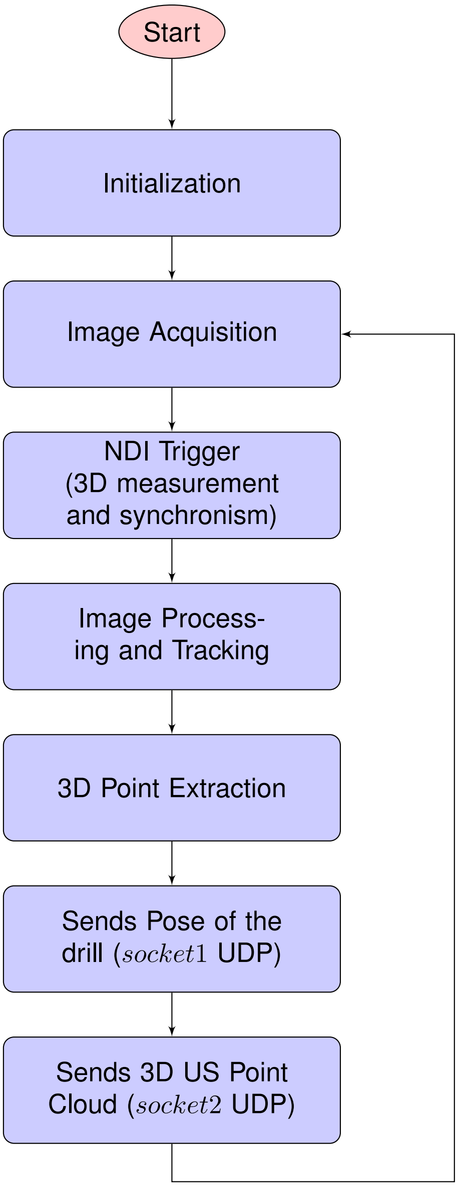
Start
Initialization
Image Acquisition
NDI Trigger (3D measurement and synchronism)
Image Processing and Tracking
3D Point Extraction
Sends Pose of the drill ($socket1$ UDP)
Sends 3D US Point Cloud ($socket2$ UDP)

Figure 6.1: Flowchart of the bone tracking based in US images.

and for the image processing algorithms.

Image Acquisition corresponds to the US image acquisition through a USB video frame grabber, which uses methods implemented in OpenCV. All images are acquired with 720×576 pixels resolution and a frame rate of 30 fps. The surgeon identifies the ROI, with a square around the bone in the first image acquired, as depicted in figure 6.2. This procedure improve accuracy and also speed up the segmentation.

In **NDI Trigger** action, is ordered to start the NDI Polaris acquisition and synchronize the tracking process. In this step, is read the position and orientation of the US probe and the extremity of the drill. Once the marker is placed on the drill, the offsets to the extremity, extracted across the drill pivoting technique (tool-tip offset), Pol (2006), need to be loaded. The synchronism between US images and Opto Tracker is established in the acquisition of the first US image by marking a point within the bone. The same point is used as the seed of the segmentation algorithm.

The **Image Processing and Tracking** action, corresponds to the task where images are processed with the aim of extracting the bone surface and enabling the tracking of the bone, based on US images. Here are applied methods to clean the images and to perform bone segmentation in all US images based on the *FastMarching* algorithm, described in section 3.1.2. The centroid of the segmented bone contour in each US image acquired, is used as input in the image segmentation of the next iteration, i.e., captured US image.

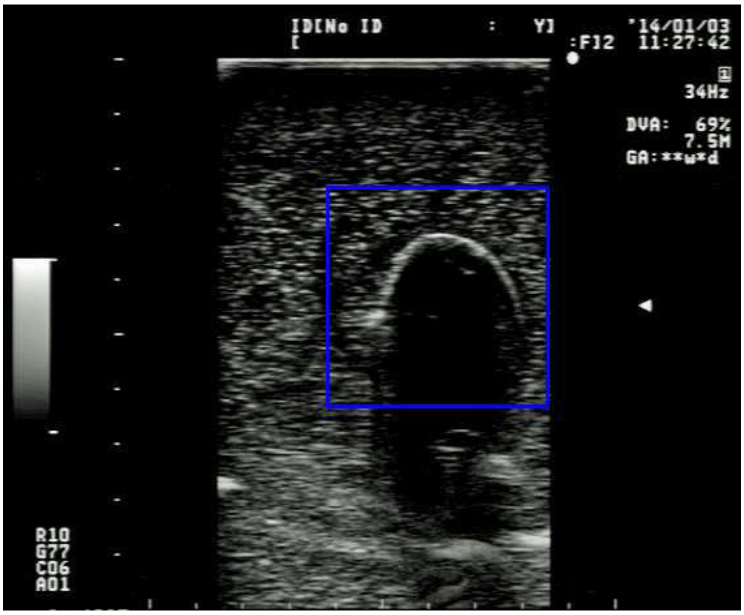

Figure 6.2: Region of interest in an US image of a femur phantom.

After extracting the 2D contour of each US image, it is identified the upper contour of the bone, extracted the correspondent pixel's coordinates and are calculated the 3D points in the NDI Polaris referential frame. The position and orientation of the drill are sent together with the 3D US point cloud, though in different sockets, by UDP to the workstation that performs the registration with the pre-operative 3D CT bone model. This process is continuously repeated until terminated by the surgeon, i.e., when the bone drilling surgical procedure ends.

6.2 Navigation System Calibration

This section presents the calibration procedures needed to relate the 3D US point cloud and the 3D CT bone models, indispensable to detect and track the bone movements.

In a real scenario, inside an operating room, the femur bone must be spatially located, to later identify the defined drilling point during pre-operative planning. Here appear the first challenges to be solved:

- What is the patient's location in the operating room, relatively to the robot and navigation system?
- Which is the location of the femur without the existence of markers? Pre-operatively, there is only a CT of the patient, the extracted femur point cloud, and the drilling point estimated in the CT reference frame. US is used to locate the femur in the intra-operative scenario, but...
- what is the relationship between CT and US, reference frames? The CT scan, was performed without any markers in the bone. The CT point cloud was extracted directly from the DICOM images, only knowing the relationship between slices, but the origin of its referential is completely unknown.

An initial calibration of the system is need, to answer the above questions. The main reference, in the intra-operative scenario, is the navigation system, (*NDI - POLARIS*), reference frame. The Homogeneous Transformation, that relates the intra-operative point clouds and the pre-operative model, CT dataset, need to be obtained. This transformation, ($^{CT}T_{NDI}$), is determined by a initial registration between the CT point clouds and 3D US bone point clouds extracted intra-operatively. With this transformation, all points in the femur are referenced to the CT reference frame.

Two calibration procedures are proposed in this thesis:

- First, after exposure of the femur head, a point cloud is extracted using the NDI Polaris pivot passive marker. The pivot is moved along the femur head in the region of *Greater*

Trochanter, according to the figure 6.3. The 3D point cloud extracted in this procedure is referenced to the opto-tracker, therefore, the registration between the CT point cloud and the former point cloud, returns the calibration matrix, ${}^{CT}T_{NDI}$.

- The second procedure, consists of performing a scan along the leg, with the US probe, while extracting the features of the femur. These features correspond to the points of the femur upper contour, referenced to the opto-tracker, since a passive marker is placed on the probe, as can be seen in figure 6.4. Again, the calibration matrix is obtained through the registration between the CT and US point clouds.

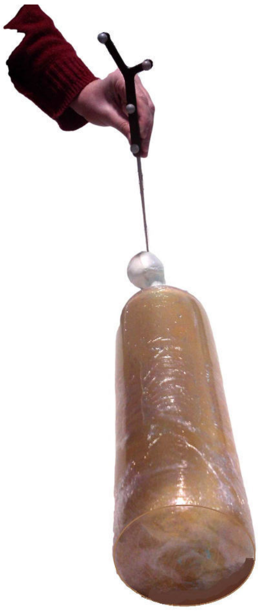

Figure 6.3: Detail the acquisition of points in the femur head (calibration method 1).

For both procedures, ${}^{CT}T_{NDI}$ is obtained according the flowchart of figure 6.5. After loading the two datasets, it is obtained the difference between the centroids (T_{R0}), of the *Moving* 3D US point cloud or the pivot point cloud of the head and the 3D CT point cloud. This difference will define the distance separating the two point clouds, and it is used to move the 3D US point cloud close to the 3D CT point cloud. The next step involves removing outliers through the *RANSAC* algorithm, Fischler & Bolles (1981). After global rigid registration based on ICP algorithm is applied to register the two point clouds. The output of this step is again used to perform a local registration and obtain a more refined result. The ${}^{CT}T_{NDI}$ transformation is then obtained through the relationship of the two consecutive registrations and initial offset, according to the equation 41, where T_{R2} and T_{R1} are the transformations obtained in both the local and global registrations, respectively.

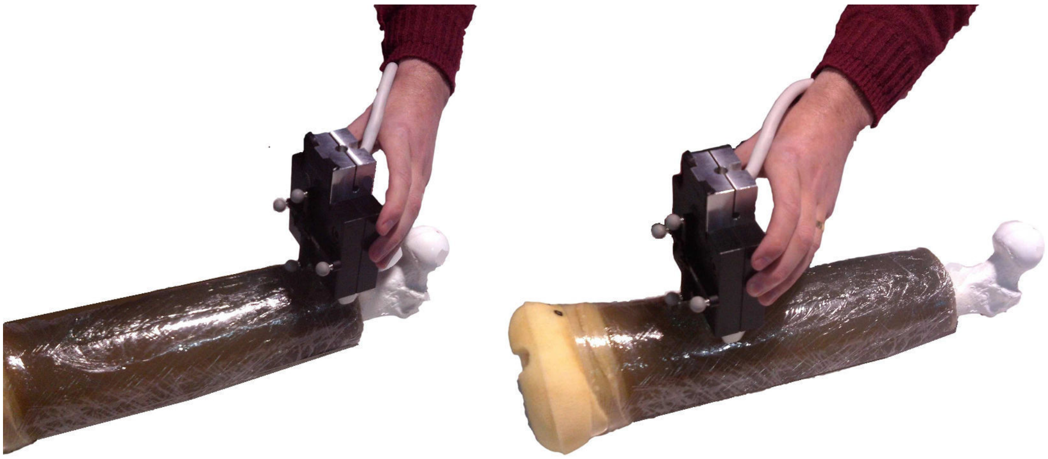
(a) (b)

Figure 6.4: Scan of the femur with the ultrasound probe to extract features (calibration method 2).

$$^{CT}T_{NDI} = T_{R2} \times T_{R1} \times T_{R0} \tag{41}$$

6.3 Robot Navigation

This section presents the method developed to update the drilling point location, in the robot reference frame, using the information described in the two sections before.

For a correct and accurate navigation of the robot during the surgical procedure it is very important that the navigation system can identify, and track the femur movements, and transmit them to the robot, to perform a correct update of the target's position and orientation, as soon as possible. Since this procedure takes place in the intra-operative scenario, all processing times have to be very fast (close to video-rate), but ensuring accuracy. To achieve these goals and because in the surgical procedures the femur does not change its position drastically, a local registration is performed on-line to update the target, based on the femur movements. As was written earlier, the ideal drilling point is estimated pre-operatively but needs to be spatially located within the intra-operative scenario, in order to be updated in case the femur moves. Intra-operatively the position and orientation of drilling point is measured with the NDI Polaris ($^{NDI}P_{drill}$). The same point is calculated in CT reference frame, considering the calibration matrix ($^{CT}T_{NDI}$), according to equation 42.

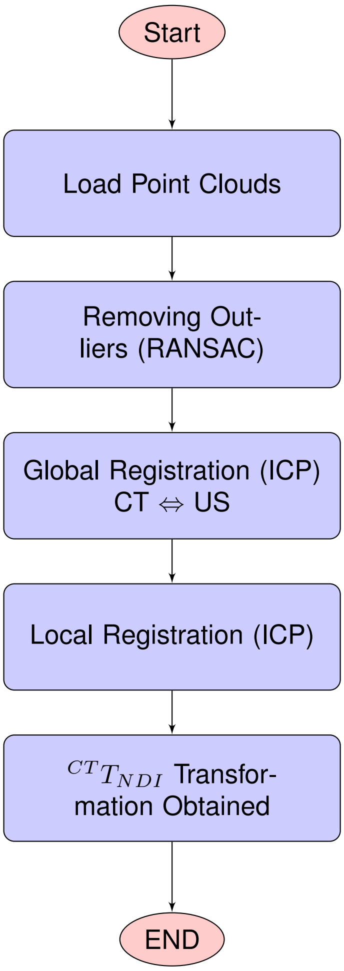
Start
Load Point Clouds
Removing Outliers (RANSAC)
Global Registration (ICP) CT ⇔ US
Local Registration (ICP)
$^{CT}T_{NDI}$ Transformation Obtained
END

Figure 6.5: Steps for obtaining $^{CT}T_{NDI}$ transformation matrix, during calibration process.

$$^{CT}P_{drill} =^{CT} T_{NDI} \times^{NDI} P_{drill} \tag{42}$$

The same point, calculated in the robot reference frame, considering the movements that may exist in the femur is given by equation 43.

$$(^{ROB}P_{drill})_k = (^{NDI}T_{ROB})^{-1} \times (^{CT}T_{NDI})^{-1} \times (T_R)_k \times^{CT} P_{drill} \tag{43}$$

where, $(T_R)_k$ is the homogeneous matrix that represent the transformation obtained in the on-line local registration, which updates the calibration to compensate the femur movements.

The target (drilling point) update, important for positioning the robot, is done by calculating the drilling point in the reference frame of the robot, at each instant, in order to track the movements that may exist in the femur. The flowchart of figure 6.6 illustrates the tasks performed to determine the on-line update of the target.

The parameters obtained pre-operatively and during calibration are loaded by the method in its initialization task. After the initial settings the method is ready to receive data by UDP. Receives at each instant, the robot pose ($^{NDI}T_{ROB}$) and the 3D point cloud of each slice. As shown in the flowchart, the method does not process the information of each slice individually received, but only sets of ten slices, to obtain a 3D US point cloud bone surface. This is because registration with a surface obtained better results compared to the slice by slice approach. Ten is the trade-off to ensure adequate speed and accuracy in the process. Each 3D US surface is calibrated with $^{CT}T_{NDI}$ in order to register the point cloud with the 3D bone model (CT). The RANSAC algorithm is used to filter the dataset before performing the local registration with the ICP algorithm, to obtain the $(T_R)_k$ matrix.

The new $^{ROB}P_{drill}$ is calculated using equation 43 and sent to the robot controller in order to follow the femur movements, if they exist. This process is repeated consecutively until terminated by the surgeon. The robotic system works on variable impedance control, (Pires (2014)), for physical surgeon-robot interaction and the real-time bone tracking is performed in open-loop, as depicted in figure 6.7. $^{NDI}T_{ROB}$ represents the drill position measure by the tracker and I, the US image used to track the bone movements.

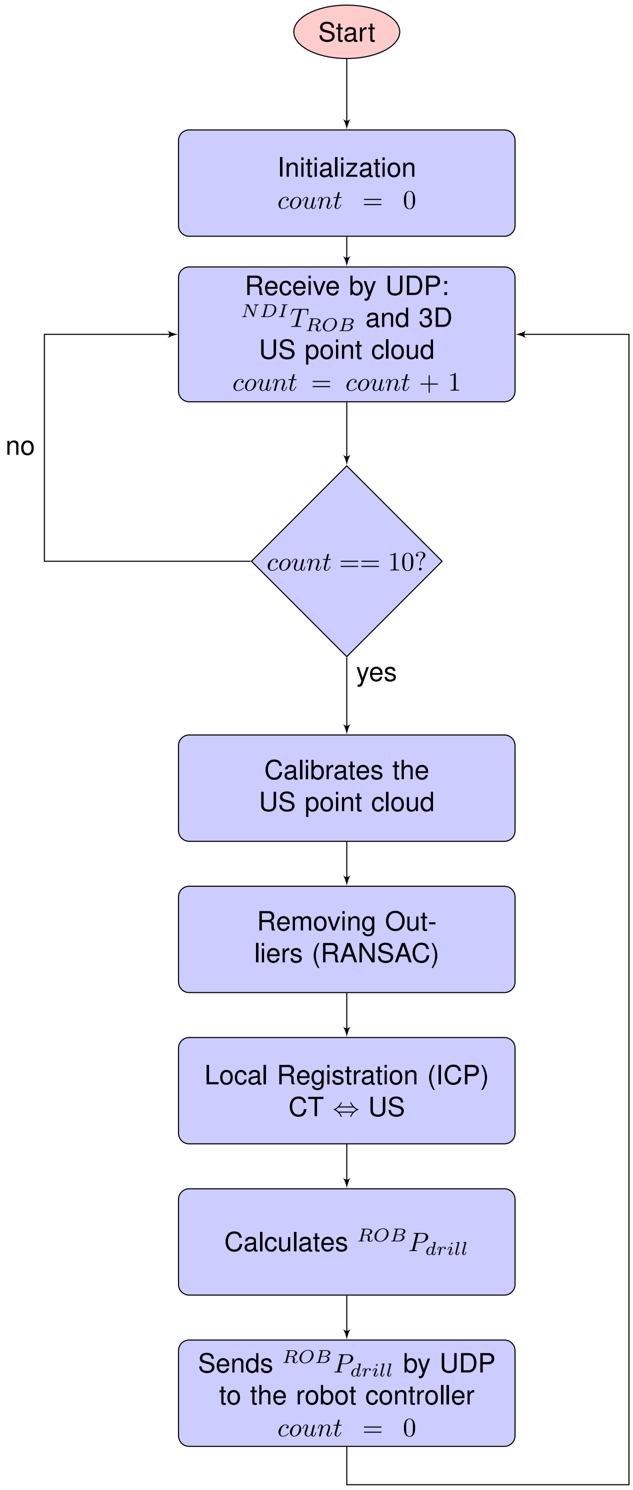
Start
Initialization
$count = 0$
Receive by UDP:
${}^{NDI}T_{ROB}$ and 3D
US point cloud
$count = count + 1$
no
$count == 10?$
yes
Calibrates the
US point cloud
Removing Outliers (RANSAC)
Local Registration (ICP)
CT ⇔ US
Calculates ${}^{ROB}P_{drill}$
Sends ${}^{ROB}P_{drill}$ by UDP
to the robot controller
$count = 0$

Figure 6.6: Flowchart that describes the calculation of the position and orientation of drilling point in the robot coordinates.

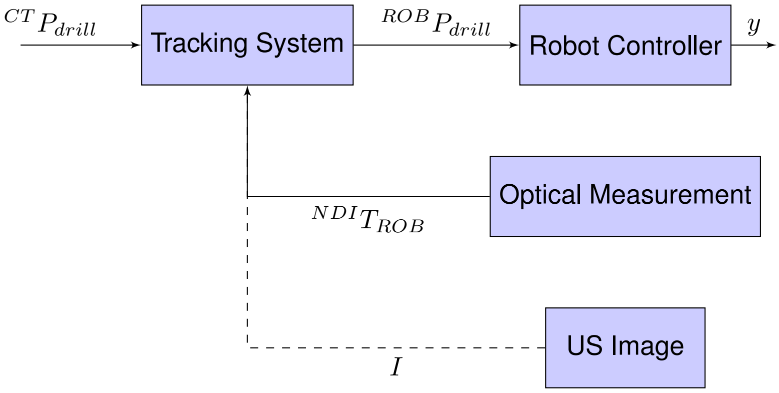
$^{CT}P_{drill}$
Tracking System
$^{ROB}P_{drill}$
Robot Controller
y
Optical Measurement
$^{NDI}T_{ROB}$
US Image
I

Figure 6.7: Block diagram of the open-loop robot control.

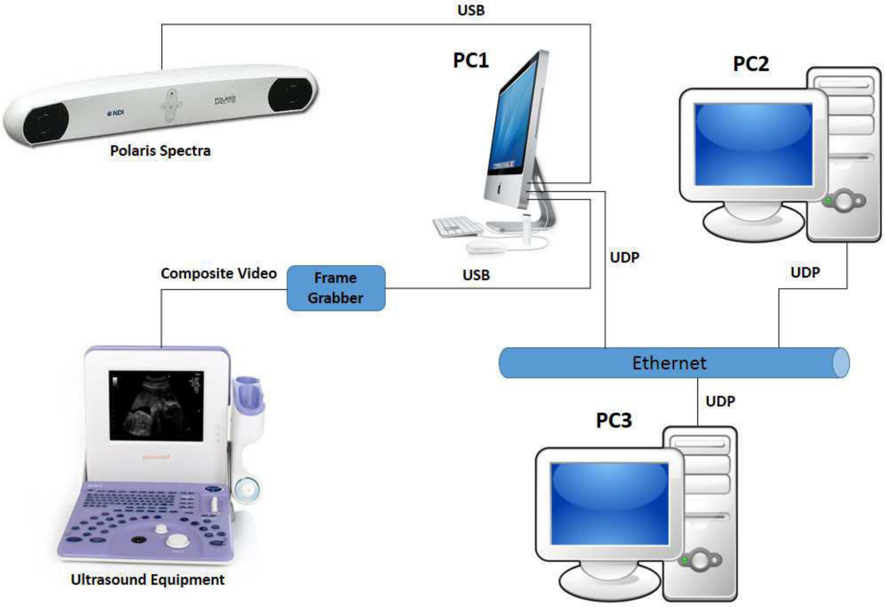
USB
PC1
PC2
Polaris Spectra
UDP
UDP
Composite Video
Frame Grabber
USB
Ethernet
UDP
PC3
Ultrasound Equipment

Figure 6.8: Experimental setup.

6.4 Experimental Setup

The experimental setup for Ultrasound Based Robot Navigation System is composed of three workstations, an optical measurement system (NDI Polaris Spectra), a portable ultrasound system (Aloka prosound 2), with a 5 MHz linear probe and a USB video frame grabber, as illustrated in figure 6.8. The vision-oriented software for bone tracking has been developed in C++ on NetBeans environment running on PC1 under OS X operating system. This computer, responsible for the Bone Tracking, is connected to the NDI Polaris and frame grabber by USB. The calibration, registration and Navigation applications, presented in sections 6.2 and 6.3 run on computer PC2 under Ubuntu Linux operating system.

Both applications, calibration and Navigation, have been developed in C++ using the Point Cloud Library (PCL), (Rusu & Cousins, 2011), for 3D point cloud processing, registration and visualization. Computer PC3 receives the updates obtained from the navigation system and implements the trajectory planning, (Pires (2014)), for real-time robot control. All computers are connected by Ethernet and communicate via UDP Protocol.

To perform experiments of robot positioning in real scenario (figure 6.9), it was constructed a femur phantom (figures 6.3, 6.4) with similar characteristics to a human femur.

At the beginning of the experiments it is necessary to define the US image scale factors, according to the image plane in which acquisitions will be made. A correct procedure goes through the femur scan with US probe, identify the desired zone and adjust the image plane, probe frequency, brightness, and focus. For the acquisitions presented in this section, the ultrasound system was configured to acquire images with an image plane of 10 [cm] (R10), Torres *et al.* (2011a), and probe frequency 7.5 MHz, as evidenced in figure 6.2, which results in scale factors Sx and Sy equal to 0.2858 [mm].

Another important task to perform is to calibrate the system, as described in section 6.2 to obtain the ${}^{CT}T_{NDI}$ transformation matrix. This matrix, automatically enters as input into the navigation software. This procedure takes an average of 5 minutes to be carried out, distributed by Acquisition and registration / calibration.

The final task to conclude calibration and initializations, passes for finding the drill tool-tip offset, in order to reference the drill extremity, to the robot wrist. This is referenced to the Polaris system according to the matrix 44, for all experiments. After performing the initializations / calibrations previously described, the surgeon or an assistant makes constant scans with the US probe along the femur. Another assistant starts the image processing station, defines the ROI and runs the application. Starting from this moment, the system is completely autonomous. It processes sets of 10 slices (US images), to obtain a 3D US point cloud, in order to perform the local registration and update the drilling point position and orientation, which is given to the robot's controller, as a set-point. Figure 6.10, depicts the experimental apparatus mounted to perform real-time experiments.

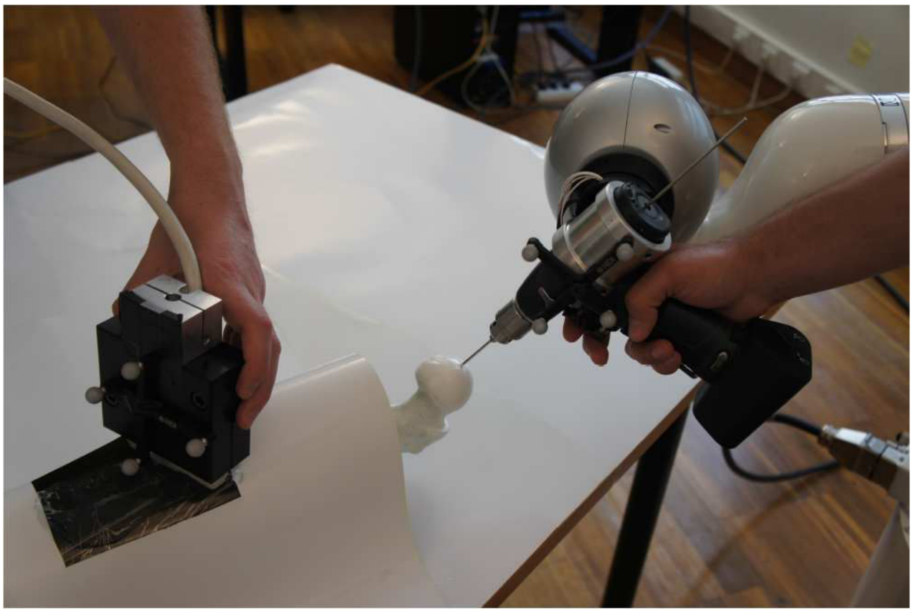

Figure 6.9: The Real Scenario of the femur phantom, the Us probe, and the drilling point in the femur head.

$$
{}^{NDI}T_{Mk} = \begin{pmatrix} {}^{NDI}R_{3\times3} & {}^{NDI}t_{3\times1} \\ 0_{3\times3} & 1 \end{pmatrix} \times \begin{pmatrix} 1 & 0 & 0 & -46,82 \\ 0 & 1 & 0 & 0,74 \\ 0 & 0 & 1 & -113,49 \\ 0 & 0 & 0 & 1 \end{pmatrix} \qquad (44)
$$

where, ${}^{NDI}T_{Mk}$ represents the Homogeneous matrix relating the position of the markers, to the tracker. These offsets (expressed in *mm*) correspond only to the markers placed on the drill.

6.5 Experimental Results

This section presents some of the results obtained from numerous experiments performed with this setup. Afterwards it is performed a global error analysis.

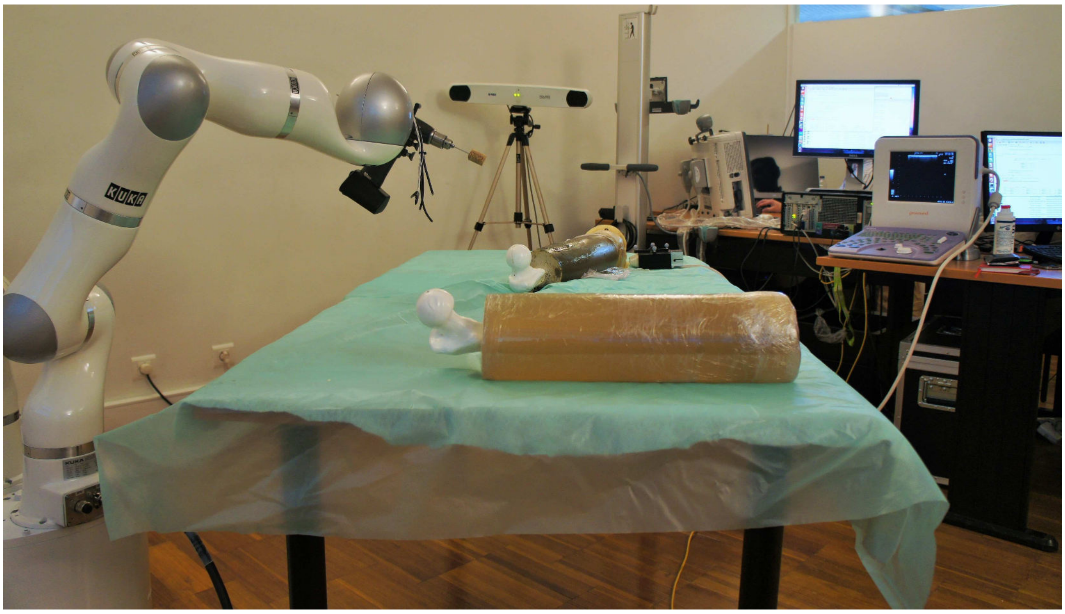

Figure 6.10: Experimental apparatus.

All bone contours were segmented successfully, enabling the accurate tracking of the bone movements. Figure 6.11 shows an output resulting of image processing and the contour points extraction, calibrated in the NDI referential frame, during the US video tracking process. The segmentation errors, presented in table 6.1 were calculated in a set of 599 US images. The segmentation method output was compared with manual segmentation performed by an expert. The results are expressed in $pixel$ and mm obtained from the Root Mean Squared Error (RMSE), Li & Zhao (2001), and Mahalanobis Distance (M_D), Bedrick *et al.* (2000). The segmentation results are within the values obtained by the scientific community, for this kind of images, Alfiansyah *et al.* (2009), Foroughi *et al.* (2007).

Figures 6.12 and 6.13, illustrate the registration process carried out by both methods, presented in section 6.2 in order to determine the calibration matrix $^{CT}T_{NDI}$. The target is the 3D CT femur bone, represented in green, the red point clouds corresponds to the femur features extracted with Polaris Marker in the head region and the features extracted through a scan with the US probe in the central part of the femur. In black is the registered point cloud. Figures 6.14 and 6.15 help to better detail the results after registration. As can be seen from the figures, the initial clouds are quite far, and both methods, first by a global registration and after a local refinement can successfully register the point clouds and find a relationship between them. The registration results presented in table 6.2 prove this and show that method 2 present better results, and is more realistic and practical to perform.

Completed the calibration process, the bone's movements are identified by registering the 3D

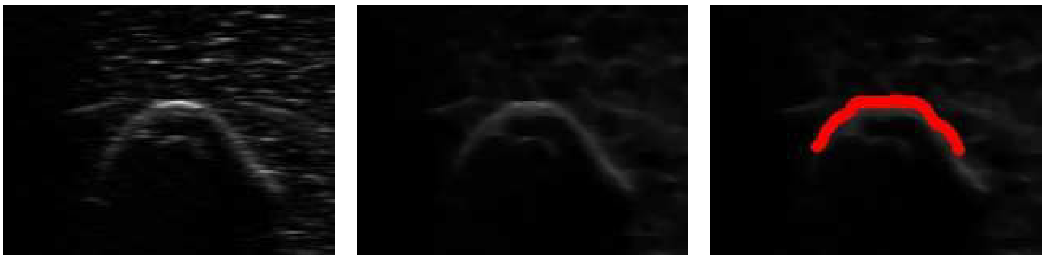

(a) ROI in the US image.

(b) Clean image.

(c) US points extracted of the segmentation.

Figure 6.11: Results of image processing during the tracking of the femur.

Table 6.1: Quantification of segmentation errors during the on-line femur tracking.

	$\overline{RMSE}$	σ_{RMSE}	$\overline{M_D}$	σ_{M_D}
$[pixel]$	4.0978	2.5462	3.8041	2.1202
$[mm]$	1.1712	0.7277	1.0872	0.6060

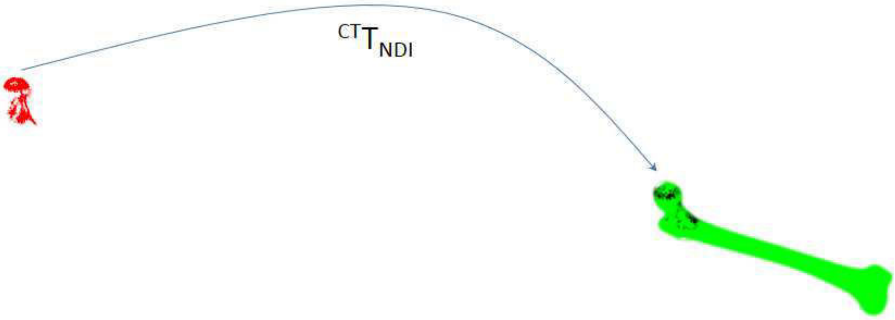

Figure 6.12: The registration process - calibration method 1. 3D CT point cloud (green). Point cloud of the femur head, before registration (red). Point cloud of the femur head, after registration (black).

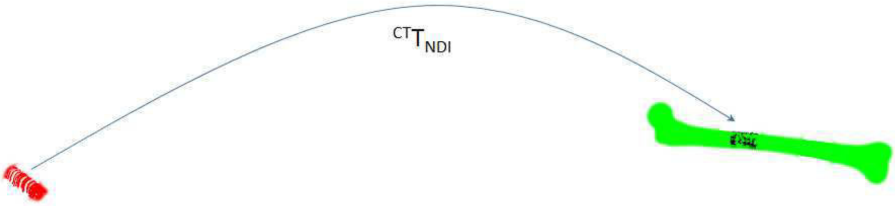

Figure 6.13: The registration process - calibration method 2. 3D CT point cloud (green). US point cloud, before registration (red). US point cloud, after registration (black).

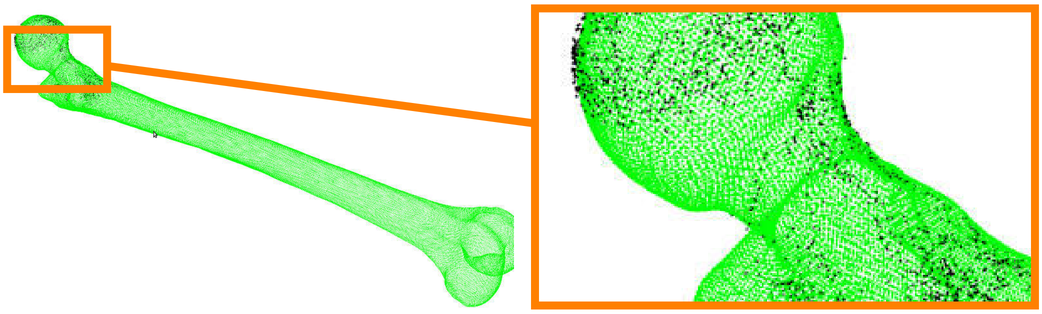

Figure 6.14: Local registration highlighting - calibration method 1.

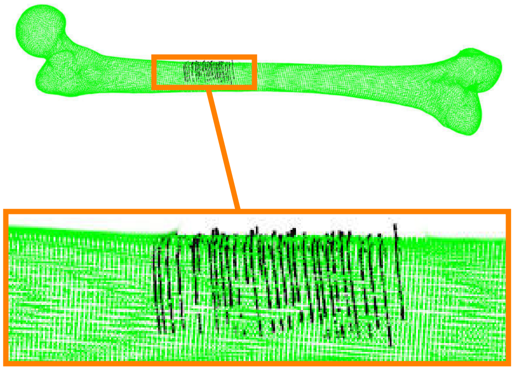

Figure 6.15: Local registration highlighting - calibration method 2.

Table 6.2: Calibration error results, after registration.

Registration error	$H_{dist}[mm]$
Method 1	0.801403
Method 2	0.756421

Table 6.3: Results before and after the on-line Registration Process.

	Before Registration $H_{dist}[mm]$	After Registration $H_{dist}[mm]$	Time $[s]$
Registration results (ICP)	1.0667	0.7936	0.32
Refinement of registration (CPD)	0.7936	0.6826	13.01

US point cloud obtained from 10 US images. The average update time between registrations is 0.32 seconds. Figure 6.16, presents a registration snapshot from the developed application, run in PC2. The point clouds at the left shows the Model (CT) and the US point cloud received from PC1 and in the right is presented the results after registration. The registration process incorporates calibration, global registration and refinement through local registration. Figure 6.17 illustrates and highlights the Local registration process. The use of CPD for local refinement is computationally more complex and slower, but improves the error results, however its use can be optional, for the surgeon. Figure 6.18 depicts the local registration of an experiment, performed with CPD. The registration errors (Table 6.3) obtained in this task are calculated by Hausdorff distance metric, Mémoli & Sapiro (2004).

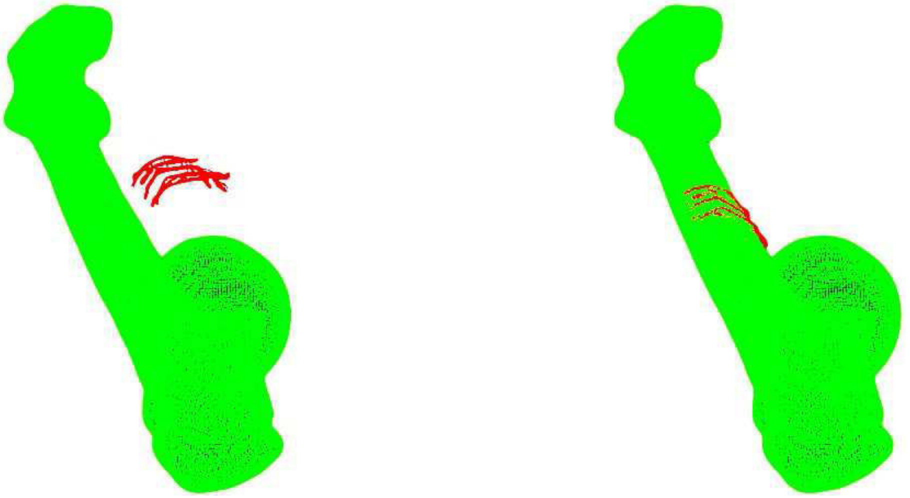

Figure 6.16: The registration process, snapshot from the developed application. Left, before registration, and right, after registration.

$$^{NDI}P_{drill} = (^{CT}T_{NDI})^{-1} \times (T_R)_k \times ^{CT} P_{drill} \tag{45}$$

$$\varepsilon = \triangle ^{NDI}P_{drill} - \triangle ^{NDI}T_{ROB} \tag{46}$$

Figure 6.19 represents both the drilling point ($^{NDI}P_{drill}$) and the robot's associated motions,

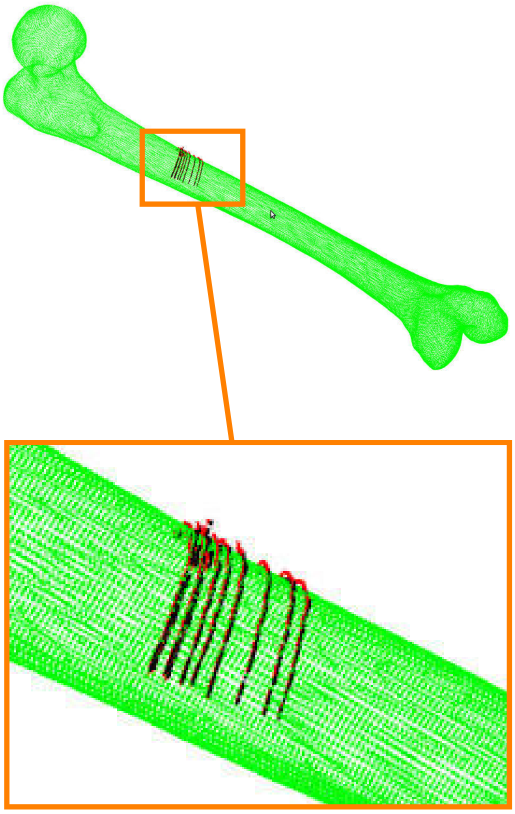

Figure 6.17: On-line local registration, highlighting. US point cloud, before local registration (red). US point cloud, after local registration (black), performed with ICP method.

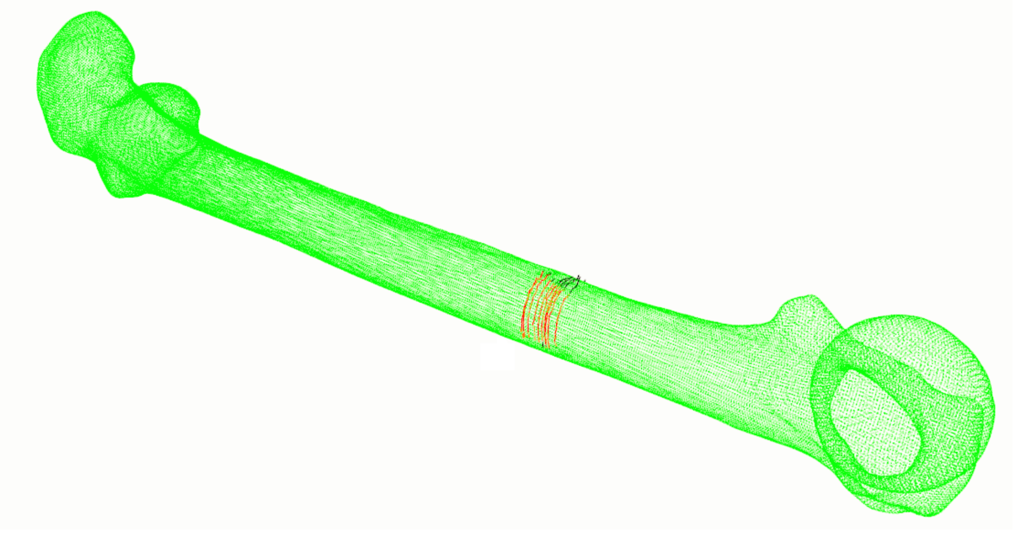

Figure 6.18: On-line local registration. CT point cloud (green). US point cloud, after local registration (red). US point cloud, after local refinement (black), performed with CPD method.

($^{NDI}T_{ROB}$), measured by the tracker during an experiment, represented in Cartesian coordinates. $^{NDI}P_{drill}$ is calculated according to equation 45 and $^{NDI}T_{ROB}$ is directly measured by the tracking system. In the numerous experiments performed, the system responded stably, the robot followed the femur's movements, randomly performed. The associated motion errors (ε) were calculated according to equation 46, and presented in table 6.4. $\triangle$ represents the differences between consecutive poses. These results were obtained in experiments where the bone is purposely randomly moved. With smooth movements of the bone, the tracking error improve significantly. An accuracy in the order of ± 2 mm / 2 .. 4° is achieved, which is aligned with the accuracy of current systems, Raaijmaakers *et al.* (2010), McMinn (2009).

Table 6.4: Errors between the drilling point variation and the corresponding variations of the robot, in the tracker reference frame.

	$\overline{norm}$	$\overline{\delta x}$	$\overline{\delta y}$	$\overline{\delta z}$
Position [mm]	6.06	1.77	3.77	1.23
Orientation [degree]	3.19	2.48	0.88	3.80

where $norm$ is the norm of the vector and δ represents the variation of position and orientation expressed in the orthonormal Cartesian system O_{xyz}.

Table 6.5 presents the tracking results obtained in 47 validated experiments. The errors were calculated in the representation of vector / angle, considering the current position and the moved drilling point at each instant, in the robot frame referential ($^{ROB}P_{drill}$).

Table 6.5: Movements of the drilling point.

	$\overline{norm}$	σ	Max	min
Position [mm]	7.64	3.56	14.60	1.46
Orientation [degree]	3.23	2.35	16.41	0.69

where Max and min, represent respectively the maximum and minimum values.

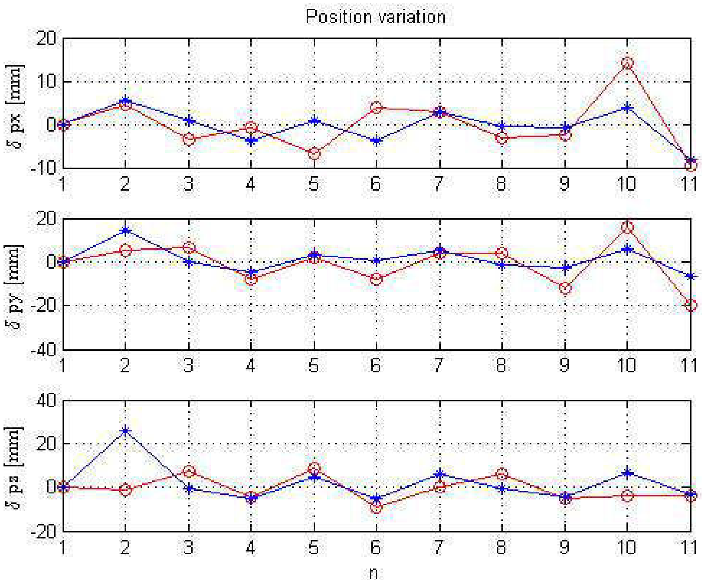

Figure 6.19: Bone movements (Red) and robot movements (Blue) during an experiment, represented in XYZ coordinates.

Chapter 7

Conclusions

In this last chapter are described the conclusions obtained from the work developed on this thesis. The contributions developed in this thesis that go beyond the state-of-the-art are presented, along with a discussion on the research lines followed, to achieve those contributions. The chapter concludes with proposals to future work.

7.1 General Conclusions

This thesis described a new approach for robot navigation during orthopaedic surgical procedures. The solution developed to track femur bones was successfully applied to Hip Resurfacing surgery. The system can also be adapted to other bone surgeries, that need a precise navigation of the surgical tools.

The developed robotic system can compensate for femur movements, during bone drilling procedures. It is useful to ensure the drill desired positioning in order to perform a hole in the femur head, necessary to implant the initial guide wire, which ensures the correct implant's alignment. The robot's navigation system is based entirely on the information extracted from images obtained from CT (pre-operatively) and US (intra-operatively). Contrary to current surgical systems, it does not use any type of implant in the bone, to track the femur movements. The intra-operative bone tracking is performed in real time by registration of 3D US points with the femur 3D model (CT).

During this thesis, several approaches have been followed, always with the goal to reach a viable solution for replacing fiducial markers used in orthopaedic surgery, towards an invasive image-based navigation. Since CT produces a detailed cross-sectional image comparatively to other medical imaging modalities, it was chosen to be used in the preoperative surgical planning. As US is a medical imaging technology with the capacity to deliver images at video-rate (50Hz), it was chosen to be used in the intra-operative scenario to acquire images of the femur during the surgical procedures. US imaging is a modality suited to track bone movements but produces noisy images, e.g., mainly speckle noise. It have a low signal to noise ratio, and is limited for tissue penetration, i.e., does not penetrate bones. As such, only the bone upper surface is represented in US bone images.

A major contribution from this thesis were the developed algorithms to obtain the relation between the images acquired intra-operatively (US) and the images previously processed pre-operatively (CT). The proposed solution was based on the registration of both 3D point clouds, extracted from CT and US images, respectively.

In this thesis, were proposed two solutions to acquire US images spatially located, in the intra-operative scenario. The first was a freehand system, where it was used the NDI Polaris opto tracker to measure the position and orientation of the US probe. The IGSTK toolkit was used to acquire and synchronize the images with the Polaris. Passive markers were placed on the US probe to measure its 3D pose and therefore find the position of each pixel in the US image.

The second solution is a non-freehand system, where the US probe is placed on the end-effector of an anthropomorphic robot. The robot is responsible to move the US probe along the leg and give a spatial location for each slice. This system has the advantage of obtaining images with the same distance between them. Both systems were tested in several acquisitions of human femurs. A combination of both systems would be a good solution, since it allows to acquire images evenly spaced and with high pixel location accuracy, provided by the Polaris system.

A new region-based approach for US images segmentation based on an existing algorithm, was proposed. This method presents excellent results in the segmentation of US images, compared with other conventional algorithms. The principal difficulty of image segmentation algorithms is to identify the bone boundary in noisy and blurred images, such as US images. The proposed method identifies correctly the bone contour and rejects other regions in the images with pixel intensities similar to bones. The same method was used in the femur head's segmentation in CT images and the results confirm the method's flexibility and robustness.

After the image processing tasks the 3D CT and US surfaces were extracted and registered, with the methods, ICP and CPD. The last method is more accurate but is more time consuming comparatively to ICP, as such is not a good solution to perform registration in real time applications. The ICP has the difficulty to obtain good results if the "*Moving*" dataset (3D US point cloud) is far from the target (CT point cloud). To solve this, the difference between the centroids of both datasets were computed and used to move the ”*Moving*” cloud close to the target. After this approximation, a global rigid registration was performed with ICP. The output was again used to perform a local registration and obtain a more refined result. The local refinement results could be improved if used the CPD, instead the ICP method, however is only an option for the surgeon, because is a more time-consuming process.

To control the robot using visual feedback, an approach where the visual motor interaction is estimated, using fuzzy models, was also presented. The Fuzzy based approach was validated using an experimental setup developed for visual servoing experiments, under real working conditions. The experimental results allows to identify real implementation issues regarding the visual frame rate, the error introduced by the visual data, and its implications to robot control. The knowledge obtained from these experiments and the results obtained, have opened a path to implement a control system with visual servoing using US images.

Following the previous presented contributions of this thesis, a new approach for US based robot navigation was developed. This approach combine the developments proposed in this thesis to obtain a solution to close the control loop for robotic motion compensation of the femur, using US images. A KUKA lightweight robot was used to validate the applicability of the bone tracking system in the experimental tests carried out on a femur phantom. During the experiments the drilling point update was validated, with errors less than 2 mm / 3°. This accuracy values are in line with the current conventional alignment systems, which demonstrates that the solution found in this thesis, is valid and have applicability. The drilling point update, calculated in the reference frame of the robot, is obtained at each 6 seconds. This value includes the time for image acquisition and processing, registration and the calculation of the new drilling point pose. This value should be improved in order to increase the robustness and stability of the navigation system, and allow that this approach can be used as a real time solution to assist the surgeon in the drilling procedures, during the HR surgery.

This thesis finally demonstrated that is possible to track the bone’s movements only with image information. However, the system accuracy must be improved in order to be a valid solution for experimental tests on corpses. Position errors less than 1 mm are needed for a real application, and is possible to obtain this precision with improvements in the different tasks of this thesis. In the next section are discussed and proposed ideas for future work, that could be implemented to improve the system, and take it to the operating room.

7.2 Suggestions for Future Work

During this thesis's developments, a number of open problems were solved in order to obtain a solution to track bones in orthopaedics surgery, without any marker in bone. These problems suggest a variety of research directions that need to be pursued to improve the work and develop a system feasible with application in the operating room.

The first suggestion consists in use a professional ultrasound equipment with a high resolution linear transducer (7-12 MHz) and a new frame grabber with high video definition for more resolution, in order to improve the quality of images in the acquisition tasks. The improvements in acquisition allow better results in the image processing tasks and certainly the precision and accuracy of segmentation will be improved.

Another suggestion is use a robot manipulator with a ultrasound probe in eye-in-hand configuration, to perform the femur's scan. With this proposal the ultrasound slices are acquired with the same spacing and the same pressure on the leg, that produces image datasets suited to obtain 3D data from them.

The registration results could be improved, if the registration between datasets is performed based in other types of features, (e.g. shape, curvature, normals, etc), instead of only 3D points. A possible drawback could be the computational time needed to obtain these features.

Another interesting line of research is the investigation of a new registration method, less sensitive to initialization and to the distance between the point clouds. One suggestion is combine the benefits of probabilistic methods such as CPD, with the speed of methods such as ICP.

The experimental setup could be changed in order to use only one workstation to perform the tasks of acquisition, registration and tracking. The processing times can be improved if is used GPU-accelerated computing in the image processing and registration tasks.

Finally, some markers could be placed in the region of femur's head, after the intra-operative exposure, to aid the tracking system in the bone movements detection during surgery. As these markers are rigidly attached on a intervention region, don't damage the bone and will be a good solution to obtain a referencing point. The pose of these markers are directly measured by the opto-tracker system.

After improving the systems reproducibility and repeatability with the reduction of tracking errors, experimental tests should be performed in corpses to validate the applicability of the robot navigation system proposed in this thesis.

Bibliography

(2006). *Polaris Spectra Tool Kit Guide*. Northern Digital Inc.

ABOLMAESUMI, P., SALCUDEAN, E. & ZHU, H. (2000). Visual servoing for robot-assisted diagnostic ultrasound. *Engineering in Medicine and Biology Society. Proceedings of the 22nd Annual International Conference of the IEEE*, **4**, 2532 – 2535.

ABOLMAESUMI, P., SALCUDEAN, S., ZHU, W.H., SIROUSPOUR, M. & DIMAIO, S. (2002). Image-guided control of a robot for medical ultrasound. *Robotics and Automation, IEEE Transactions on*, **18**, 11 –23.

ADAMS, L., KRYBUS, W., MEYER-EBRECHT, D., RUEGER, R., GILSBACH, J., MOESGES, R. & SCHLOENDORFF, G. (1990). Computer-assisted surgery. *Computer Graphics and Applications, IEEE*, **10**, 43–51.

ALFIANSYAH, A., NG, K. & LAMSUDIN, R. (2009). Deformable model for serial ultrasound images segmentation: Application to computer assisted hip athroplasty. In C. Lim & J. Goh, eds., *13th International Conference on Biomedical Engineering*, vol. 23 of *IFMBE Proceedings*, 1073–1076, Springer Berlin Heidelberg.

AMIOT, L. & POULIN, F. (2004). Computed tomography-based navigation for hip, knee, and spine surgery. *Clin. Orthop. Relat. Res.*, **421**, 77–86.

ANGELOV, P. & FILEV, D. (2004). An approach to online identification of takagi-sugeno fuzzy models. *IEEE Transactions on Systems, Man, and Cybernetics, Part B: Cybernetics*, **34**, 484–498.

AYADI, A., BAYLE, B., GRAEBLING, P. & GANGLOFF, J. (2008). An image-guided robot for needle insertion in small animal. accurate needle positioning using visual servoing. In *IROS*, 1453–1458.

BACHTA, W. & KRUPA, A. (2006). Towards ultrasound image-based visual servoing. *Proceedings of the 2006 IEEE International Conference on Robotics and Automation, Orlando, Florida*.

BAILEY, C., GUL, R., FALWORTH, M., ZADOW, S. & OAKESHOTT, R. (2009). Component alignment in hip resurfacing using computer navigation. *Clinical orthopaedics and Related Research*, **467**, 917–922.

BANIASADIPOUR, A., ZOROOFI, R., SATO, Y., NISHII, T., NAKANISHI, K., TANAKA, H., SUGANO, N., YOSHIKAWA, H., NAKAMURA, H. & TAMURA, S. (2007). A fully automated method for segmentation and thickness map estimation of femoral and acetabular cartilages in 3d ct images of the hip. In *Image and Signal Processing and Analysis, 2007. ISPA 2007. 5th International Symposium on*, 92 –97.

BEASLEY, R.A. (2012). Medical robots: Current systems and research directions. *Journal of Robotics*.

BEDRICK, E.J., LAPIDUS, J. & POWELL, J.F. (2000). Estimating the mahalanobis distance from mixed continuous and discrete data. *Biometrics*, **56**, 394–401.

BEITZEL, J., AHMADI, S.A., KARAMALIS, A., WEIN, W. & NAVAB, N. (2012). Ultrasound bone detection using patient-specific ct prior. In *Engineering in Medicine and Biology Society (EMBC), 2012 Annual International Conference of the IEEE*, 2664–2667.

BERRY, D. & LIEBERMAN, J. (2013). *Surgery of the Hip*. Elsevier.

BESL, P.J. & MCKAY, N.D. (1992). A method for registration of 3-d shapes. *Pattern Analysis and Machine Intelligence*, **14(2)**, 239 – 256.

BEZDEK, J. (1981). *Pattern Recognition With Fuzzy Objective Functions*. Plenum Press, New York.

BRENDEL, B., WINTER, S., RICK, A., STOCKHEIM, M. & ERMERT, H. (2002). Registration of 3d ct and ultrasound datasets of the spine using bone structures. *Computer Aided Surgery*, **7 (3)**, 146–155.

CATARINO, N.M.M., GONÇALVES, P.J.S. & TORRES, P.M.B. (2012). Bone contour segmentation from us images - a comparative study. *Proceedings of RECPAD 2012, 18th Portuguese Conference on Pattern Recognition*.

CHAN, T. & VESE, L. (2001). Active contours without edges. *Image Processing, IEEE Transactions on*, **10**, 266 –277.

CHEN, A.P.P.D., T. & ELLIS, R. (2005). A system for ultrasoundguided computer-assisted orthopaedic surgery. *Journal of Computer Aided Surgery*, **10**, 281–292.

CHIU, S.L. (1994). Fuzzy model identification based on cluster estimation. *Journal of Intelligent Fuzzy Systems*, **2**, 267–278.

COBB, J., HENCKEL, J., GOMES, M., BARRETT, A., HARRIS, S., JAKOPEC, M., RODRIGUEZ, F. & DAVIES, B. (2006). Hands-on robotic unicompartmental knee replacement: a prospective, randomised controlled study of the acrobot system. *The Journal of Bone and Joint Surgery B*, **88**, 188–197.

DANG, H., GU, L., ZHUANG, X. & LUO, Z. (2010). Hierarchical normal vector information based registration for surgical navigation by using saliency information. 137–142.

DAVIES, B., RODRIGUEZ Y BAENA, F., BARRET, A., GOMES, M., HARRIS, S., JAKOPEC, M. & COBB, J. (2007). Robotic control in knee joint replacement surgery. *Proc Inst Mech Eng [H]*, **221(1)**, 71–80.

DAVIS, E., GALLIE, P., MACGROARTY, K., WADDELE, J. & SCHEMITSCH, E. (2007). The accuracy of image-free computer navigation in the placement of the femoral component of the birmingham hip resurfacing. *The Bone & Joint Journal*, **89**, 557–560.

DESCOTEAUX, M., AUDETTE, M., CHINZEI, K. & SIDDIQI, K. (2006). Bone enhancement filtering: application to sinus bone segmentation and simulation of pituitary surgery. *Computer aided surgery : official journal of the International Society for Computer Aided Surgery*, **11**, 247–255.

FISCHLER, M.A. & BOLLES, R.C. (1981). Random sample consensus: A paradigm for model fitting with applications to image analysis and automated cartography. *Commun. ACM*, **24**, 381–395.

FOROUGHI, P., BOCTOR, E., SWARTZ, M., TAYLOR, R. & FICHTINGER, G. (2007). Ultrasound bone segmentation using dynamic programming. In *Ultrasonics Symposium, 2007. IEEE*, 2523–2526.

GANAPATHI, M., VENDITTOLI, P.A., LAVIGNE, M. & GUNTHER, K.P. (2009). Femoral component positioning in hip resurfacing with and without navigation. *Clinical orthopaedics and Related Research*, **467**, 1341–1347.

GINHOUX, R., GANGLOFF, J., DE MATHELIN, M., S., L., SANCHEZ, M. & MARESCAUX, J. (2005). Active filtering of physiological motion in robotized surgery using predictive control. *IEEE Transactions on Robotics*, **21**, 67–79.

GONÇALVES, P. & FERNANDES, J. (2008). Tools for an ultrasound based 3d bone model reconstruction, registration and visualization system. *Euromedia 2008, Workshop on Medical Imaging Systens, Porto, Portugal*.

GONÇALVES, P., MENDONÇA, L., SOUSA, J. & PINTO, J.C. (2008). Uncalibrated eye-to-hand visual servoing using inverse fuzzy models. *IEEE Transactions on Fuzzy Systems*, **16**, 341–353.

GONÇALVES, P.J.S. & TORRES, P.M.B. (2010). Extracting bone contours in ultrasound images: Energetic versus probabilistic methods. *Romanian Review Precision Mechanics, Optics & Mechatronics*, 105–110.

GONÇALVES, P.J.S., CARVALHO, M.V., MATEUS, D. & B., T.P.M. (2009). Registo de imagens ecográficas com modelo 3d de ossos - aplicação ao fémur. *Revista Ibérica de Sistemas e Tecnologias de Informação*, 43–56.

GONÇALVES, S.J., P.J.S. & PINTO, J.C. (2008). Evolving fuzzy modeling of an uncalibrated visual servoing system. *In Lecture Notes in Computer Science, Springer-Verlag Berlin*, **5112**, 1041–1050.

GRANGER, S., PENNEC, X. & ROCHE, A. (2010). Rigid point-surface registration using an em variant of icp for computer guided oral implantology. In *Medical Image Computing and Computer-Assisted Intervention MICCAI 2001*, 752–761, Springer.

GUILLAUME, S. (2001). Designing fuzzy inference systems from data: an interpretability-oriented review. *IEEE Transactions on Fuzzy Systems*, **9**, 426–443.

GUMPRECHT, H., WIDENKA, D. & LUMENTA, C. (1999). Brainlab vectorvision neuronavigation system: technology and clinical experiences in 131 cases. *Neurosurgery*, **44**, 97–104.

GUSTAFSON, D.E. & KESSEL, W.C. (1979). Fuzzy clustering with a fuzzy covariance matrix. In *Proceedings of the IEEE Conference on Decision and Control*, 761–766, San Diego, USA.

HACIHALILOGLU, I., WILSON, D., GILBART, M., HUNT, M. & ABOLMAESUMI, P. (2013). Non-iterative partial view 3d ultrasound to ct registration in ultrasound-guided computer-assisted orthopedic surgery. *International Journal of Computer Assisted Radiology and Surgery*, **8**, 157–168.

HAGN, U., NICKL, M., JÖRG, S., PASSIG, G., BAHLS, T., NOTHHELFER, A., HACKER, F., LE-TIEN, L., ALBU-SCHÄFFER, A., KONIETSCHKE, R., GREBENSTEIN, M., WARPUP, R., HASLINGER, R., FROMMBERGER, M. & HIRZINGER, G. (2008). The DLR MIRO: a versatile lightweight robot for surgical applications. *Industrial Robot: An International Journal*, **35**, 324–336.

HARRIS, S., F., A.C., MEI, Q., HIBBERD, R., DAVIES, B., WICKHAM, J., NATHAN, M. & KUNDU, B. (1997). The probot - an active robot for prostate resection. *Proc Inst Mech Eng H.*, **211**, 317–25.

HASHIMOTO, K. (2003). A review on vision-based control of robot manipulators. *Advanced Robotics*, **17**, 969–991.

HILL, J. & PARK, W. (1979). Real time control of a robot with a mobile camera. In *9th International Symposium on Industrial Robots*, 233–246.

HODGSON, A., HELMY, N., MASRI, B., GREIDANUS, N., INKPEN, K., DUNCAN, C., GARBUS, D. & ANGLIN, C. (2007). Comparative repeatability of guide-pin axis positioning in computer-assisted and manual femoral head resurfacing arthroplasty. *Proc Inst Mech Eng.*, **221**, 713–724.

HUTCHINSON, S., HAGER, G. & CORKE, P. (1996). A tutorial on visual servo control. *IEEE Transactions on Robotics and Automation*, **12**, 651–670.

IBÁÑEZ LUIS, N.L., SCHROEDER WILL & JOSH, C. (2005). The itk software guide second edition update for itk version 2.4. [manual] http://www.itk.org/itksoftwareguide.pdf. *Insight Software Consortium.*.

JANG, J. (1993). Anfis: Adaptive-network-based fuzzy inference system. *IEEE Transactions on Systems, Man, and Cybernetics*, **3**, 665–685.

KATHER, J., HAGEN, M.E., MOREL, P. & FASEL, J. (2010). Robotic hip arthroscopy in human anatomy. 301–305.

KAZANZIDES, P., MITTELSTADT, B., MUSITS, B., BARGAR, W., ZUHARS, J., WILLIAMSON, B., CAIN, P. & CARBONE, E. (1995). An integrated system for cementless hip replacement. *Engineering in Medicine and Biology Magazine, IEEE*, **14**, 307 –313.

KONIETSCHKE, R., HAGN, U., NICKL, M., JORG, S., TOBERGTE, A., PASSIG, G., SEIBOLD, U., LE-TIEN, L., KUBLER, B., GROGER, M., FROHLICH, F., RINK, C., ALBU-SCHAFFER, A., GREBENSTEIN, M., ORTMAIER, T. & HIRZINGER, G. (2009). The dlr mirosurge - a robotic system for surgery. In *Robotics and Automation, 2009. ICRA '09. IEEE International Conference on*, 1589–1590.

KRUPA, A. & CHAUMETTE, F. (2006). Guidance of an ultrasound probe by visual servoing. *Advanced Robotics*, **20**, 1203–1218.

KRUPA, A., GANGLOFF, J., DOIGNON, C., DE MATHELIN, M., MOREL, G., LEROY, J., SOLER, L. & MARESCAUX, J. (2003). Autonomous 3-d positioning of surgical instruments in robotized laparoscopic surgery using visual servoing. *IEEE Trans. on Robotics and Automation*, **19**, 842–853.

KRUPA, A., MOREL, G. & DE MATHELIN, M. (2004). Achieving high precision laparoscopic manipulation through adaptive force control. *Advanced Robotics*, **18**, 905–926.

KRUSE, R., GEBHARDT, J. & KLAWONN, F. (1994). *Foundations of fuzzy systems*. John Wiley and Sons, Chichester.

LEE, B., YUN, J., SEO, J., SHIM, B., SHIN, Y.G. & KIM, B. (2010). Fast high-quality volume ray casting with virtual samplings. *Visualization and Computer Graphics, IEEE Transactions on*, **16**, 1525 –1532.

LI, C., KAO, C.Y., GORE, J. & DING, Z. (2008). Minimization of region-scalable fitting energy for image segmentation. *Image Processing, IEEE Transactions on*, **17**, 1940 –1949.

LI, T., KERMORGANT, O. & KRUPA, A. (2012). Maintaining visibility constraints during tele-echography with ultrasound visual servoing. In *Robotics and Automation (ICRA), 2012 IEEE International Conference on*, 4856–4861.

LI, X.R. & ZHAO, Z. (2001). Measures of performance for evaluation of estimators and filters. vol. 4473, 530–541.

LORENSEN, W.E. & CLINE, H.E. (1987). Marching cubes: A high resolution 3d surface construction algorithm. *COMPUTER GRAPHICS*, **21**, 163–169.

MAINTZ, J.B.A. & VIERGEVER, M.A. (1998). A survey of medical image registration. *Image (Rochester, N.Y.)*, **2**, 1–37.

MALIS, E., CHAUMETTE, F. & BOUDET, S. (1999). 2 $\frac{1}{2}$ d visual servoing. *IEEE Transactions on Robotics and Automation*, **15**, 238–250.

MALLADI, R., SETHIAN, J. & VEMURI, B. (1995). Shape modeling with front propagation: a level set approach. *Pattern Analysis and Machine Intelligence, IEEE Transactions on*, **17**, 158–175.

MANTWILL, F., SCHULZ, A.P., FABER, A., HOLLSTEIN, D., KAMMAL, M., FAY, A. & JU, C. (2005). Robotic systems in total hip arthroplasty is the time ripe for a new approach. **1**, 8–19.

MARESCAUX, J., LEROY, J., GAGNER, M., RUBINO, F., MUTTER, D., VIX, M., BUTNER, S. & SMITH, M. (2001). Transatlantic robot-assisted telesurgery. *Nature*, **413**, 379–80.

MARION, P., R. KWITT, B.D. & GSCHWANDTNER, M. (2012). Pcl and paraview - connecting the dots. In *CVPR Workshop on Point Cloud Processing (PCP)*.

MATHARU, G.S., MCBRYDE, C.W., REVELL, M.P. & PYNSENT, P.B. (2013). Femoral neck fracture after birmingham hip resurfacing arthroplasty: Prevalence, time to fracture, and outcome after revision. *The Journal of arthroplasty*, **28**, 147–153.

MCMINN, D.J.W. (2009). *Modern Hip Resurfacing*. Springer Science & Business Media.

MEBARKI, R., KRUPA, A. & CHAUMETTE, F. (2008). Image moments-based ultrasound visual servoing. *IEEE International Conference on Robotics and Automation, Pasadena, CA, USA*, 19–23.

MEBARKI, R., KRUPA, A. & CHAUMETTE, F. (2010). 2-d ultrasound probe complete guidance by visual servoing using image moments. *IEEE TRANSACTIONS ON ROBOTICS*, **26,N.2**, 296–306.

MÉMOLI, F. & SAPIRO, G. (2004). Comparing point clouds. In *Proceedings of the 2004 Eurographics/ACM SIGGRAPH Symposium on Geometry Processing*, SGP '04, 32–40, ACM, New York, NY, USA.

MIEHLKE, R., HAAKER, R. & KONERMANN, W. (2004). The orthopilot navigation system in total knee arthroplasty: Version 4.0. In *Navigation and Robotics in Total Joint and Spine Surgery*, 242–247, Springer Berlin Heidelberg.

MOGHARI, M. & ABOLMAESUMI, P. (2007). Point-based rigid-body registration using an unscented kalman filter. *Medical Imaging, IEEE Transactions on*, **26**, 1708–1728.

MORAR, A., MOLDOVEANU, F. & GROLLER, E. (2012). Image segmentation based on active contours without edges. In *Intelligent Computer Communication and Processing (ICCP), 2012 IEEE International Conference on*, 213 –220.

MORGADO, P., PINTO, J.C., MARTINS, J.M.M. & GONÇALVES, P. (2009). Cooperative eye-in-hand/stereo eye-to-hand visual servoing. In *Proceedings of RecPad 2009 - 15th Portuguese COnference on Pattern Recognition*, Aveiro, Portugal.

MUIRHEAD-ALLWOOD, S., SANDIFORD, N. & KABIR, C. (2008). Total hip resurfacing as an alternative to total hip arthroplasty: Indications and precautions. *Seminars in Arthroplasty*, **19**, 274 – 282.

MYRONENKO, A. & SONG, X. (2010). Point set registration: Coherent point drift. *IEEE Transactions on Pattern Analysis and Machine Intelligence*, **99**.

NABEYAMA, R., MATSUDA, S., MIURA, H., MAWATARIM, T., KAWANO, T. & IWAMOTO, Y. (2004). The accuracy of image-guided knee replacement based on computed tomography. *J. Bone Joint Surg.*, **86-B**, 366–371.

NOGLER, M., MAURER, H., WIMMER, C., GEGENHUBER, C., BACH, C. & KRISMER, M. (2001). Knee pain caused by a fiducial marker in the medial femoral condyle: a clinical and anatomic study of 20 cases. *Acta orthopaedica Scandinavica*, **72**, 477–80.

NOPPADOL, C. & KE, C. (2009). A robust affine image registration method. **6**, 311–334.

PAUL, H., BARGAR, W., MITTLESTAD, B., MUSITS, B., TAYLOR, R., KAZANZIDES, P., ZUHARS WILLLIAMSON, B. & W, H. (1992). Development of a surgical robot for cementless total hip arthroplasty. *Clin Orthop*, **285**, 57–66.

PEARLE, A.D., KENDOFF, D., STUEBER, V., MUSAHL, V. & REPICCI, J.A. (2009). Perioperative management of unicompartmental knee arthroplasty using the mako robotic arm system (makoplasty). *American Journal of Orthopedics*, **38**, 16–19.

PENNEY, G., BARRATT, D., CHAN, C., SLOMCZYKOWSKI, M., CARTER, T., EDWARDS, P. & HAWKES, D. (2006). Cadaver validation of intensity-based ultrasound to ct registration. *Medical Image Analysis*, **10**, 385 – 395.

PICCAND, S., NOUMEIR, R. & PAQUETTE, E. (2008). Region of interest and multiresolution for volume rendering. *Information Technology in Biomedicine, IEEE Transactions on*, **12**, 561 – 568.

PIRES, P.M.S. (2014). *Position and Force Control of Lightweight Robot Manipulators for Orthopedic Surgery*. Ph.D. thesis, Instituto Superior Técnico, Universidade de Lisboa.

RAAIJMAAKERS, M., GELAUDE, F., DE SMEDT, K., CLIJMANS, T., DILLE, J. & MULIER, M. (2010). A custom-made guide-wire positioning device for hip surface replacement arthroplasty: description and first results. *BMC Musculoskeletal Disorders*.

ROOKS, B. (2006). The harmonious robot. *Industrial Robot: An International Journal*, **33 (2)**, 125–130.

RUSU, R. & COUSINS, S. (2011). 3d is here: Point cloud library (pcl). In *Robotics and Automation (ICRA), 2011 IEEE International Conference on*, 1–4.

SALVI, J., MATABOSCH, C., FOFI, D. & FOREST, J. (2006). A review of recent range image registration methods with accuracy evaluation. *Image and Vision Computing*.

SANCHES, J., NASCIMENTO, J. & MARQUES, J. (2008). Medical image noise reduction using the sylvester-lyapunov equation. *IEEE transactions on image processing*, **17**, 1522–39.

SANDHU, R., GEORGIOU, T. & TANNENBAUM, A. (2008). A new distribution metric for image segmentation. In *SPIE Medical Imaging*, vol. 3, Citeseer.

SATAVA, R. (2002). Surgical robotics: the early chronicles: a personal historical perspective. *Surg Laparosc Endosc Percutan Tech*, **12**.

SCHULZ, A.P., FABER, A. & MEINERS, J. (2007). Determination of optimal non-invasive patient fixation methods for use in robotic hip replacement surgery - an in vitro study. 135–139.

SETHIAN, J. (1996). Level set methods and fast marching methods. *Cambridge University Press*.

SHIMMIN, A., BARE, J. & BACK, D. (2005). Complications associated with hip resurfacing arthroplasty. *Orthopedic clinics of North America*, **36**, 187–193.

SHIMMIN, A.J. & BACK, D. (2005). Femoral neck fractures following birmingham hip resurfacing: A national review of 50 cases. *Journal of Bone & Joint Surgery, British Volume*, **87-B**, 463–464.

SHIRAI, Y. & INOUE, H. (1973). Guiding a robot by visual feedback in assembly tasks. *Pattern Recognition*, **5**, 99–108.

SMITH&NEPHEW (2008). Smith and nephew birmingham hip resurfacing, surgical technique.

SOUSA, J. & KAYMAK, U. (2002). *Fuzzy Decision Making in Modeling and Control*. World Scientific Publishing Co., Singapore.

STIEHL, J., KONERMANN, W., HAAKER, R. & DIGIOIA, A. (2007). *Navigation and MIS in Orthopedic Surgery*. Springer.

SUGANO, N. (2003). Computer-assisted orthopedic surgery. *Computer-Aided Design*, 442–448.

SUH, I. & KIM, T. (1994). Fuzzy membership function based neural networks with applications to the visual servoing of robot manipulators. *IEEE Transactions on Fuzzy Systems*, **2**, 203–220.

SUH, I. & KIM, T.W. (2000). A visual servoing algorithm using fuzzy logics and fuzzy-neural networks. *Mechatronics*, **10**, 1–18.

TAKAGI, T. & SUGENO, M. (1985). Fuzzy identification of systems and its applications to modelling and control. *IEEE Transactions on Systems, Man, and Cybernetics*, **15**, 116–132.

TAPANINEN, T., KROGER, H., JURVELIN, J. & VENESMAA, P. (2012). Femoral neck bone mineral density after resurfacing hip arthroplasty. *Scandinavian Journal of Surgery*, **101**, 211–215.

TORRES, P., GONÇALVES, P. & MARTINS, J. (2011a). Robot calibration for precise ultrasound image acquisition. *Romanian Review Precision Mechanics, Optics & Mechatronics*, 129–134.

TORRES, P.M.B., GONÇALVES, P.J.S. & MARTINS, J.M.M. (2011b). Bone registration using a robotic ultrasound probe. In *VipIMAGE 2011 - III ECCOMAS Thematic Conference on Computational Vision and Medical Image Processing*.

TYRYSHKIN, K., MOUSAVI, P., BEEK, M., ELLIS, R., PICHORA, D. & ABOLMAESUMI, P. (2007). A navigation system for shoulder arthroscopic surgery. *Proceedings of the Institut of Mechanical Engineers. Part H, Journal of engineering in medicine*, **6 (1)**, 221–19.

V. CASELLES, R.K. & SAPIRO, G. (1997). Geodesic active contours. *International Journal on-ComputerVision*, **22**, 61–97.

WALLIS, J., MILLER, T., LERNER, C. & KLEERUP, E. (1989). Three-dimensional display in nuclear medicine. *Medical Imaging, IEEE Transactions on*, **8**, 297 –230.

WEI SONG, W., HUA LI, G., YING OU, Z., HAN, J., ZHAO, D.W. & MING WANG, W. (2007). Model-based segmentation of femoral head and acetabulum from ct images. In *Complex Medical Engineering, 2007. CME 2007. IEEE/ICME International Conference on*, 586 –590.

WINTER, S., BRENDEL, B. & IGEL, C. (2006). Registration of bone structures in 3d ultrasound and ct data: Comparison of different optimization strategies.

ZHANG, K., ZHANG, L., SONG, H. & ZHOU, W. (2010). Active contours with selective local or global segmentation: A new formulation and level set method. *Image and Vision Computing*, **28**, 668–676.